THE UNIVERSITY OF SYDNEY

High Resolution Imaging and the Formation of Stars and Planets

Anthony Craig Cheetham

A thesis submitted in fulfilment
of the requirements for the degree of
Doctor of Philosophy

Faculty of Science
University of Sydney
2015

Statement of Originality

I, Anthony Cheetham, hereby declare that all work presented in this thesis is based on research conducted by me during my PhD candidature at the Sydney Institute for Astronomy, University of Sydney, from February 2012 to April 2015. I declare that none of this work has been submitted to obtain another degree at this or any other university. Most work presented in this thesis is based on collaborative efforts and I have clearly stated in each case which part of the work was done by me and which by others. To the best of my knowledge, this thesis contains no copy or paraphrase of work by others, except where clearly acknowledged in the text.

Anthony Cheetham

Date

Abstract

Understanding the formation of stellar and planetary systems is one of the great challenges of contemporary astrophysics. Stellar evolutionary models are supported by a large volume of observational evidence with which to calibrate models for stars once they reach the main sequence, but models for young stars are not as well constrained. Models for substellar objects such as brown dwarfs and exoplanets are similarly uncertain due to the difficulty of obtaining incisive measurements. Predictions for the location and timing of planet formation differ and are also currently not well constrained. In addition, most detailed numerical modelling of star and planet formation has concentrated on single stars, while it is known that a large fraction of stars form in multiple systems. These problems demonstrate that further observations are needed to test and refine these models, so that we can fully understand the processes behind the formation of stellar systems. This thesis describes progress towards these goals, through advancement of techniques to enable high resolution imaging of faint companions and other structures in the immediate environs of young stars.

Future high resolution imaging studies will rely on large segmented telescopes such as the James Webb Space Telescope, Giant Magellan Telescope, European Extremely Large Telescope and the Thirty Meter telescope. In order to ensure optimal performance, techniques to precisely cophase the mirror segments are required. In this thesis we propose the Fizeau Interferometric Cophasing of Segmented Mirrors algorithm, and present the results of testing both numerically and through experiment. First, we simulate the performance of the technique under realistic noise conditions and present additional strategies to ensure its robustness. We then perform experiments to verify the concepts behind the algorithm and measure its accuracy in a real optical-testbed setting.

We use high resolution techniques to rectify a lack of observational evidence with which to test brown dwarf evolutionary models, by laying the foundation for an orbital monitoring survey of 19 brown dwarf binary systems. The results of this survey should greatly expand the number of known model-independent masses for these objects. We also report the discovery of an additional 7 low mass companions to intermediate mass stars. These objects straddle the stellar/sub-stellar boundary and should allow precise mass, luminosity and age information to be obtained following characterisation of their orbits.

We perform a Non-Redundant Masking (NRM) survey targeting the 1 Myr old Ophiuchus star forming region. Both binary statistics and the relationship between multiplicity and the presence of a circumstellar disk are explored, providing many results similar to those from older regions. This helps frame the time evolution of effects related to dynamical interactions in binary systems, and the timescale of disk dissipation, with profound implications for giant planet formation.

In thesis we also present the results of commissioning for the Gemini Planet Imager Non-Redundant Masking mode. These results indicate that the addition of an Extreme Adaptive Optics systems has substantially improved the performance of NRM compared to previous instruments. Using the instrument, we then study the circumbinary transition disk HD 142527, with a highly significant detection of the low mass stellar companion that should help with future studies of this system aiming to provide an orbit for the companion. In addition, resolved polarized structure is tentatively detected. Finally, GPI NRM is used to study the mass losing supergiant VY CMa, providing a high resolution image reconstruction that verifies the imaging ability of GPI NRM and allows measurement of the wind speed, in agreement with previous measurements.

Finally, the transition disk T Cha is studied with multi-epoch NRM data, showing that the signal previously interpreted as a planetary companion is more likely to be the result of forward scattering from the inclined outer disk. Transition disks such as T Cha and HD 142527 represent an important stage in the evolution of circumstellar disks and reveal much about the processes and timing of planet formation and its relation to the stellar environment.

Publications

The following papers have been published in or submitted to refereed journals and are results from the work presented in this thesis and other related research collaboration.

- **Cheetham, A.C.**, Tuthill, P.G., Sivaramakrishnan, A., Lloyd, J.P.. *Fizeau interferometric cophasing of segmented mirrors*. Optics Express (2012), 20 (28), 29457–29471.
- **Cheetham, A.C.**, Cvetojevic, N., Norris, B., Sivaramakrishnan, A., Tuthill, P.G.. *Fizeau interferometric cophasing of segmented mirrors: experimental validation*, Optics Express (2014), 22 (11), 12924–12934.
- **Cheetham, A.C.**, Huélamo, N., Lacour, S., de Gregorio-Monsalvo, I., Tuthill, P.. *Near-IR imaging of T Cha: evidence for scattered-light disc structures at Solar system scales*. MNRAS (2015), 450, L1-L5.
- **Cheetham, A.C.**, Kraus, A.L., Ireland, M.J., Cieza, L., Rizzuto, A.C., Tuthill,P.G. *Mapping the shores of the brown dwarf desert. IV. Ophiuchus*. Submitted to ApJ (2015).
- Hinkley, S., Kraus, A.L., Ireland, M.J., **Cheetham, A.C.**, Carpenter, J.M., Tuthill, P.G., Lacour, S., Evans, T.. *Discovery of Seven Companions to Intermediate Mass Stars with Extreme Mass Ratios in the Scorpius-Centaurus Association*. ApJL (2015), 806, L9.
- Pope, B., Cvetojevic, N., **Cheetham, A.C.**, Martinache, F., Norris, B., Tuthill, P.G.. *A Demonstration of Wavefront Sensing and Mirror Phasing from the Image Domain*. MNRAS (2014), 440, 125–133.

In addition, the following are publications in conference proceedings relating to the work presented in this thesis and other related research collaboration.

- **Cheetham, A.C.**, Cvetojevic, N., Sivaramakrishnan, A., Tuthill, P.G.. *Fizeau Interferometric Cophasing of Segmented Mirrors*. Proceedings of SPIE Astronomical Telescopes and Instrumentation (2014), 9143, 52C.
- Sivaramakrishnan, A., Lafrenière, D., Saavik Ford, K.E., McKernan, B., **Cheetham, A.C.**, Greenbaum, A.Z., Tuthill, P.G., Lloyd, J.P., Ireland, M.J., Doyon, R., Beaulieu, M., Martel, A., Koekemoer, A., Martinache, F., Teuben, P.. *Non-Redundant Aperture Masking Interferometry (AMI) and Segment Phasing with JWST-NIRISS*. Proceedings of SPIE Astronomical Telescopes and Instrumentation (2012), 8442, 2SS.

- Greenbaum, A.Z., **Cheetham, A.C.**, Sivaramakrishnan, A., Tuthill, P., Norris, B., Pueyo, L., Sadakuni, N., Rantakyrö, F., Hibon, P., Goodsell, S., Hartung, M., Serio, A., Cardwell, A., Poyneer, L., Macintosh, B., Savransky, D., Perrin, M.D., Wolff, S., Ingraham, P., Thomas, S.. *Gemini planet imager observational calibrations X: non-redundant masking on GPI*. Proceedings of SPIE Astronomical Telescopes and Instrumentation (2014), 9147, 7BG.
- Sivaramakrishnan, A., **Cheetham, A.C.**, Greenbaum, A.Z., Tuthill, P.G., Acton, D.S., Pope, B., Martinache, F., Thatte, D., Nelan, E.P. *Non Redundant Masking Ideas on JWST*. Proceedings of SPIE Astronomical Telescopes and Instrumentation (2014), 9143, 3SS.

Acknowledgements

I would like to thank my supervisors Peter Tuthill and Anand Sivaramakrishnan for all of their advice, hard work and encouragement during the past 3 years. I was extremely fortunate to have such excellent PhD supervisors, who gave me the right mix of freedom and guidance. Peter, thank you for always finding time to answer questions and discuss ideas with me, for teaching me so much about interferometry and the world of science, as well as all your help with drafts of observing proposals, papers and thesis chapters. Anand, thanks for all of your help, for answering all of my questions and for being such a gracious host during my visit. I also want to thank Mike Ireland, Adam Kraus, Nuria Huélamo and all of my other collaborators for all of their assistance and advice over the years.

I want to extend my gratitude to the entire interferometry / high angular resolution astronomy group at Sydney for all of their help along the way, and making it such a fun (and awesomely quirky) environment to do research, as well as the whole SIfA community. Special thanks go to Paul Stewart for never missing an opportunity for a joke, and Barnaby Norris for all of the discussions we had after I encountered difficult problems. Many thanks to Alex Greenbaum for all of her help with GPI and JWST related questions, and for being a fantastic person to work with.

To all of the people I've been lucky enough to call friends, thanks for being there for me and keeping me sane. To James, Eleanor, Andy, Brad, John, Jedd, Jesh, Jude, Mel and the rest, thanks for being such an awesome group of friends for all these years. Special thanks go to Brad for always keeping things interesting and generally being a fantastic flatmate, and to Jesh for being a constant source of energy and enthusiasm. To Matt, David, Alison, Paul, Jason, Dan and the others, thanks for some memorable games of maths snap, velodrome and DKR.

Last but certainly not least, I wish to thank my family, to whom I owe everything. To my parents: for always encouraging me to follow my dreams, for being great role models, and for all of their hard work and support throughout the years. And to my brother Grant: thanks for always being up for a chat, for being there to listen to me through the hard times, and for being a great friend.

Contents

Chapter 1

Introduction

1.1 Star and Planet Formation

1.1.1 Formation Processes

The standard model for star formation begins with dense molecular clouds. Turbulence within these clouds results in local overdensities which, upon reaching a sufficient density and mass, begin to collapse (Jeans, 1902). As an overdense region collapses, it begins to flatten into a disk due to conservation of angular momentum. At the centre of the disk, the temperature increases until it reaches hydrostatic equilibrium, forming a dense protostar at its core.

Forming protostars are usually divided into four, observationally-motivated, evolutionary stages (e.g. Andre et al., 1993). In the Class 0 phase, protostars are highly embedded and rapidly accrete mass from their surroundings. Class I sources also exhibit strong accretion, but possess clear circumstellar disks and envelopes. As accretion slows and the envelope dissipates, the protostars enter the Class II phase. Class III marks the end of any significant stellar accretion and the removal of gas from the circumstellar disk.

At the same time as the progression of the protostar through the evolutionary stages, planet formation occurs in the circumstellar disk. There are two competing models to explain the process of planet formation in these conditions; core accretion (Pollack et al., 1996) and disk instability (Rasio and Ford, 1996; Boss, 2001).

The disk instability scenario posits that the disk is gravitationally unstable. Planets are then thought to form directly due to the gravitational collapse of a region (Youdin and Shu, 2002), a process analogous to that of stellar formation.

In the core accretion scenario, planet formation is initiated by dust grains in the cooling gaseous disk. Due to the density profile of the disk decreasing at larger radii, the gas pressure acts to partially balance the gravitational force and leads to the gaseous component moving slightly slower than the Keplerian rotation velocity (Lissauer, 1993). Larger dust particles are decoupled from the gas and instead move at the Keplerian speed, causing them to feel an increased drag force and settle out of the gas disk towards the midplane. Collisions between dust grains cause them to stick together and grow in size (Dominik and Tielens, 1997).

It is not currently understood how kilometre-sized objects form, since models predict that inward migration (Weidenschilling, 1977) and destructive collisions should prevent further growth before this scale, leading to a “metre size barrier”. Many methods to circumvent this have been

proposed, and this remains a developing area of research. However, once kilometre-sized objects are formed, planetesimal mergers generating growth become more likely than destructive collisions; an effect that increases with the size of the planetesimals (Chambers, 2001). This leads to runaway growth and to the formation of protoplanets. Large protoplanetary cores then sweep up gaseous material that lies within their Hill radius, the radius at which the protoplanet's gravitational influence dominates over that of the star.

The pathway by which gas-rich protoplanetary disks become rocky debris disks is currently unclear. Observations have revealed a class of object known as "transition disks" that are thought to represent the short-lived intermediate stage between these two. A lack of near-infrared excess indicates that these objects possess partially evacuated cavities with radii of several AU (Calvet et al., 2002). Spatially resolved observations support this assertion, revealing dense outer disks with sharp inner edges (Thalmann et al., 2010; Quanz et al., 2013). In addition, a further subclass termed "pre-transition disks" have been observed, which possess optically thick inner disks in addition to outer disks.

Several plausible theories for the cause of transition disk gaps have been suggested and observations of these objects are needed to resolve their origin. The most commonly cited ideas include grain growth and radial transport (Dullemond and Dominik, 2005), dissipation due to photoevaporation (Alexander and Armitage, 2007), and disk truncation due to dynamical interaction with a close stellar or sub-stellar companion (e.g. Ireland and Kraus, 2008). As noted above, giant planets forming within a protoplanetary disk are expected to sweep gaseous material from their surroundings, leaving a partially evacuated annulus in the disk. This provides another exciting hypothesis; that the presence of these disk gaps indicates the location of forming giant planets. These objects then represent ideal opportunities to study disk evolution and planet formation in situ.

Despite significant progress towards understanding the processes of planet and star formation, many unanswered questions remain. The aforementioned metre size barrier presents significant challenges to modelling efforts. Observations have not settled the debate between the two competing models for star formation. The location and timing of planet formation remain uncertain, and theories about the role of planetary migration in the observed distributions of planets in older systems have limited observational constraints.

1.1.2 Exoplanetary Systems

The first exoplanet orbiting a main sequence star outside our Solar System was discovered only 20 years ago, around the star 51 Pegasi (Mayor and Queloz, 1995). Since then, a plethora of discoveries have been made, resulting in more than 1900 known planets spread over more than 1000 known planetary systems. In addition, a further 3300 planetary candidates have been announced.

The majority of these systems have been detected through indirect means. The most common of these techniques involve changes in the brightness of a star due to a faint planet passing in front (the transit method), or the measurement of the tiny periodic Doppler shift signal of a host star as it orbits around the barycentre of the planet-star system (the radial velocity method).

Recent advances in instrumentation have lead to spectrographs and photometric instruments, such as the Kepler mission, able to target exoplanets with masses similar to those of the terrestrial planets in our own Solar System (Borucki et al., 2010). While the majority of systems to date have been substantially more massive than the Earth and with orbital separations far less than

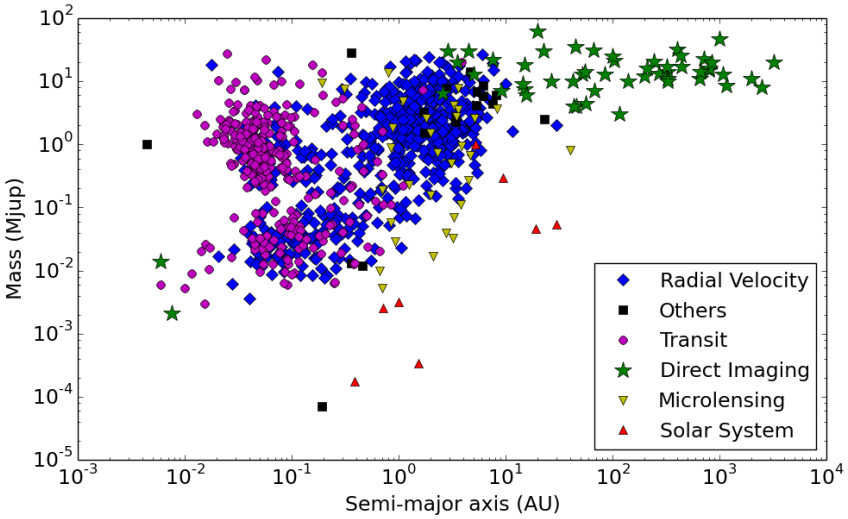

Figure 1.1: The masses and orbital semi-major axes of all confirmed exoplanets as of March 2015. When split by their detection method, observational biases for each method are evident. The "Others" category includes planets detected by astrometry and pulsar timing. The two low mass, small semi-major axis planets marked as direct imaging were detected based on polarization changes due to reflected light. The Solar system planets are plotted for reference. Data are taken from exoplanet.eu (Han et al., 2014).

that of Jupiter, these techniques are pushing the boundaries towards lower mass planets at larger separations.

However, due to limitations and biases inherent to these techniques, direct observations of exoplanets are highly sought after. Both the transit and radial velocity techniques are biased towards high mass planets at small separations around old stars. These techniques both require time-series data spanning multiple orbits to confirm that a companion candidate is planetary, and the time baseline required for a widely separated planetary orbit makes such systems impractical to observe. The characteristic variability of young stars also provides a challenge for these methods, since stellar activity leads to noise in both photometric and spectroscopic observations, masking the signal caused by any potential planets.

A natural way to complement these methods is through direct imaging, which is instead biased towards high mass planets at large separations around young stars. These biases are clearly seen in Figure 1.1 which shows all currently known exoplanets plotted as a function of mass and separation, marked by their detection method. The distribution of exoplanet ages is shown in Figure 1.2, which illustrates the bias of indirect methods towards older planets, while direct imaging covers a wider range of ages. The combination of these techniques allows a range of planetary separations and ages to be explored.

In particular, exploring the incidence and properties of planets around young stars is important for testing current planet formation models. It is expected that dynamical interactions between

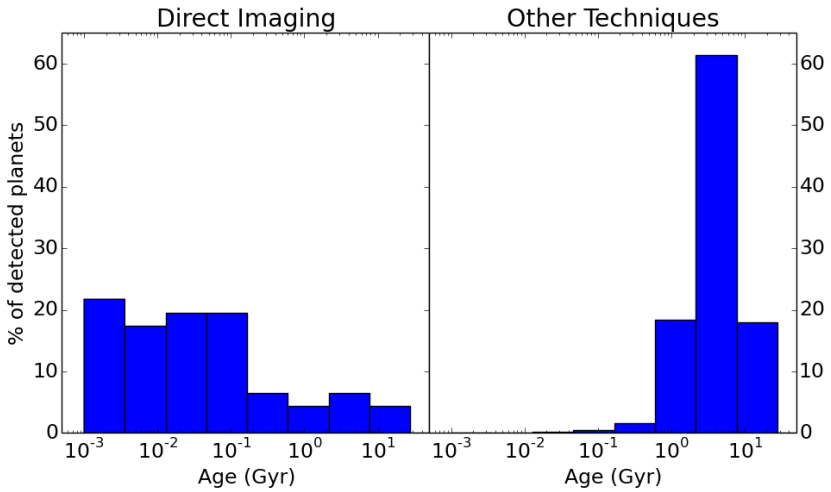

Figure 1.2: The host star ages of all confirmed exoplanets as of March 2015. The radial velocity and transit techniques that have resulted in the vast majority of exoplanet detections to date are biased towards older stars, while direct imaging is instead biased towards younger stars. Data are taken from exoplanet.eu (Han et al., 2014).

planets plays a significant role in determining their final configurations, and leads to the observed distributions of planet masses and separations being different from the primordial distributions. Observations of young systems are needed to resolve this discrepancy and test predictions about the location and timing of planet formation.

Models describing exoplanet atmospheres also have very little observational evidence to calibrate against. To provide this information, exoplanet spectra are needed that allow precise measurement of their atmospheric compositions. Indirect techniques that fail to separate the light of an exoplanet from that of its host star necessarily encounter problems trying to disentangle the stellar and planetary contributions, while direct imaging offers an alternative pathway that eliminates many of these problems.

Development of high angular resolution direct imaging techniques for the detection of faint companions is important to test a range of theoretical models relating to star and planet formation, as well as providing complementary information on the incidence and properties of exoplanets.

1.2 High Angular Resolution Imaging

1.2.1 Adaptive Optics and Coronagraphy

The fundamental challenge of directly imaging exoplanets (and other faint structure) involves distinguishing the faint glow of the exoplanet from that of the star that it orbits, which is usually many orders of magnitude brighter. Both the small angular separations and extreme differences in brightness make direct imaging difficult. The most common technique to tackle these chal-

lenges combines coronagaphy with Adaptive Optics (AO) and significant post-processing to remove noise.

A revolution in high angular resolution astronomy was precipitated by the introduction of fast computers that made it possible for corrections to be made to incoming wavefronts to cancel the effects of the atmosphere. AO typically relies on combining a wavefront sensor with a controllable deformable mirror. By placing the deformable mirror in a pupil plane of the telescope, the phase effects of the turbulent atmosphere can be counteracted by the addition of phase delays on the deformable mirror calculated to reverse the errors.

The most common type of wavefront sensor is the Shack-Hartmann sensor (Hartmann, 1900; Shack and Platt, 1971), which places an array of lenslets in a pupil plane to break the incoming wavefronts into small pieces which are focussed into spots on a detector. Small tilts in the incoming wavefront then manifest as shifts in the position of each of the spots. By measuring the centroid for each lenslet, the overall shape of the wavefront can be constructed.

A more recent alternative wavefront sensor design was proposed by Ragazzoni (1996), based around forming an image plane at the vertex of a glass pyramid, which then splits the incoming light into four parts. From there, a lens produces four images of the pupil onto a detector. The relative brightness between the same pupil location in the four images is analagous to a quad-cell (2x2) Shack-Hartmann sensor and gives a measure of the wavefront slope. This design has the advantage of allowing the wavefront sampling and the gain to be tuned in a simple and continuous manner.

After the shape of the incoming wavefront has been measured, the delays needed to flatten it are calculated and applied to the deformable mirror. By measuring the wavefront changes many times faster than the atmospheric coherence time, the resulting wavefront can be kept relatively stable, leading to a stable instrument point-spread function (PSF).

Adaptive optics has allowed detailed study of faint structure at high angular resolution. The stable PSF provided by an AO system is crucial for coronography, which in its simplest form directs starlight onto an opaque occulting spot in order to suppress its contribution to the total flux and reveal faint structure in its surroundings. This approach (called Lyot coronagraphy) has been moderately successful in the past, contributing to the detection of the majority of directly imaged exoplanets (Kalas et al., 2008; Marois et al., 2008).

Currently, the most commonly used coronagraph designs pair an occulting spot with an apodizer placed in the pupil plane to reduce the amplitude variations of the PSF wings. This technique is known as Apodized Pupil Lyot Coronagraphy (APLC). Several new approaches have been proposed in an attempt to solve some of the drawbacks of APLC designs, and have recently been implemented on large telescopes. The Four-Quadrant Phase Mask (Rouan et al., 2000) is a transmissive mask in the image plane consisting of four quadrants that introduce either a 0 or π phase shift. By placing the stellar PSF at the center of the mask, the beams passing through each quadrant interfere destructively with their neighbours, providing excellent rejection of starlight. The Vortex Coronagraph (Foo et al., 2005; Mawet et al., 2005) extends this idea by creating an optical vortex, where the phase introduced to the image plane forms a helical shape. This results in an intensity null at the centre, with little effect on off-axis sources.

Coronography is an integral part of current and future exoplanet research, with instruments such as the Gemini Planet Imager (GPI Macintosh et al., 2008a), the Spectro-Polarimetric High

contrast Exoplanet REsearch instrument (SPHERE Beuzit et al., 2008), and the Subaru Coronagraphic Extreme AO instrument (SCExAO Martinache and Guyon, 2009) all utilising coronagraphic designs.

Angular Differential Imaging (ADI Schneider and Silverstone, 2003; Marois et al., 2006) techniques are commonly used to improve the resulting obtainable contrast, often in conjunction with coronagraphy. The most common of these techniques involves setting up the telescope so that the pupil is stabilised. In this mode the field, and therefore the exoplanet signal, rotate with the motion of the sky. In this way the PSF is stable and a best-guess as determined by advanced procedures such as LOCI (Lafrenière et al., 2007b), TLOCI(Marois et al., 2014), or KLIP (Soummer et al., 2012) can be subtracted from each frame, the stellar and instrumental contribution to each image can be minimized. The resulting frames are then rotated to counteract sky rotation and added together, allowing faint structure and exoplanets to be detected at high significance. By combining images taken at different wavelengths through a process known as Spectral Differential Imaging (Marois et al., 2000), the instrumental and stellar contribution can be further suppressed. This relies on the fact that the PSF size scales with wavelength, while source structure remains at a fixed position. The combination of these techniques is critical to the success of current and future coronagraphic instruments for the direct imaging of exoplanets.

1.2.2 Aperture Masking

While coronagraphy allows the achievement of very high contrasts, exoplanet searches are restricted to angular separations larger than the occulting spot. Many of the recent advances in coronagraph technologies have been motivated by reducing the size of the coronagraph spot to decrease their inner working angle.

One technique for studying structure at angular separations smaller than can be studied through coronagraphy or conventional imaging is that of aperture masking interferometry, also called Non-Redundant Masking (NRM) or sparse aperture masking. This technique was based on early interferometric work by Fizeau (1868) and Michelson (1920), and was first applied by Baldwin et al. (1986). Since then, NRM has been established as a workhorse technique for obtaining measurements of high contrast structure at small angular separations. Its principal advantages include high angular resolution, high dynamic range of measurements and resistance to wavefront errors located in the pupil plane of the telescope (such as those caused by atmospheric seeing).

The advantages of aperture masking are achieved by turning a telescope pupil into a sparse interferometric array. Large regions of the telescope pupil are blocked, with the unblocked regions carefully located such that the baseline vector (that joins any two mask holes) is unique. The advantages of such a technique are not immediately obvious but counter-intuitively, lie in the way that it preserves rather than averages wavefront errors across the telescope pupil.

The dominant source of wavefront error for ground based telescopes is the rapidly varying and random changes in the refractive index of the air column above them that modify the wavefront as it propagates through the atmosphere. This has the effect of adding an unknown phase distribution to the wavefront, with a smaller change to the wavefront amplitude distribution.

In addition to the contribution from the atmosphere, wavefront pertubations are inevitably introduced by the imaging system itself, as small deformations in mirror surfaces and small changes

to mirror shapes are unavoidable. Wavefront errors generally act to change the PSF shape, making identification and calibration of detected structure difficult.

In the case of a non-redundant pupil, a unique set of interference fringes is generated from each pair of points in the pupil, and the PSF is the superposition of these interference fringes. Consider a single pair of points in the pupil and the baseline vector that connects them, which defines the spatial frequency and orientation of the fringes produced by those points. The phase changes introduced by wavefront errors will affect the phase of the corresponding interference fringes, while the amplitude changes (such as scintillation) will affect the fringe amplitude. The measured phase for the corresponding interference fringes (ϕ_{12}) is then a simple sum of the phase due to the source (Φ_{12}) and the difference between the pupil plane phases at the position of the two points ($\epsilon_1 - \epsilon_2$).

From the measured phases a quantity called "closure phase" can be constructed, which has the remarkable property of being robust to wavefront errors in the case of a non-redundant array geometry. Closure phases are calculated from the sum of the fringe phases measured on any 3 baselines arising from the same 3 subapertures in the telescope pupil. For subapertures 1, 2 and 3, the closure phase Φ_{cp} can be calculated from the measured phases from the 3 baselines ($\phi_{12}, \phi_{23}, \phi_{31}$). As before, the phases measured on each baseline have two terms: the difference in the wavefront error from the two subapertures ($\epsilon_1 - \epsilon_2$) and the phase inherent to the source itself Φ_{12}.

$$\Phi_{cp} = \phi_{12} + \phi_{23} - \phi_{31} \tag{1.1}$$
$$= \Phi_{12} + \Phi_{23} - \Phi_{31} + (\epsilon_1 - \epsilon_2) + (\epsilon_2 - \epsilon_3) + (\epsilon_3 - \epsilon_1) \tag{1.2}$$
$$= \Phi_{12} + \Phi_{23} - \Phi_{31} \tag{1.3}$$

When constructing closure phases, the phase contributions due to wavefront error cancel, leaving only the phase inherent to the source. This allows NRM to obtain sensitive measurements of structure at small angular separations, where wavefront errors typically prevent other techniques from obtaining high contrasts.

For a redundant pupil, multiple sets of points have the same baseline vector and each produce a set of fringes with the same orientation and spatial frequency. However the amplitude and phase of each of these fringes will be different, and the final calculated amplitude and phase for that spatial frequency will come from their vector sum. This prevents the wavefront error terms in the closure phase from cancelling, leading any attempted closure phase measurement to be much noisier than the non-redundant case.

The other most commonly used measurable in aperture masking is the fringe visibility amplitude $|V|$, often used in the form of the square visibility V^2. The visibility amplitude is related to the fringe amplitude, and is often combined with the fringe phase to give the complex visibility V. Mathematically, it has the following definition:

$$|V| = \frac{I_{max} - I_{min}}{I_{max} + I_{min}} \tag{1.4}$$

where I_{max} and I_{min} are the minimum and maximum intensity of the relevant interference fringes.

The square visibility is also robust to atmospheric phase errors in non-redundant setups. However, in redundant setups the V^2 is given by the vector sum of the complex visibilities for each of the points with the same baseline vector, leading to noisier measurements.

An additional advantage of aperture masking is its adherence to the interferometric diffraction limit of $\frac{1}{2}\frac{\lambda}{D}$, rather than the traditional Rayleigh diffraction limit of $1.22\frac{\lambda}{D}$. This allows measurements to be conducted on smaller angular scales than conventional imaging techniques.

Aperture masking has established itself as a technique for obtaining high contrast measurements at small angular scales, but suffers from several disadvantages compared to other direct imaging methods. The closure phases produced by any single model are a function of 4 independent variables (2 sets of baseline lengths and directions), and are inherently difficult to visualise. For this reason, aperture masking relies on model fitting and it is important to ensure a robust estimate of the significance of a detected signal. Determining a valid model to fit to the data is difficult, and this can lead to incorrect interpretation of detected structure (e.g. Olofsson et al., 2013, and Chapter 7).

Closure phases and square visibilities suffer from systematic terms, of which the main contributors are wavefront errors on scales smaller than a mask hole, temporal changes in the wavefront during an exposure and the small amount of redundancy caused by non-zero size of the mask holes and the polychromaticity of the incoming light. To calibrate aperture masking data, these quantities are measured on known point source calibrator stars. The accuracy of this calibration is the limiting factor for aperture masking measurements.

The contrasts obtained by NRM are not competitive with those obtained by coronagraphic techniques at larger separations. In addition, the outer working angle resulting from NRM limits the technique to a narrow field of view. Despite this, NRM has found widespread use for studying the very youngest stars by targeting nearby star forming regions, where the combination of angular resolution and obtainable contrast offers it a unique window into recently formed planetary systems.

1.2.3 Mirror Cophasing

Optical astronomy is rapidly moving towards a future dominated by large telescopes employing a segmented design. The European Extremely Large Telescope (E-ELT), Giant Magellan Telescope (GMT), Thirty Meter Telescope (TMT) and James Webb Space Telescope (JWST) all have segmented primary mirrors, and will be the largest of their kind on land and in space. In addition, many current facilities such as the Keck telescopes have similar segmented designs. These telescopes are expected to contribute significantly towards high angular resolution studies of star and planet formation and optimising their performance at such tasks is an important step in preparing for their use.

Primary mirror segmentation was designed to eliminate problems with monolithic (single element) designs, which grew increasingly heavy and difficult to manufacture as aperture sizes increased. To ensure optimal performance, telescope mirrors must conform to a rigid predefined shape, even when tilted to observe stars across the sky. As their sizes increased, fundamental limits on the strength of the materials used made this impossible. One way to avoid this problem is through active control of the mirror shape to account for these known effects, a method known

as “active optics”. Another option involves increasing the strength-to-weight ratio of the materials used, such as through the use of a honeycomb design. But these techniques merely delay the problem rather than solving it, and themselves become impractical for larger mirrors. Segmented mirrors instead solve the problem by breaking the mirror into many smaller pieces that can be made rigid more easily. However, in order for the mirror to match its predefined shape, the separate segments must be aligned through a process known as “cophasing”.

The foundation of any cophasing strategy is the ability to measure the piston and tip/tilt between segments. Piston is defined as the height difference between segments along the direction out of the plane of the mirror, while the tip and tilt of any segment are its slopes in two orthogonal directions. In addition to these aberrations, the rotation of a segment in the plane of the mirror (segment clocking) can be important to measure and correct, especially when segments are not symmetrical (such as those of JWST). For curved segments, higher order wavefront errors such as focus must also be accounted for, but are not measured by most cophasing algorithms currently in use.

Many of the first cophasing techniques were successfully demonstrated at the Keck telescopes, the first large optical segmented telescopes. The most commonly used algorithm employs a modified Shack-Hartmann sensor to measure wavefront discontinuities due to steps between adjacent segments (Chanan et al., 1998, 2000). This requires a separate phasing camera to monitor the diffraction patterns produced from the segment edges.

Dispersed Hartmann Sensing, the primary phasing method for JWST, is based on the modified Shack-Hartmann approach, but with the addition of a dispersive element to measure phase across a range of wavelengths and remove problems with phase wrapping (Wirth, 2003).

Another commonly used method is that of “curvature sensing” (Chanan et al., 1999). This technique involves taking images from a camera position either side of focus, using the differences between the images to estimate the wavefront error. The simplest implementation measures only the direction of the wavefront error rather than its magnitude and uses an iterative approach to cophase a mirror. Due to the requirement to change the relative position between the telescope focus and the camera, this method usually requires dedicated hardware and can introduce non-common path errors.

The use of dedicated phasing cameras introduces substantial non-common paths. Imperfect correction of resulting non-common path errors leads to a primary mirror shape that is not optimised with respect to a camera that is used to produce images for science. Existing techniques also have limited dynamic range, with large capture range measurements having limited accuracy and highly accurate measurements being limited in their range of operation. The current situation is not ideal, and there is room for new cophasing algorithms to solve these problems.

1.3 Outline of Thesis

This thesis covers recent advances in sparse aperture interferometric and other high resolution techniques for astronomy, most notably Non-Redundant Masking (NRM). These techniques are applied to a range of problems relating to the formation of stars and planets. The underlying technological goal of this work centred around the detection of faint companions to stars at small angular separations.

- In Chapter 2, I focus on a novel application of interferometric techniques to the problem of mirror cophasing, possible due to their ability to precisely measure phase. Methods such as this are necessary for future high resolution imaging searches using large segmented telescopes.
- Chapter 3 details two experiments that aim to demonstrate the algorithm introduced in Chapter 2 and show its viability for future implementation on ground and space based large segmented telescopes.
- In Chapter 4, I study brown dwarfs in multiple systems using high resolution imaging techniques. Orbital follow up of the targets studied in this chapter will produce precise age-mass-luminosity measurements necessary for brown dwarf evolutionary models.
- In Chapter 5, I perform a multiplicity survey of a nearby star forming region using NRM, providing a crucial test of many aspects of star and planet formation, including circumstellar disk evolution.
- In Chapter 6, I detail results from one of the next generation of instruments employing high resolution imaging techniques, focussing on the commissioning of NRM on the Gemini Planet Imager instrument. Details of the instrument are provided, as well as commissioning performance and two scientific applications explored with early data.
- In Chapter 7, I perform a high resolution study of the transition disk object T Cha, a young star thought to be in the process of forming planets. The nature of a previously suggested planetary companion candidate is investigated through analysis of several years of NRM data and detailed modelling of the disk.
- In Chapter 8, I summarise the results of this thesis and discuss the future for similar studies of star and planet formation.

Chapter 2

Fizeau Interferometric Cophasing of Segmented Mirrors

2.1 Mirror Cophasing with Interferometry

Due to its ability to precisely measure phase, non-redundant sparse aperture interferometry is a natural technique for wavefront sensing. In the following paper, I introduce a novel algorithm that applies interferometric techniques to the problem of segmented mirror cophasing. The algorithm was developed by myself, with some input and feedback from Peter Tuthill and Anand Sivaramakrishnan. The simulations and code were performed and developed by myself. This work was partially completed during my Honours year, when the basics of the technique were devised. During my PhD, the method was been modified extensively to make it more robust against noise and real-world conditions including nonzero filter bandwidths. Simulations were also performed, showing the capability of the algorithm when applied to the problem of cophasing for the James Webb Space Telescope, for which the technique is now an official backup. The manuscript was significantly improved based on feedback from the coauthors.

The following manuscript was published in Optics Express (2012) vol. 20, issue 28, p. 29457. The version presented here has been modified slightly from the published version.

Fizeau interferometric cophasing of segmented mirrors

Anthony C. Cheetham,[1] Peter G. Tuthill,[1] Anand Sivaramakrishnan,[2] and James P. Lloyd[3]

[1]Sydney Institute for Astronomy, School of Physics, University of Sydney, NSW 2006, Australia
[2]Space Telescope Science Institute, 3700 San Martin Drive, Baltimore MD 21218, USA
[3]Department of Astronomy, Cornell University, 122 Sciences Drive, Ithaca, NY 14853, USA

Abstract

Segmented mirror telescope designs address issues of mechanical rigidity, but introduce the problem of aligning, or cophasing, the separate segments to conform to the optimum mirror shape. While several solutions have been widely adopted, a few difficulties persist — the introduction of non-common path errors and an artificial division of the problem into coarse and fine regimes involving separate dedicated hardware solutions. Here we propose a novel method that addresses many of these issues. Fizeau Interferometric Cophasing of Segmented Mirrors (FICSM) uses non-redundant sparse aperture interferometry to phase mirror segments to interferometric precision using unexceptional science hardware. To show the potential of this technique we numerically simulate conditions on NASA's James Webb Space Telescope (JWST), showing that the FICSM method has the potential to phase the primary mirror from an initial state with segment-to-segment pistons as large as 150 microns and tilts as large as 0.5 arcseconds, to produce a final state with 0.75 nm rms segment-to-segment pistons and 3.7 mas rms segment tilts. The image undergoes monotonic improvement during this process. This results in a rms wavefront error of 3.65 nm, well below the 100 nm requirement of JWST's coarse phasing algorithm.

2.1.1 Introduction

The drive to telescopes with ever larger apertures has led to an explosion of interest in segmented mirror designs which can significantly reduce problems with mechanical rigidity. However, mirror segmentation introduces a new problem: that of aligning the separate segments to closely match the optimum mirror shape. This cophasing process is critical for the delivery of successful observational science. Many of the world's largest telescopes and all of the next generation of Extremely Large Telescopes plan to employ a segmented design, making the development and improvement of cophasing methods vital.

We posit that each segment has 6 rigid-body degrees of freedom (3 translational positions and 3 rotations), but of these, 3 are considered stabilized by the segment mounting system and generally do not require alignment to optical precision, or are aligned through other means. The remaining degrees of freedom are the position perpendicular to the plane of the mirror (piston) and two rotations around axes in the plane of the mirror (tip/tilt). The foundation of any segmented optical telescope is the detection and correction of these aberrations. The problem of segment rotation about the normal to the center of the segment (called clocking) and the degeneracy between clocking and the azimuthal position of the segment are not treated here. These problems are amenable to other solutions (Acton et al., 2012).

It is important to make clear from the outset that segment cophasing falls under the category of active optics, which involves slow or infrequent corrections to match the mirror to the optimum

shape. This contrasts with adaptive optics, which seeks to minimize the fast effects associated with the turbulent atmosphere. Segment cophasing is often tasked with bringing the segments into alignment from large offsets, rather than continuously measuring and maintaining their position. The Keck telescopes, the most well known telescopes with segmented primary mirrors, are phased only after a segment has been swapped or when the segment alignments are expected to have degraded substantially; phasing is not part of routine observing.

Some cophasing techniques are used routinely on telescopes. Among the most common are modified Shack-Hartmann sensing (Chanan et al., 1998, 2000) and modified curvature sensing (Rodríguez-Ramos and Fuensalida, 2001; Chanan et al., 1999), and both have shown great success. These approaches are generalizations of traditional wavefront sensing techniques, utilizing physical optics to model the effects of diffraction from a discontinuous surface. However, these methods suffer from some disadvantages and are far from ideal. Both utilize dedicated phasing cameras, so the primary mirror is optimized for a camera that is not used for science. Some require relative motion between the primary mirror and the camera, increasing the complexity of the operation.

Our proposed method is Fizeau Interferometric Cophasing of Segmented Mirrors (FICSM), first developed in Cheetham (2011). We utilize the increasingly widespread technique of Sparse Aperture Interferometry (Tuthill et al., 2000; Monnier et al., 2009) to develop a conceptually and operationally simple cophasing plan that avoids many of the disadvantages mentioned above. In particular, Non-Redundant Aperture Masking (NRM) is used here to illustrate the method, but the process is general and applicable to any form of sparse aperture interferometry.

It should be stressed that NRM allows cophasing only for those mirrors behind the mask holes. Options to use NRM to cophase an entire mirror include rotating the mask or utilizing multiple aperture masks. Another option to implement FICSM involves tilting primary mirror segments to different pointing origins, generating interference patterns from entire segments, known as segment tilting interferometry. In this paper, we deal solely with the application of FICSM to NRM imaging, building the basics of the method around one of the simplest applications of sparse aperture interferometry.

By fragmenting the telescope pupil into a non-redundant array of subapertures, every set of interference fringes can be traced to a unique pair of subapertures, corresponding to unique regions on the primary mirror. Information obtained from the fringes present in the images can then be used to infer the state of the mirror segments to interferometric precision.

An N hole aperture mask exhibits $n_b = N(N-1)/2$ baselines (or hole pairs). For the case of a non-redundant array geometry, each baseline produces a fringe pattern at a unique spatial frequency, hence the number of baselines is greater than the number of holes when $N > 3$. The distinguishable fringe patterns comprising such an interferogram are most readily studied in the Fourier plane (or image spectrum), where the amplitude and phase at any given point for which there is power can be termed the complex visibility on that specific baseline. The square of the absolute value of the image spectrum is referred to as the power spectrum, and we note that NRM often does not fill the Fourier plane completely, in which case only a subset of the available spatial frequencies passed by the unocculted primary mirror are measured by a single NRM image.

In order to illustrate the potential of FICSM as a cophasing strategy, we explore an application to the JWST. As a segmented mirror space telescope, there is the added risk of failure of dedicated

hardware. Both currently adopted cophasing techniques rely on the NIRCam instrument, so a failure of that instrument would be catastrophic to the mission. Alternative cophasing methods must use existing hardware on JWST, and be able to phase the mirror from an initial state with a maximum of $100\,\mu$m segment pistons to a state with a final root-mean-square (rms) wavefront error of 100 nm to maximize telescope performance (Long, 2006). To comfortably test this range, we opt for a maximum initial segment-to-segment piston error of $150\,\mu$m.

A non-redundant aperture mask is planned for the NIRISS instrument (Doyon et al., 2012), allowing this science camera to be used with FICSM to cophase JWST. However, combining FICSM with segment tilting interferometry would allow all mirror segments to be phased using any of the imaging science cameras planned for JWST (Sivaramakrishnan et al., 2012).

Phasing segmented mirrors with NRM

A non-redundant mask has the special property that each baseline vector is unique, and therefore produces power in a unique and separately isolated region of the Fourier plane. This has two critical consequences. Firstly information extracted from interferograms is unambiguous: A Fourier datum can be uniquely identified with the baseline from which it arose. This is not the case for a redundant aperture, where this mapping is an ill-conditioned inverse problem, and therefore possesses no general solution. Following Lloyd et al. (2006), we refer to the helpfully segregated areas of signal in the Fourier domain delivered by NRM as *splodges*. Secondly, the information extracted from each splodge is uniquely related to a pair of mask holes, and therefore to two regions on the primary mirror.

These features make it immediately apparent that an NRM-inspired approach offers a novel solution to the problem of phasing segmented primary mirror telescopes. Information extracted from interferograms taken with the science camera can be directly related to the phase structure of specific points on the wavefront at the pupil. By placing the mask such that each hole exposes the surface of a single primary mirror segment, one exposure can deliver independent information about the phases of all exposed segments simultaneously. Moreover, since the number of hole pairs (or baselines) usually greatly exceeds the number of holes, a single image provides multiple measurements to constrain the cophasing of each mirror. Due to the over-constrained nature of this mapping between baseline phases and the mirror glass, errors due to wild data points can be identified and eliminated by enforcing self-consistency on the solution.

At the outset of our cophasing problem all segments are assumed to have unknown errors in both tip/tilt and piston. It is important that our cophasing strategy is able to identify and separate the effects of these two errors, because under some circumstances they can produce similar signals. The key to separating tip/tilt from piston-induced errors in our method is to use images taken with both a narrow and a broad optical bandwidth filter. The two different cophasing error terms then exhibit quite distinct behaviors and can be readily discriminated, as described below.

Our method utilizes three observables readily extracted from the splodges in the interferogram image spectrum: (1) the baseline phase; (2) the fringe power; and (3) the phase ramp or slope across the splodge. The effects of piston and tilt on these three observables extracted from an NRM image are illustrated in Fig. 2.1. Without any aberrations, interferograms give high contrast fringes (as seen in 1a, 1g) with zero phase (1d, 1j). After applying piston errors, the fringes move and (for the broadband case) begin to blur (1b,1h), resulting in a constant phase (in the

Table 2.1: Effects generated by our two classes of segment alignment errors (tilt and piston), on different fringe observables for Narrowband (monochromatic) and broadband interferograms.

	Narrowband Image			Broadband Image		
	Fringe Power	Phase (center)	Phase Slope	Fringe Power	Phase (center)	Phase Slope
Tilt Error	Decrease	No Effect	Yes arb. ramps	Decrease	No effect	Yes arb. ramps
Piston Error	No Effect	Cyclic phasor	No Effect	Decrease	Cyclic phasor	Yes radial ramps

narrowband case, 1e) or radial phase slopes (in the broadband case, 1k) across the corresponding Fourier splodges. After applying tilts to the mirrors, the centroids of the Airy patterns from each aperture move, yet the fringes remain centered where the patterns overlap (as seen in 1c, 1i). This causes a linear phase ramp across the corresponding splodge in the Fourier plane regardless of bandwidth (1f,1l). Unlike the case for piston however, these slopes are not necessarily radial, instead following the direction of the arbitrary tilt errors.

Table 2.1 summarizes the expected effect on the observables recovered from analysis of any given splodge in the image spectrum for a given type of alignment error of the mirror. Perhaps the most critical thing to note is that for the case of a monochromatic image, the effects of tilt and piston are entirely independent and separable. A monochromatic image, or a narrowband image (e.g. using a filter with 1% fractional bandwidth) will allow tilt to be measured in isolation directly from the phase ramps across each splodge in the Fourier plane. After removing tilts, a broadband image (e.g. using a filter with 4.5% fractional bandwidth) will allow measurement of the pistons from the shape of the amplitude and phase distributions in the Fourier plane. As we show below, this step has a remarkably wide single step capture range. Finally, the fringe phase measured at the center of the splodge can be used for fine alignment to sub-wavelength precision.

2.1.2 Mathematical basis

In order to understand the processes behind FICSM, it is important to have an analytical model of the optical setup. The intensity distribution at the detector can be derived using simple Fourier optics. A diffraction limited imaging system is assumed, with the only optical aberrations considered being piston and tip/tilt applied to sub-apertures. Additionally, the imaging camera is assumed to well sample the interference fringes at the wavelengths used.

Consider the telescope pupil as being partitioned into N identical non-overlapping subapertures with uniform and identical reflectivity. We observe a point source through a filter such that the spectrum of the incident light is described by $f(\lambda)$ (energy per wavelength interval per square meter). The combined intensity distribution on the detector expressed in terms of the field (E) at each wavelength will be given by Eq. 2.1 below. We define (ξ, η) to be the coordinates in the image plane (expressed as angles on the sky), and (x, y) to be the coordinates in the pupil plane

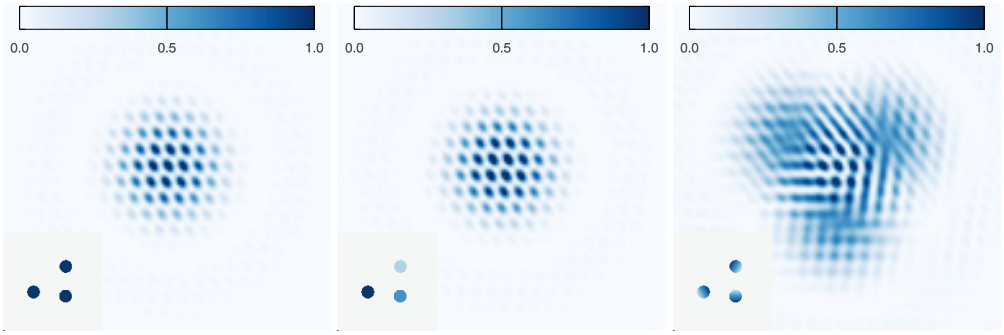

(a) Narrowband image. (b) Narrowband image with piston. (c) Narrowband image with tip/tilt.

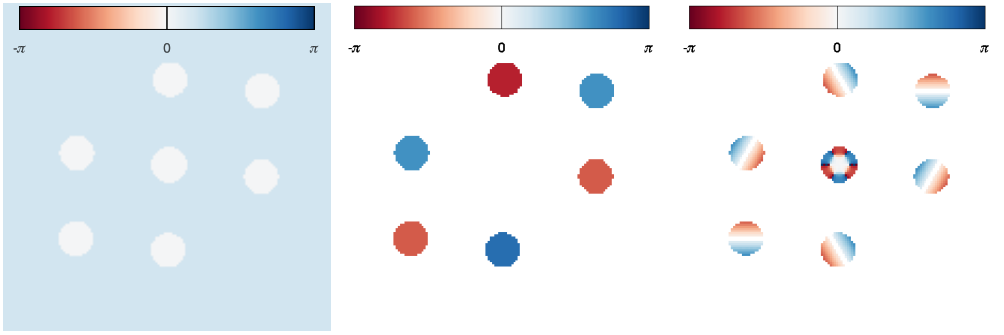

(d) Narrowband phases. (e) Narrowband phases with piston. (f) Narrowband phases with tip/tilt.

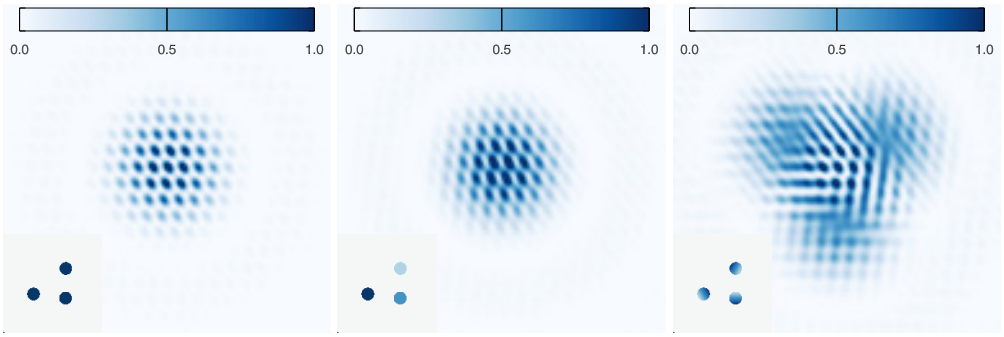

(g) Broadband image. (h) Broadband image with piston. (i) Broadband image with tip/tilt.

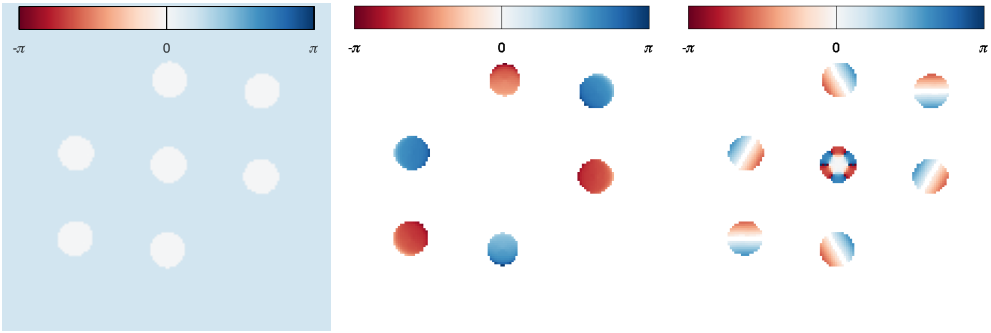

(j) Broadband phases. (k) Broadband phases with piston. (l) Broadband phases with tip/tilt.

Figure 2.1: Simulated images generated from a 3 hole mask (inset: phases added in the pupil plane) and their corresponding Fourier phase spectra, illustrating the effects summarized in table 2.1. Note that the fringes (and splodges) in narrowband images in the absence of aberrations have zero phase, and so the background has been darkened to show the splodge outlines.

(in meters).

$$I(\xi,\eta) = \int_{\lambda_1}^{\lambda_2} f(\lambda)\,|E(\xi,\eta)|^2\,d\lambda, \tag{2.1}$$

where λ_1 and λ_2 are the extremal wavelengths of the filter's bandpass.

By the principle of superposition, the field E can be expressed as a sum of the fields E_i from each subaperture. We write the shape of each subaperture as $C_i(x-x_i, y-y_i)$, where the hole center is (x_i, y_i), and write its piston as p_i and tip/tilt (expressed as mirror gradients) as (m_i, n_i) in the (x, y) directions. For circular holes, $C_i(x-x_i, y-y_i)$ would be a uniform disk with radius r_i. We can then write each E_i as the Fourier transform ($\mathcal{F}$) of the subaperture function, which becomes:

$$E_i = e^{\frac{4\pi i}{\lambda}p_i}\mathcal{F}[C_i(x-x_i, y-y_i)e^{\frac{2\pi i}{\lambda}(m_i x + n_i y)}]. \tag{2.2}$$

Here we measure piston as a physical height of a segment, so the wavefront error (or optical path difference) is twice this value.

In order to evaluate this Fourier Transform we can use the Shift Theorem for Fourier Transforms (Bracewell, 1965). We use it twice; once to incorporate the shifting due to the location of the subaperture away from the origin, and once in reverse to include the linear phase ramp term inside the Fourier transform caused by tip/tilt.

This leads to the analytical result for E_i shown in Eq. 2.3. $A_i(\xi - m_i, \eta - n_i)$ is the Fourier Transform of the subaperture function C_i, shifted in the image plane (relative to the centroid of the image intensity distribution) due to the tilt of mirror i. The phase term due to piston is unaffected by the Fourier Transform.

$$E_i(\xi,\eta) = e^{\frac{2\pi i}{\lambda}(2p_i - x_i\xi - y_i\eta)}A_i(\xi - m_i, \eta - n_i) \tag{2.3}$$

In the special case of circular holes, we can use the familiar result for the Fourier transform of a uniform disk shown in Eq. 2.4. When using other subaperture shapes this term must be replaced by the appropriate Fourier transform. Hexagonal segments, or shapes with an arbitrary number of straight edges, possess analytical Fourier transforms (Sabatke et al., 2005). The phase terms will remain the same.

$$\begin{aligned} A_i(\xi - m_i, \eta - n_i) &= \mathcal{F}[C(x-x_i, y-y_i)] \\ &= \frac{r_i J_1\left(\frac{2\pi r_i\sqrt{(\xi-m_i)^2+(\eta-n_i)^2}}{\lambda}\right)}{\sqrt{(\xi-m_i)^2+(\eta-n_i)^2}} \end{aligned} \tag{2.4}$$

In general, the intensity distribution can then be written as the sum of the patterns generated from each pair of subapertures (with * denoting a complex conjugate):

$$
\begin{aligned}
I(\xi,\eta) &= \int_{\lambda_1}^{\lambda_2} f(\lambda) \sum_{i=1}^{N}\sum_{j=1}^{N} E_i E_j^* d\lambda \\
&= \int_{\lambda_1}^{\lambda_2} f(\lambda) \sum_{i=1}^{N}\sum_{j=1}^{N} I_{i,j} d\lambda, \qquad (2.5)
\end{aligned}
$$

where the E_i are given by Eq. 2.3.

The $I_{i,j}$ terms then correspond to the fringes generated from interference between subapertures i and j. In the special case $i = j$ this reduces to a form of the familiar Airy pattern shifted due to the tilt on the mirror associated with that subaperture. In the case $i \neq j$, this gives interference fringes etched into the overlap of the two shifted Airy patterns from subapertures i and j, with an added phase due to the difference in piston.

We can express the interference terms in the image plane intensity, $I_{i,j}$, using En. 2.6:

$$
I_{i,j} = e^{\frac{4\pi i}{\lambda}(p_i - p_j)} e^{-\frac{2\pi i}{\lambda}(\xi(x_i - x_j) + \eta(y_i - y_j))} A_i(\xi - m_i, \eta - n_i) A_j^*(\xi - m_j, \eta - n_j). \qquad (2.6)
$$

Clearly, the phase terms disappear when $i = j$, giving the familiar Airy pattern.

Writing the intensity distribution in this form immediately shows the effect of piston and tip/tilt on the interference fringes. A piston difference between the two mirrors will shift their fringe off the image's intensity centroid. This fringe phase shift scales with wavelength. For a nonzero filter bandwidth, fringes at different wavelengths will no longer add in phase since they will be shifted away from the origin by different distances. This results in a decrease in fringe amplitude and a fringe blurring known as bandwidth smearing, as seen in Fig. 2.1. Since the difference between the two extremal wavelengths λ_1 and λ_2 is small compared to the wavelengths themselves, the difference in phase between the fringes changes over a much larger scale, characterized by the coherence length of the filter,

$$
L_c = \frac{\lambda_c^2}{\Delta\lambda}. \qquad (2.7)
$$

Here $\Delta\lambda$ is the full width at half maximum (FWHM) of $f(\lambda)$ and $\lambda_c = (\lambda_1 + \lambda_2)/2$. Since the fringes are affected by relative piston only, the zero point of the pistons is unspecified. It can be chosen to be convenient for the descriptions of segment positioning.

2.1.3 The basis of the FICSM algorithm

In principle, a single interferogram taken through a non-redundant mask with a filter of non-zero bandwidth is sufficient to measure both tilt and piston aberrations. However these two aberrations can deliver similar signatures, and in the presence of other real world imperfections such as read-out noise and telescope jitter, a robust strategy to extract cophasing information requires further complexity. The modifications required will depend upon the specific application (e.g. levels of noise, specifics of filters available etc), and must be developed through simulation. In the following sections we illustrate the FICSM method by applying it to JWST. Its use in other contexts should require further (straightforward) modifications.

Both mathematical simulation and physical intuition tell us that in the monochromatic case, two of our three observables – fringe power and phase slopes – are sensitive only to tilt errors (as seen in Table 2.1). These may therefore be measured in isolation and corrected to high precision, so that polychromatic images may then be employed to determine piston errors alone. Because of the complex way in which the shape of both the subapertures and the filter bandpass modify the observables, it turns out that in general a unique signal is imprinted on the phase and amplitude structure which may be recorded out to very large piston offsets. Capture ranges of tens to hundreds of microns (several coherence lengths) are enabled by the complex, non-repeating nature of these signals. At the final step, measuring the phase itself (rather than phase slopes) empowers sensitive metrology to achieve fine-adjustment of segments which are already cophased to within one wavelength.

Measuring tilts

Tilts may be measured from a single monochromatic (in practice narrowband) image in two steps: a coarse measurement for each baseline, and a fine measurement for each subaperture. A coarse step is performed to ensure the fitting procedure in the fine step converges to the global minimum. The phase slope for any splodge is governed by the average of the tilts of the two mirrors that comprise that baseline. This is due simply to the fact that the interference fringes are located halfway between the two subaperture diffraction patterns, and position in the image plane is directly related to phase slope in the Fourier plane. This makes measuring the tilts relatively simple: the phase slope across each splodge is measured, immediately yielding a baseline mean tilt. The ensemble of measurements for each baseline are then converted to tilt estimates for each subaperture. The mathematical procedure to accomplish this is also used in identical context for piston measurements, and we have therefore dedicated a separate Section 2.1.3 to discuss it.

In order to refine the measurements, a second fine-tuning step is performed using least squares fitting. The fitting is performed on the images themselves rather than the image spectrum to reduce computational time, since Eqs. 2.5 and 2.6 give a direct way to compute the intensity distribution of the image. Non-linear least squares fitting is then performed using the goodness of fit parameter (χ_I^2) shown in Eq. 2.8. The unknown parameters for this fit are the mirror tilts and the constant phase offsets for each baseline caused by piston. Each iteration requires generating a new simulated image. This fitting is straightforward; the solution is a clear global minima, and generally requires approximately 10 iterations. This fine-tuning step also relies indirectly on the phase slope.

$$\chi_I^2 = \sum_{\xi,\eta} |I_{model}(\xi,\eta) - I_{measured}(\xi,\eta)|^2 \tag{2.8}$$

The tilt measurement process relies on the interference fringes, and so the capture range of this step is the maximum separation of the subaperture diffraction patterns that still allows some measurable interference between them.

Measuring piston

This procedure is more involved than that for measuring the tilts, due to the complicated relationship between the complex visibilities and piston. A two step process is again employed, consisting of a coarse measurement for each baseline and a fine measurement for each subaperture, measured relative to the chosen reference (in this case, one of the segments). This is motivated by the two different scales resulting from the effects of piston; changing the piston on the scale of a wavelength changes the phase across each splodge by an approximately uniform amount and leaves the amplitude roughly the same, while changing the piston on the scale of a coherence length changes the shape of both the phase and amplitude function across each splodge. The role of the filter coherence length here is similar to that used in understanding the limits of positioning tolerances in the case of free-flying interferometers (Allen, 2007).

The coarse measurement procedure consists of comparing the phase and amplitude distributions in the image spectrum to a "lookup table" of distributions covering a range of pistons. Calculations are done in the Fourier plane, so that measurements for each baseline can be done separately. The data in the lookup table is generated once and saved prior to the phasing process, since it will depend only on the specifics of the instrumentation (mask and camera optics as well as the bandpass of the filter). This lookup table contains the complex visibility of each point on each splodge as a function of piston. The entries must be spaced by less than one wavelength to ensure that the fine step converges to the correct solution. In practice, a sampling density of 4 simulations per wavelength has been found to be sufficient.

The actual phase at any spatial frequency changes much too quickly as a function of piston for a coarse, large capture range measurement. To overcome this problem, only relative phase is used. The phase at the center of each splodge is subtracted from the entire splodge. This process is reminiscent of differential phase measurements common in interferometry, however in this case the signal is entangled with both spatial structure and phase slopes due to residual tilts. For each baseline, this modified version of the visibility distribution (V) of the splodge is compared to each theoretically generated one from the lookup table using the goodness-of-fit parameter (χ^2_V) shown in Eq. 2.9. The (u, v) coordinates refer to the frequencies in the (ξ, η) directions of the image.

$$\chi^2_V = \sum_{u,v} |V_{model}(u, v) - V_{measured}(u, v)|^2 \tag{2.9}$$

In order to ensure that the coarse estimate is accurate, this process is performed independently for two images in different observing bands. The visibility distributions at each piston will depend on the filter bandwidth and central wavelength, and so adding the χ^2_V distributions of the two images effectively eliminates near-degeneracies which can be present for a single filter alone, resulting in a much more robust coarse piston estimate. The point of minimum total χ^2_V for each baseline is then recorded as the coarse measured piston difference.

Since the equations for the image depend only on the piston differences, the "zero" piston position is arbitrary and undefined. For this reason, the piston for one of the mirrors is set to zero, and the other mirrors measured relative to it. In practice, any condition on the zero piston position could be set, including setting the average piston to be zero to minimize mirror motion. The piston differences measured for each baseline then need to be converted to measurements for each hole. This procedure is similar to that for tilts, and is described in section 2.1.3

After the coarse phasing step described above, a nonlinear least-squares fine fitting procedure is applied to one of the interferograms, with the piston values as the only unknown parameters. The coarse value is used as a starting parameter for the fit, and the procedure and misfit statistic for fitting is the same as for tilts. This procedure generally converges in approximately 10 iterations, and requires generating new simulated images each iteration.

This fine fitting step is equivalent to finding the absolute phase of each splodge in the Fourier plane, or lining up the fringe peaks in the image plane. This results in the χ^2 space having local minima centered on the correct piston and spaced by λ. In order for this step to converge to the correct solution (so that the correct fringes line up), the coarse measurement must be accurate to within half a wavelength. Occasionally this condition is not met, leading to a final piston measurement that is an integral number of wavelengths (usually 1) from the actual value. While this is a rare occurrence (observed in one out of 100 complete simulations below), they are easily recognized and rectified.

In order to unambiguously identify these errors, the two images used for the coarse piston measurement can both be used in the fine step. The fine piston measurement will always ensure that the piston is measured to within an integral number of wavelengths. Since the two images are at different wavelengths, a disagreement between the measured values indicates that one or both are inaccurate. Only when both measurements are correct will they agree. Knowledge of the two wavelengths also allows us to immediately recover the actual piston in the case where they do disagree. The difference between the piston measurements will be equal to $c\lambda_2 - d\lambda_1$, where c and d are unknown integers (usually -1, 0 or 1). This equation has a unique solution when assuming small c and d, and these can then be multiplied by the wavelength and subtracted from the measured piston to reconstruct the actual piston.

Turning baseline data into estimates for mirrors

The phasing strategy described above requires a method for converting quantities recovered from each baseline into estimates for each subaperture. As previously discussed, the number of baselines is generally greater than the number of subapertures so that one image provides multiple constraints for each mirror. Enforcing consistency on both the tip/tilt and piston measurements dramatically reduces the impact of outliers and measurement errors. In order to turn the baseline measurements into estimates for each subaperture, a method to calculate the least squares solution is required. We have employed the method used in the Keck telescope cophasing algorithm (Chanan et al., 1998), which is based on a singular value decomposition from Press et al. (1986).

We have a system of equations relating the pistons on each mirror p_i to the measured piston difference $\delta_{i,j}$ between mirrors j and i:

$$\delta_{i,j} = p_j - p_i \tag{2.10}$$

Since all measurements are of relative piston, we also impose a constraint that one of the mirrors be defined to have zero piston. This allows all of the mirror pistons to be expressed relative to a single reference point. In practice it may be more useful to require the total piston be zero, to minimize mirror motion.

Similarly, turning to the tip/tilt problem, we have equations for the measured tip/tilt $M_{i,j}$ for each baseline in terms of that on each mirror t_i:

$$M_{i,j} = \frac{1}{2}(t_i + t_j) \tag{2.11}$$

Since we measure tilts in two directions, we have a separate set of equations for each. This method is described for one, and is repeated for the other direction.

For the remainder of the method, pistons and tilts are treated identically, and so only the equations for pistons are shown. The equations for tilts are given by replacing δ with M and replacing p with t.

For an N hole mask, these are systems of $n_b = \frac{N(N-1)}{2}$ equations in N unknowns, and can be expressed in matrix form as:

$$A\mathbf{p} = \delta \tag{2.12}$$

Singular value decomposition allows the matrix A to be expressed in the form $A = U\ w\ v^T$, where w is a diagonal matrix with diagonal elements (w_j). This leads to the least squares solutions for piston, given by (Press et al., 1986):

$$p = v\ \mathrm{diag}(1/w_j)\ U^T\ \delta \tag{2.13}$$

where $\mathrm{diag}(1/w_j)$ is the diagonal matrix with diagonal elements $1/w_j$.

As mentioned above, the fact that there are more measurements than unknowns provides a way of checking the consistency of the measurements. Systems to accomplish this have been implemented for both piston and tilts. They work by combining measurements from several baselines to get an estimate of what the measurement for a particular baseline should be. All distinct combinations are calculated, and the actual measurement is replaced by the median measurement if it is beyond two wavelengths from the rest.

For example, an estimate for the measured piston difference $\delta_{i,j}$ can be calculated from two other baselines, since:

$$\begin{aligned} \delta_{i,j} &= p_j - p_i \\ &= p_a - p_i + p_j - p_a \\ &= \delta_{i,a} + \delta_{a,j} \end{aligned} \tag{2.14}$$

2.1.4 Cophasing JWST: a numerical case-study

Quantitative metrics of the success of this technique (such as capture range and residual error) require a specific case with real world error sources and limitations to be modeled, otherwise it is mathematically possible to cophase in a single step with arbitrary precision. A simulator was written in the IDL programming language capable of modeling the JWST primary mirror and producing images subject to various imperfections and noise processes. Our cophasing algorithm then performed the following steps:

1. Using the specifications of the telescope, optics and detector, the coarse piston lookup table is computed and loaded.

2. The initial state of the mirror is prepared by applying a random tip/tilt and piston to each segment.

3. Cophasing begins by taking a narrow bandwidth image using the current mirror state.

4. The image is processed with the tip/tilt fitting program, and the best-estimate tilts corrected in the present pupil.

5. Images in two different broad bandwidth filters are taken.

6. The two broad band images are processed with the piston fitting program, and the results compared.

7. If they agree, the present pupil is corrected for the mean of the two measurements.

8. If they disagree, the two measurements are used to reconstruct the true piston, which is then used to correct the pupil.

9. Steps 3 – 8 are repeated once.

10. The final fit residual pistons are computed by comparison with Step 2.

Here the "narrow" bandwidth image would ideally approach monochromatic, but realizing that we must work with commonly-available optics, we have developed the strategy so that a 1% fractional bandwidth can easily be made to work in simulations. Although 1% may sometimes be too broad to be approximated as monochromatic for the purpose of tilt fitting (increasing misfit residuals), a relatively straightforward cure is to repeat the fitting sequence as indicated at Step 9. Simulations have shown this to deliver very robust results, incurring a proportional penalty in increased observing time and algorithmic complexity. Turning to the broadband filters, fractional bandwidths as small as 4.5% have been shown to work in simulations. These numbers are rough guides, but the width of the narrow bandwidth filter will affect the accuracy of the tip/tilt fitting, while the widths of the broad bandwidth filters will define the capture range and accuracy of the piston fitting by changing the coherence length. The final accuracy of the piston fitting will also depend on the central wavelengths of the broad bandwidth filters.

To summarize, the entire cophasing process defined above requires one narrow and two broad band images with a tilt and a piston move, all performed twice — a total of 6 images and 4 segment moves, assuming perfect segment actuation. With real hardware an iterative process might be required to assert desired mirror moves with sufficient accuracy.

Numerical simulations: setup and configuration

In order to explore the capability for the FICSM algorithm to cophase the JWST primary mirror, extensive numerical simulations have been performed. The method was implemented in the IDL programming language. Non-linear least squares fitting steps were achieved using MPFIT, a freely available IDL routine that uses the Levenberg-Marquardt technique. We have chosen the current specifications of JWST's NIRCAM instrument with filter profiles taken from the WebbPSF software (Perrin et al., 2012)). To generate the narrowband image, the F405N filter profile was used,

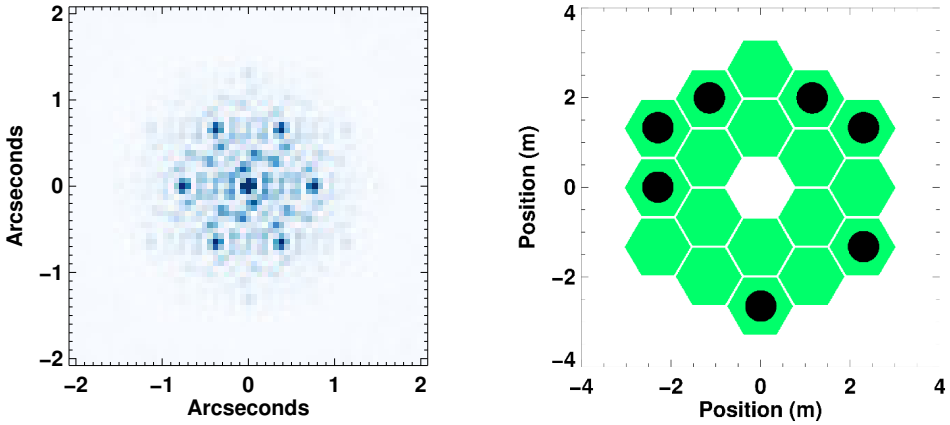

(a) Simulated interferogram.

(b) Simulated JWST mask, overlaid on primary mirror.

Figure 2.2: Left Panel: An example of a simulated interferogram as imaged with the NIRCam instrument using a non-redundant mask. Right Panel: the aperture mask with seven circular holes overlaid on the hexagonal segments of JWST's primary mirror. The envelope of the interferogram is sometimes referred to as the primary beam in synthesis imaging. The shape of the primary beam depends on the hole shape.

while the broadband images used the F430M and F480M filter profiles. The mask used in the simulations is based on one already designed for JWST and described in Sivaramakrishnan et al. (2009), with a few small changes (0.6 m diameter circular holes were used instead of 0.8 m diameter hexagonal holes). The discrepancy in setup for our simulations was motivated only by clarity for the images and plots produced: similar outcomes should apply to both cases. The mask used for the simulations is shown in Fig. 2.2, along with a theoretical image generated using it, while basic data for our simulation setup is given in Table 2.2.

As stated in section 2.1.1, the requirements for a JWST phasing system are a capture range of more than 100 μm in piston, and a final wavefront error of less than 100 nm. To comfortably test the viability of this method, a maximum piston capture range of 150 μm was adopted, measured between any two segments. Using the coherence length of 96 μm from the first broadband filter, this corresponds to more than 3 coherence lengths at the wavefront (6 coherence lengths for the second filter). We adopted a reasonable error budget of a maximum 0.5 arcseconds of tilt, chosen through consideration of the plate scale, 65 mas per pixel. This corresponds to more than 7.5 pixels, and is an estimate of the residual tilts from initial alignment steps rather than an exploration of the capture range of FICSM.

A number of important noise processes were also incorporated into the simulations, namely flat field errors, image jitter and photon noise. The level of noise for each of these processes was set using baseline design specifications for the JWST instrument (Long, 2006). The noise levels were further adjusted over a range around the nominal performance levels so as to explore the expected cophasing accuracy under various scenarios. It is our belief that we have captured the

Table 2.2: Specifications used for simulations

Parameter	Value
Hole Diameter	0.6 m
Number of Holes	7
Plate Scale	65 mas
Narrowband Filter: Name	F405N
Narrowband Filter: Central Wavelength	4.05 μm
Narrowband Filter: Bandwidth (FWHM)	1%
Broadband Filters: Name	F430M and F480M
Broadband Filters: Central Wavelengths	4.3 μm and 4.8 μm
Broadband Filters: Bandwidth (FWHM)	4.5% and 8%

dominant contributions to degrading the accuracy of our algorithm in a flight context. Our specific choice of NIRCAM for these simulations is illustrative; as discussed briefly in section 2.1.5 this technique could be used with the NIRCam short wavelength, NIRCam long wavelength, and MIRI imaging cameras aboard JWST. NIRISS' narrowest bandpass at wavelengths where the image is Nyquist-sampled is of the order of 5%. Further study of the three-filter approach described here will be required to determine the practicability of using NIRISS to perform coarse phasing.

Numerical simulations: results

Both piston and tilt fitting were tested with a fixed capture range by using a random uniform distribution to generate the error terms. This also ensured that the maximum capture range for piston (set by the size of the lookup table) was not exceeded.

The results from running 100 complete phasing simulations under nominal noise conditions can be seen in Fig. 2.3. They used 0.2 pixels (13 mas) of jitter, a standard deviation of 0.1% for flat field errors, and photon noise from 10^9 photons. Errors due to inaccuracy in segment actuator motion were not considered. The cophasing algorithm produced a final rms residual piston of 0.75 nm, and an rms residual tilt of 3.7 mas, showing that we can expect the method to work to well within the accuracy required from the JWST coarse phasing system. By comparison with the 65 mas plate scale of the detector, a tilt of this size would result in a misalignment on the detector of less than 6% of a pixel.

The corresponding total rms wavefront error is 3.65 nm, corresponding to a Strehl ratio of 0.99997 at 4.3 μm using the common approximation $S = e^{-(2\pi\sigma/\lambda)^2}$, where σ is the rms wavefront error and λ is the operating wavelength. This is more than an order of magnitude lower than the 100 nm requirement for coarse phasing the JWST primary mirror, and appears to be achievable with existing hardware and most of its science cameras.

Out of 100 simulations, only one simulation was flagged as having possibly inaccurate results after comparing the piston measurements at the two wavelengths. Both filters were a single wavelength off for each measurement in that simulation, but since the wavelengths were known the correct pistons were reconstructed. However, this proved to be substantially less accurate than di-

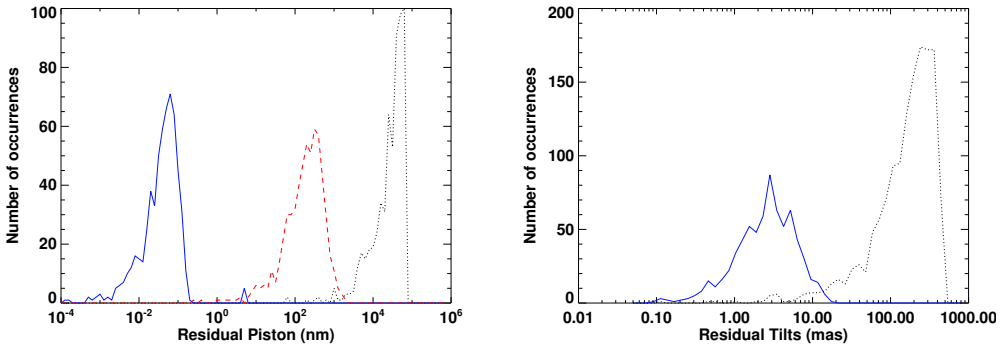

(a) Histogram of residuals from coarse piston (red, dashed line), and coarse+fine piston (blue line) measurement steps, compared with original pistons (black, dotted line).

(b) Histogram of residuals from tilt measurement (blue line), compared with original tip/tilts (black, dotted line).

Figure 2.3: Output residuals from 100 complete cophasing simulations, each with noise as described above. The left panel plots histograms of the initial pistons and the residuals after each step of the piston measurement process. After phasing, one simulation produced visible outliers around 5 nm, while the remainder are well below 1 nm. The right panel shows histograms of the initial mirror tilts, and the residuals after the tilt measurement process. All tilts are reduced to well below a single pixel (65 mas).

rectly measuring the piston, so these points skewed the results. Despite this, the maximum residual piston was less than 6 nm and the wavefront error from that simulation was 11 nm, significantly less than the 100 nm requirement. However, these measurements were detected by the algorithm. A strategy involving a further application of the method whenever this occurs would reduce the residual piston errors to levels similar to the remainder of the simulations, thereby reducing the rms residual piston to less than 0.1 nm.

It is also clear that the tilt residuals do not limit the accuracy of the piston measurements. Plotting the piston residuals against the tilt residuals yields no significant correlation.

2.1.5 Extending FICSM to other configurations

While our simulations have demonstrated the utility of FICSM with NRM, the technique is applicable to any form of sparse aperture interferometry. Since the ultimate goal is to phase segmented mirrors efficiently without the need for dedicated hardware, removing the need for an aperture mask would be ideal. Segment tilting interferometry is a maskless extension of NRM which promises the potential to phase entire mirror arrays. Segment tilting interferometry has demonstrated success in mid-infrared interferometric imaging at the Keck I telescope (Monnier et al., 2009). It works by deliberately repointing subsets of mirror segments to focus at different points within the field of view of the camera. By coaligning and cophasing selected groups of segments to the same pointing origin, sparse-aperture non-redundant interferograms can be generated without the need for a physical mask. The FICSM technique could then be applied to each of these interference patterns, thereby cophasing the subset of segments selected by the pattern. Repeating this

process with differing mirror combinations, taking care to ensure that the segment patterns have some segments in common (so as to stitch the absolute phases to a common surface) would permit the cophasing of any segmented mirror. A more complete discussion is contained in Cheetham (2011). Details of this stitching procedure are telescope- and hardware-dependent. For JWST the operational procedures already developed for stacking all single-segment PSFs at one location in the focal plane (Long, 2006) can be used, with little modification, to stitch the distinct segment patterns together.

As presented here, FICSM has been specifically developed for telescopes such as JWST where it is possible to retrieve Fourier phase information directly from the interferograms. However, this process is made much more difficult when observing on large ground based telescopes through the turbulent atmospheric phase screen, particularly for the longest baselines. Similarly, unexpected large image jitter during JWST's early commissioning stages might require tailoring the subsets of segments that form interferograms to have short baselines, so that the FICSM algorithm can still be used to cophase the telescope. Despite this, options for extending FICSM to work on seeing limited telescopes may be possible; indeed the earlier Keck segment tilting interferometry has shown it can work in the mid-infrared. A phasing strategy which can be employed on ground based segmented telescopes may prove particularly useful for the next generation of Extremely Large Telescopes (ELTs), but determining the efficacy of FICSM applied to the many hundreds of segments in some ELT designs is beyond the scope of this paper.

2.1.6 Conclusions

We present a new technique christened Fizeau Interferometric Cophasing of Segmented Mirrors (FICSM) for cophasing segmented mirror telescopes. The method uses a sparse aperture interferometric approach to measure the piston and tilt aberrations of mirror segments to interferometric precision. Feasibility has been demonstrated with numerical modeling of mirror cophasing applicable to the James Webb Space Telescope with the NIRCAM instrument. Our simulations started with the mirror in an initial state with large errors in piston and tilt (150 μm and 0.5 arcsecond respectively) and incorporated realistic noise sources, yet delivered final residuals of a few nanometers in piston and 10 milliarcseconds of segment tilt – an improvement of more than 5 orders of magnitude. The method can be carried out using any of JWST's scientific imaging cameras. Results were achieved after two iterations through a procedure requiring three exposures and two mirror adjustments each pass. Operational details of the technique follow existing procedures. We conclude that the FICSM technique has the potential to cophase the JWST primary mirror to more than an order of magnitude better than its coarse phasing requirements, and may also be useful to future segmented-mirror telescopes.

Chapter 3

Experimental Demonstration of Mirror Cophasing Techniques

3.1 Laboratory Demonstration of FICSM

To extend the successful simulations of the performance of the FICSM algorithm established in Chapter 2, a laboratory test was performed to demonstrate the fundamentals of the technique and to investigate its performance under more realistic conditions. In the following paper, I present the results of this experiment. The experimental setup was put together by Nick Cvetojevic and myself, by modifying an existing setup constructed by Barnaby Norris. The experiment was performed by myself with supervision by Nick Cvetojevic. Software to control the MEMS array was written by Barnaby Norris, while I completed all data analysis. The paper was substantially improved by comments from all coauthors.

The following manuscript was published in Optics Express (2014) vol. 22, issue 11, p. 12924.

Fizeau interferometric cophasing of segmented mirrors: experimental validation

Anthony Cheetham,[1] Nick Cvetojevic,[1,2,3] Barnaby Norris,[1] Anand Sivaramakrishnan[4] and Peter Tuthill[1]

[1]Sydney Institute for Astronomy, School of Physics, University of Sydney, NSW 2006, Australia
[2]Space Telescope Science Institute, 3700 San Martin Drive, Baltimore MD 21218, USA
[3]Department of Astronomy, Cornell University, 122 Sciences Drive, Ithaca, NY 14853, USA

Abstract

We present an optical testbed demonstration of the Fizeau Interferometric Cophasing of Segmented Mirrors (FICSM) algorithm. FICSM allows a segmented mirror to be phased with a science imaging detector and three filters (selected among the normal science complement). It requires no specialised, dedicated wavefront sensing hardware. Applying random piston and tip/tilt aberrations of more than 5 wavelengths to a small segmented mirror array produced an initial unphased point spread function with an estimated Strehl ratio of 9% that served as the starting point for our phasing algorithm. After using the FICSM algorithm to cophase the pupil, we estimated a Strehl ratio of 94% based on a comparison between our data and simulated encircled energy metrics. Our final image quality is limited by the accuracy of our segment actuation, which yields a root mean square (RMS) wavefront error of 25 nm. This is the first hardware demonstration of coarse and fine phasing an 18-segment pupil with the James Webb Space Telescope (JWST) geometry using a single algorithm. FICSM can be implemented on JWST using any of its scientic imaging cameras making it useful as a fall-back in the event that accepted phasing strategies encounter problems. We present an operational sequence that would co-phase such an 18-segment primary in 3 sequential iterations of the FICSM algorithm. Similar sequences can be readily devised for any segmented mirror.

3.1.1 Introduction

Optical and infrared astronomy has long been dominated by a drive for ever larger telescope apertures. Inevitably, this leads to problems with primary mirror rigidity when a single monolithic mirror is used. This has been ameliorated through the use of a segmented primary mirror, first successfully implemented in the optical and near-IR at the Keck Telescopes and now an integral part of modern large telescope design (Nelson, 1979, 2000; Gilmozzi, 2004).

To function as a primary mirror, all segments must be aligned to conform to a single optical surface, a process known as cophasing. Several methods are currently used today. Chanan et al. (1998, 2000) utilize a modified Shack-Hartmann sensor to measure discontinuous (segmented) wavefronts. Acton et al. (2006, 2007) use a combination of sensing discontinuities between neighbouring segments and focus-diverse phase retrieval (Fienup et al., 1993). When implemented, these methods often require dedicated hardware such as actuated elements and additional optics, which introduce non-common path errors. This means that the final science image on the detector has different aberrations than those sensed by the cophasing strategy. Non-common path errors are a concern for many modern astronomical instruments using active or adaptive optics because they

create the best wavefront quality at the wavefront sensor rather than the science detector, degrading the performance of scientific instruments (Sivaramakrishnan et al., 2008). An approach employed on the Hubble Space Telescope utilizes defocus introduced by moving the secondary mirror (Krist and Burrows, 1995). Such secondary mirror motions increase risk, especially on space telescopes.

We proposed a new cophasing solution that utilises an interferometric approach to overcome many of these challenges (Cheetham, 2011; Cheetham et al., 2012). Our method, Fizeau Interferometric Cophasing of Segmented Mirrors (FICSM), allows a primary mirror to be cophased using any science camera equipped with three filters; usually those already present for the core science of the instrument. This method has obvious applications in space-based segmented telescopes such as the James Webb Space Telescope (JWST) – where the dedicated hardware required by its proven cophasing techniques introduce some risk of single-point failure. JWST will carry two copies of its wavefront sensing camera (NIRCam) to mitigate this risk.

FICSM could also be applied to cophase ground based segmented telescopes with a few modifications. Short integration times on bright stars are required to freeze seeing-induced fringe motion, and a time-series of such phase measurements averaged to separate wavefront distortion terms due to imperfectly-aligned optics from the random phase scatter due to atmospheric turbulence. Preliminary simulations show that this strategy is successful, although further optimizations for the seeing-limited case are possible but beyond the scope of the present paper.

The accepted coarse phasing method aboard JWST, Dispersed Hartmann Sensing (Wirth, 2003), is based on a modified Shack-Hartmann approach with a dispersive element to solve the problem of phase-wrapping. This allows phasing to be accomplished with a science camera. It requires dedicated hardware, and introduces a division of phasing into coarse and fine regimes. FICSM addresses these issues by phasing mirror segments in non-redundant groups. In order to cophase an entire mirror, FICSM either needs to actuate segments or use several pupil masks. A possible alternative to Dispersed Hartmann Sensing for JWST exists (Shi et al., 2004), although it requires a large number of large segment motions. This alternative approach increases mission risk and operational complexity, given that large actuator motions are often insufficiently accurate. Actuator motions required by FICSM lie within JWST's planned actuator use (both range of motion as well as number of moves), as it is a replacement for the stage when every segment point-spread function (PSF) is co-located at one place on the science detector (Acton et al., 2006).

Here we report an experimental demonstration of FICSM using an optical testbed. The three-ring segment pattern of the JWST primary mirror was used, along with potential segment groupings that allow the entire mirror to be phased in 3 steps. In an important extension to previous work, we have eliminated the requirement for a pupil-plane mask in favour of full segment interference patterns, using the proven segment-tilting technique (Monnier et al., 2009). Since FICSM moves segments it is proposed as a commissioning rather than routine phasing method.

Unless otherwise noted, our piston and tip/tilt aberrations are measured at the wavefront rather than on a mirror surface.

3.1.2 Fizeau interferometric cophasing of segmented mirrors

A detailed explanation of FICSM can be found in the literature (Cheetham, 2011; Cheetham et al., 2012), although we present a concise summary of the method below.

FICSM involves directly simulating the effects of piston and tip/tilt on a telescope point spread function (PSF) using collimated starlight, in the case where the primary mirror is made up of a non-redundant array of subapertures (for example, whole segments or holes in an aperture mask). The non-redundancy of baseline vectors connecting every pair of subapertures is essential for this method, as it allows the relative pistons and tilts to be measured from each set of interference fringes which are uniquely separable in the image Fourier transform.

The PSF will consist of an envelope function from each subaperture (an Airy pattern in the case of circular holes), and areas where the envelope functions overlap will host interference fringes with a frequency and direction determined by the separation vector between the two subapertures in the telescope pupil.

The presence of a phase step between two subapertures will cause the fringes for that baseline to shift. Large pistons (on the order of a coherence length) will cause polychromatic fringes to blur. This leads to *bandwidth smearing*, a reduction in fringe amplitude and introduces a distribution of phase that is a complicated yet predictable function of piston. The combination of amplitude and phase distributions produces a unique fingerprint that allows the piston term to be recovered with high accuracy even in the presence of large pistons (up to several filter coherence lengths). By using the distribution of phase and amplitude as a function of spatial frequency in the presence of a polychromatic light source, problems with phase wrapping are avoided.

Introducing a tilt to a subaperture will cause its envelope function to move, both reducing the amplitude of the fringes and introducing a distribution of phase. Our algorithm therefore requires a way to distinguish segment tilts from pistons, as both can produce similar effects.

These effects can be easily separated by measuring tilts using an image taken with a monochromatic source or narrowband filter (simulations show a filter with 1% fractional bandwidth is sufficient). In this case, pistons only contribute as a constant phase offset, with no loss of coherence while tilts produce a simple phase ramp. After tilts have been corrected, a broad bandwidth filter is used to measure the pistons. The amplitude and the shape of the phase distribution allows for a good estimate of the coarse piston, while the average phase allows fine measurement to sub-wavelength precision. To ensure reliability, pistons can be measured using two images taken with different filters. Estimates very occasionally exhibit an ambiguity which can lead to a phasing error of a small integer number (typically 1) of wavelengths, however the use of dual wavelength data completely removes any ambiguity and all such problem cases can be flagged and corrected.

By applying this strategy numerically to a model of JWST NIRCam's long wavelength arm and it's complement of filters, it was shown that FICSM has the potential to phase a mirror from an initial state with 300 μm pistons (corresponding to more than 3 coherence lengths or 70 wavelengths) and tilts as large as 0.5 arcseconds (3.5 λ/D) at the wavefront. After 2 applications of FICSM, the wavefront error was reduced by more than 5 orders of magnitude to 3.65 nm RMS, with RMS pistons and tilts of 0.75 nm and 3.7 mas respectively, corresponding to a Strehl ratio of approximately 0.99997 at 4 μm.

While previous work on FICSM has used circular subapertures (assumed to be in a pupil plane mask), here we employ the hexagonal mirror segments themselves. Since all shapes with straight edges posses analytic Fourier transforms (Sabatke et al., 2005), all that is required is to substitute the Airy pattern for its hexagonal equivalent.

3.1.3 Segment groupings

In order to phase an entire mirror with FICSM, segments must be phased in non-redundant groups. For the case of JWST, these are groups of 3 or 4 segments, as shown in Fig. 3.1. In principle it is possible to cophase several segment groups at once by tilting them to different positions on the detector, but due to the limited range of motion of our mirror segments, demonstration of this was not possible here. Regardless, the groups used allow the entire mirror to be phased in 3 steps if multiple pointings are possible, or 7 steps if not. The blue group in the first step (segments 1, 3 and 5) are phased with respect to each other first, and then with the remainder of the segments in the third step. These three segments would allow the telescope to guide on a phased PSF in the second step, to improve telescope guiding during its early stages of commissioning. The short baselines between segments 1, 3 and 5 may enable the phasing process to be more robust to telescope jitter, since the fringes formed by this group are correspondingly wide. If multiple pointings are not possible, telescope guiding can be accomplished on a phased PSF after the first step even without this group, and so it can be removed.

Due to the fact that the spatial frequency of interference fringes scales with wavelength, large bandwidths cause a greater range of frequencies to be associated with each baseline - a process known as “bandwidth smearing”. This can cause redundancy, as a spatial frequency associated with one baseline at one wavelength can be equal to the spatial frequency associated with another baseline at a different wavelength. For this grouping of segments, a manageable level of redundancy should be provided at fractional bandwidths up to 25% of the central wavelength. Thus FICSM enables any of JWST’s three scientific imaging cameras to cophase JWST, using their standard complement of filters.

The sequence of segment groupings comprising the phasing strategy illustrated in Fig. 3.1 minimises mirror movement, and mitigates against unexpectedly high jitter when guiding on a broad, single-segment PSF at the start of the commissioning operations. The first group of green segments are initially phased together to define a single ”zero” piston position, then all other segments measured relative to this phased group. This avoids the problem of having to move whole groups of phased segments at the end of the phasing sequence. This segment grouping scheme allows an 18 segment mirror to be cophased by moving each segment a maximum of 8 times, with the majority of segments requiring 6 or fewer moves, assuming perfect actuation. In reality larger steps might require iteration similar to JWST’s current segment stacking plans (Acton et al., 2006)

Choosing optimal segment groupings to weave into a phasing sequence requires consideration of a number of factors. Incorporating as many segments as possible in each group allows for a smaller number of steps and groups, but non-redundancy here enforces an upper limit of 4. Starting with an initial group to act as a zero point for subsequent groups decreases the number of actuator moves required, but does not allow for multiple groups to be phased in the first step. The minimum number of such groups also increases with the number of mirror segments.

3.1.4 Experimental setup

The backbone of our testbed was a 37-element Micro-Electro-Mechanical System (MEMS) segmented mirror from IrisAO. The gold-plated mirrors are arranged in a 4-ring honeycomb config-

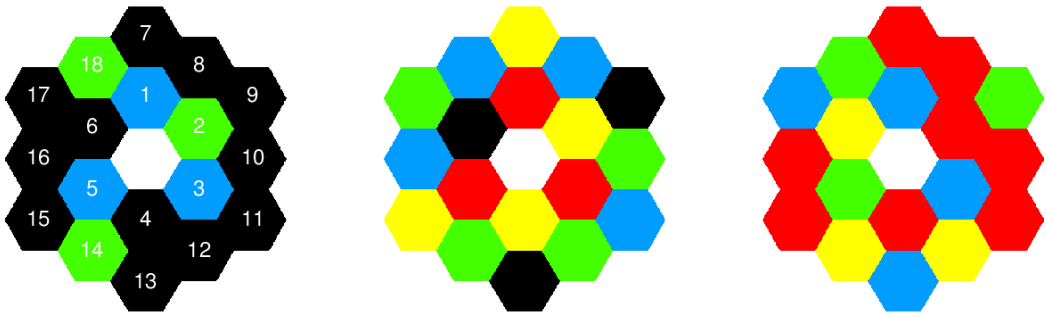

Figure 3.1: The segment groups used for this demonstration. Each image shows several segment groups that are phased simultaneously. At each step, each group is shown in a different colour. Red segments are phased but unused in that step and could be used for telescope guiding (to ensure the PSF remains stationary), while black segments are unphased and unused in that step. Each group produces an interference pattern with acceptable levels of redundancy at bandwidths of up to 25% of the peak wavelength. If multiple pointings are possible this allows the entire mirror to be phased in the three steps shown. If this is not possible, the first blue group is unnecessary and the procedure is accomplished in 7 steps. The segment numbering scheme is also shown superimposed on the segments in the first step.

uration and can each be adjusted electronically in piston, tip and tilt to a precision of a few nm (Helmbrecht et al., 2006). Only the 18 segments in the two middle rings were used, to conform to the layout of the JWST primary mirror. This was accomplished by tilting the remaining segments to a large beam deviation such that they did not contribute to the PSF. An opaque mask matched to the segment layout was also placed in front of the MEMS chip to block light reflected from other surfaces, minimising the contribution of stray light to the final image.

The MEMS mirror used in this test was expected to have high optical quality, with 6-20nm rms figure error after removal of piston, tip and tilt aberrations (Helmbrecht et al., 2006). This is similar to the measured segment figure error of the JWST primary mirror segments (13.5 nm rms, Daniel et al., 2012), both of which are significantly better than the Keck segments (80 nm rms, Neyman et al., 2007). When combined with the operating wavelengths ($\sim$ 500 nm for this setup, $\sim 4\,\mu$m for JWST), the phases introduced by segment figure errors in this setup are larger than those expected during JWST phasing and equivalent to phasing the Keck telescopes at 6 μm. Simulations show that segment figure errors may set an upper limit to the accuracy obtainable through FICSM, but including known segment errors into the image simulation code has been shown to effectively ameliorate this problem.

A schematic diagram of the experimental setup is given in Fig. 3.2. Collimated light was reflected off the MEMS mirror and then focused through a 200 mm focal length achromatic doublet lens (Thorlabs AC254-200-A-ML) onto a Point Grey CCD optical camera. The combination of lens focal length and CCD pixel size ensured the PSF was sampled at more than twice the Nyquist limit, but it is important to note that FICSM operates as long as the sampling is at or above the

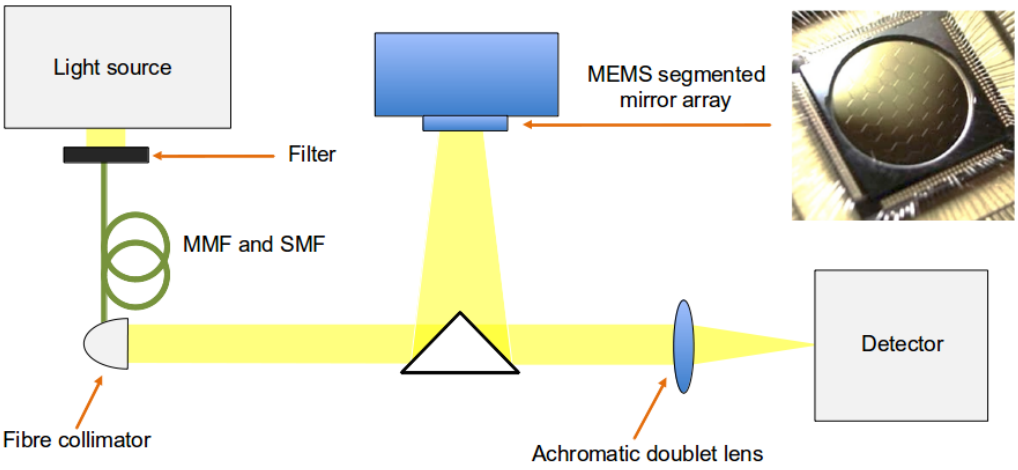

Figure 3.2: A schematic overview of the experimental setup. For the broadband images, light from a halogen lamp was passed through a filter into a multimode fibre, then coupled into a single mode fibre connected to a fibre collimator. For the narrow band images, a HeNe laser was connected to the fibre collimator using a single mode fibre only. Collimated light was then reflected off the MEMS mirror array and through an achromatic doublet lens onto a detector. MEMS inset image from Helmbrecht et al. (2011).

Nyquist frequency. Our test was performed in the optical band (500-700nm), to increase the amount of wavefront error possible from the limited MEMS absolute range of motion (max. 5μm in piston).

As described previously, to ensure reliability FICSM requires two broad bandwidth filters and one narrow bandwidth filter. For our demonstration we used a 550 nm (green) and a 650 nm (red) filter, both with a 40 nm bandwidth. A halogen lamp served as a light source for these filters. For our narrow filter we opted for the convenience of a HeNe laser, with a 633 nm central wavelength and negligible bandwidth. This avoided problems with source brightness when combining the halogen lamp with a narrowband filter.

The filters were placed directly between the lamp and a multimode fibre, which was then coupled into a single mode fibre to serve as an analogue of a point source (unresolved star) seen by a telescope. Light from the single mode fibre was collimated using an off-axis parabolic reflective collimator, with the beam then steered onto the MEMS mirror array.

While the 4.0 mm diameter of our Gaussian input beam slightly overfilled the 3.5 mm MEMS mirror array, variations in intensity between segments were significant enough that the intensity profile could not be considered to approximate uniform illumination (as would be expected for a star). To correct for this, the amplitudes of each set of fringes was measured from the narrowband images, as a fraction of their theoretical amplitudes. These multiplicative factors were then applied

Table 3.1: Initial and final positions of each segment, measured at the wavefront.

	Piston (μm)		Tip (mrad)		Tilt (mrad)	
Segment	Initial	Final	Initial	Final	Initial	Final
2	1.70	0.00	0.78	-0.06	-0.76	-0.04
3	0.00	0.00	0.06	0.02	0.60	0.16
4	3.10	0.00	0.60	0.14	-0.30	0.18
5	-1.50	0.02	0.26	-0.14	0.34	-0.14
6	1.78	0.00	-0.14	0.04	-0.70	0.12
7	-0.64	-0.02	-0.16	-0.12	0.34	-0.14
8	3.20	0.04	-0.42	-0.08	-0.62	-0.08
9	-0.90	0.02	-0.28	0.00	-0.42	-0.02
10	1.78	0.00	0.40	-0.12	0.76	0.02
11	3.10	0.00	0.36	-0.10	0.80	0.20
12	-0.10	0.00	-0.44	0.14	-0.64	0.10
13	3.90	0.00	0.28	0.00	-0.44	0.06
14	1.26	0.00	-0.76	-0.08	0.70	0.08
15	-0.40	0.00	0.10	0.12	-0.40	-0.08
16	-3.18	-0.02	0.28	-0.14	0.74	-0.14
17	-0.04	0.00	0.40	0.06	-0.36	-0.02
18	1.42	0.00	-0.76	0.08	0.32	0.14
19	-3.14	0.00	-0.10	0.10	0.28	-0.24

to each set of fringes for subsequent theoretical images, in essence calibrating the fringes for visibility loss induced by the uneven pupil illumination.

3.1.5 Procedure and calibration

As with any experimental setup, calibration steps were required to maximise and fully characterise the expected performance of the experiment. Images were dark subtracted and combined from 100 short exposure images to ensure high signal-to-noise out to and beyond the first Airy ring.

Since FICSM cophases segments in groups, at any given step, unwanted segments were "stowed" by tilting them away from the primary PSF into a widely spaced ring. The limited actuation of the MEMS meant that this ring was still within the field of view of the camera. To prevent this source of stray light from biasing the results, frames were taken with the light source on and all segments in their stowed positions. While this subtraction method was not perfect (due to the fact that during phasing not all segments are stowed), it proved more than adequate in removing the majority of the unwanted bias.

To determine the expected accuracy of the phasing method, several calibration datasets were taken and analysed, separately for piston and tip/tilt. The uncertainty caused by residual instability in the imaging system was estimated by analysing a sequence of images taken without moving any MEMS segments and computing their RMS scatter. This produced values of 0.006 μm for piston and 0.02 milliradians (mrad) for tip/tilt, and was taken as an estimate of the uncertainty limit due

to the stability of the setup.

One MEMS segment was then moved between two fixed positions several times to investigate the reproducibility of segment movements. This test showed that movement of the MEMS did not introduce any extra piston or tip/tilt to the moving segment beyond that expected due to stability with time. However, tilting one segment appeared to cause all other segments to move by a small amount. The RMS scatter of this motion was approximately 0.10 mrad, and appeared independent of the amount of applied tilt.

The movement resolution limits of the control software were 0.02 μm in piston and 0.02 mrad for tip/tilt. Combining these sources of uncertainty sets an upper limit for the obtainable accuracy as 0.02 μm in piston and 0.10 mrad in tip/tilt.

To test FICSM, random tilts and pistons were taken from a uniform distribution with limits of $\pm$ 4 μm for piston and $\pm$ 0.80 mrad for tip/tilt. The piston values were chosen to be safely within the maximum possible range of motion of the MEMS segments, while the tilts were at a level where light from individual segments could easily be identified by eye but still provided some overlap. These values, along with the final results, are given in Table 3.1. The maximum possible piston between any two segments was then 8 μm, approximately 1 coherence length.

Due to the fact that only relative pistons are measurable, a zero point must be chosen. In order to ensure the pistons stayed within the range of motion of the MEMS, segment 2 was set to zero piston in the MEMS control software and the other segments measured relative to it. Tip/tilt, however, is defined relative to the centre of the image and so each image was centred on the same pixel to ensure a common phase centre.

During these tests, it was discovered that the measured pistons were as large as 1.6 μm when the segments were set to their nominal zero positions, and varied substantially from segment to segment. This is likely due to a combination of poor calibration of the preset MEMS "zero" position and wavefront errors from the various optical elements that formed the setup (collimator, mirrors and lens). This was expected, as the MEMS "zero" position is a manufacturer predefined configuration that is not a true reflection of a flat mirror. The final image is then a better indicator of image quality than the actual segment pistons and tip/tilts in the MEMS control software.

To ensure an identifiable target point for our phasing strategy, images with the segments set to zero were first analysed. The piston values measured in each filter were then subtracted from all future piston measurements. This ensured that the goal was to move the segments back to their manufacturer "zero" positions rather than to a new configuration (despite the fact that this may optimise the PSF). Indeed this is one of the strengths of FICSM; by directly measuring the wavefront it can be used to phase segments to an arbitrary, not-necessarily-cophased configuration.

These measured static pistons were later removed and a final image taken to demonstrate the accuracy of the measurements.

The sequence for phasing was modified slightly from the algorithm described earlier (Cheetham et al., 2012) since the negligible laser bandwidth used in the tip/tilt step made the need to repeat the entire procedure (as previously specified) unnecessary. Instead the tip/tilts were measured and removed once, while the pistons were measured and removed twice, with subsequent images taken to verify the setup. The modified sequence is as follows:

1. Take an image using the laser, measure tip/tilt.

2. Remove measured tip/tilt from the segments.

3. Repeat step 1 to verify the segment tip/tilts.

4. Take an image with each of the red and green broadband filters, measure piston.

5. Remove measured piston from the segments.

6. Repeat steps 4 and 5 once, followed by step 4 a third time to record the final segment positions.

3.1.6 Results

The initial and final positions of each segment are shown in Table 3.1. Any overall tip/tilt (due to the centring of the initial image) was removed. The pistons were reduced from a maximum of 3.90 μm to a maximum of 0.04 μm, while the tilts were reduced from a maximum of 0.78 mrad to a RMS scatter of 0.12 mrad.

Images taken using the configurations of each segment before and after phasing are shown in Fig. 3.3. The "after" image was taken with the mirror in its final configuration after phasing with the static wavefront error removed. For reference, a simulated image with a perfectly phased mirror and in the absence of noise is shown.

Upon examination of the phased images, it was apparent that the nominal segment "zero" positions produce a visually worse image than the FICSM phased solution. This is consistent with the observation of large measured static pistons for this "zero" setting.

The encircled energy as a function of radius from the peak was also computed to numerically compare the final image to the expected noise limit, and is shown in Fig. 3.4. Clearly, applying FICSM improves image quality substantially, and the encircled energy curve appears consistent with the noise limit. This corresponds to a RMS wavefront error of about 25 nm. This result suggests a Strehl ratio of 94% using the Maréchal approximation $S = e^{-(2\pi\sigma/\lambda)^2}$, where λ is the observing wavelength and σ is the RMS wavefront error.

This technique proved most sensitive to high Strehl ratio images, so an estimate of the initial Strehl ratio was given by multiplying the final Strehl ratio by the ratio of the peak fluxes of "before" and "after" images taken with the same exposure time. This yielded a value of 9%.

From these results it is clear FICSM has phased the mirror from a degraded state with large pistons beyond the longest filter coherence length and tilts at a level where individual segments could be identified by eye, to within the limits imposed by the segment control system.

3.1.7 Conclusion

Here we have experimentally demonstrated the Fizeau Interferometric Cophasing of Segmented Mirrors algorithm. 18 segments of a MEMS segmented mirror array were phased from a configuration with random initial piston steps of up to 8 μm and tilts of up to 0.80 mrad. The test was performed in the optical band (rather than the infrared) to maximise the aberrations produced by the limited-stroke mirrors. To phase the entire mirror, a segment-tilting approach was utilised. Suggested segment groupings were provided that allow an 18 segment mirror to be phased in 3

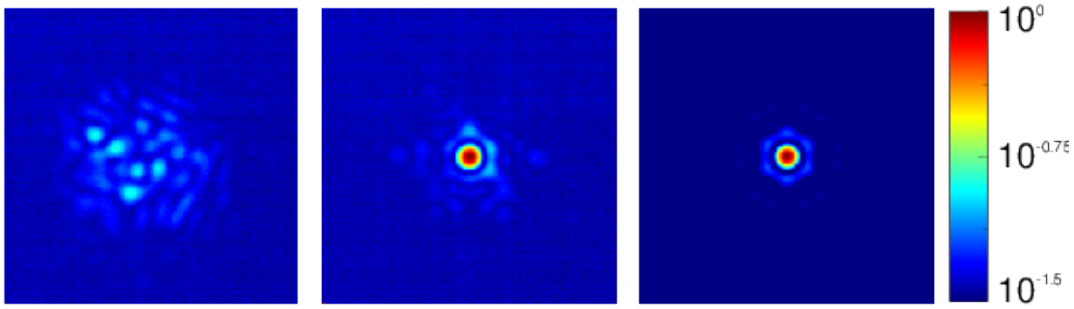

Figure 3.3: Images showing the PSF before (left) and after (middle) phasing, with a log stretch. A simulated perfectly phased image (right) is also shown for comparison. Before phasing, power is spread over a large area. After applying FICSM, the PSF conforms well to the theoretical PSF in the absence of aberrations.

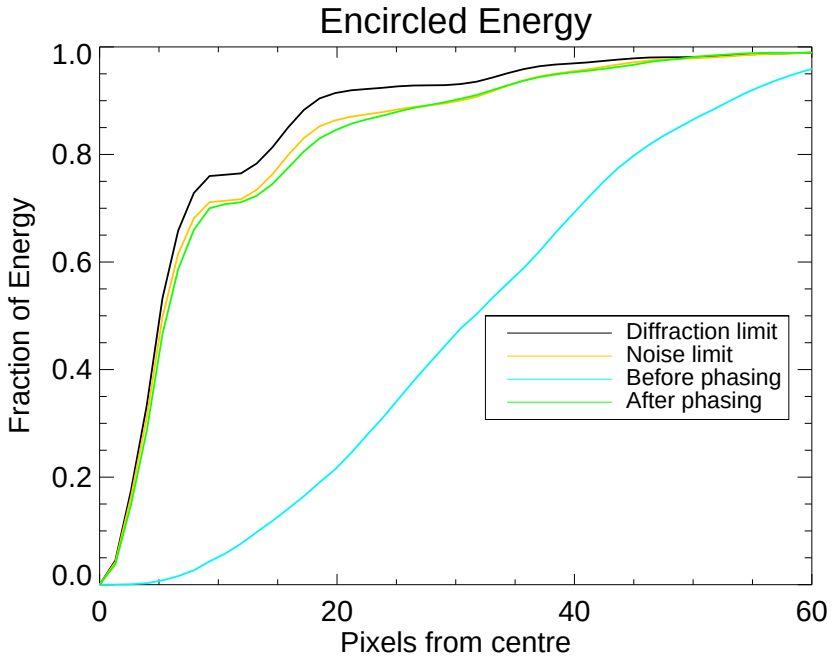

Figure 3.4: The encircled energy as a function of radius of several real and numerical images. The black curve shows the result for a numerically generated image in the absence of noise and free of wavefront error. A typical example of a theoretically generated image with pistons and tilts consistent with the noise limit of the segments is shown in yellow. The blue and green curves show the results for real images taken before and after phasing. These results suggest that FICSM has successfully phased the mirror from an extremely degraded state to a level consistent with the expected noise.

steps, assuming multiple simultaneous pointings on the detector are possible. Analysis of several sources of uncertainty produced an estimation of the final accuracy of 0.10 mrad in tip/tilt and 0.02 μm in piston. After a single application of FICSM to measure and remove tip/tilt and two applications to measure and remove piston, significant improvement in the PSF of the setup was apparent. Comparing encircled energy diagrams for real and numerically generated images implied that the final setup is consistent with this limit, suggesting a final RMS wavefront error of 25 nm, or a Strehl ratio of 94%, from an initial Strehl ratio of 9%. This shows that FICSM has phased the mirror from its extremely degraded initial state to within the limit of accuracy imposed by the setup, using only a science camera, three filters and the actuated mirror itself.

3.2 FICSM on the JWST Testbed

To ensure that the FICSM algorithm is ready for use on JWST if required, there are several criteria that need to be fulfilled. In order to progress to the next Technical Readiness Level, a complete demonstration of the capture range and accuracy on a JWST-like setup is necessary. A perfect candidate for such a test is the JWST Testbed Telescope (TBT) situated at Ball Aerospace (Kingsbury and Atcheson, 2004), which served as the development and testing hub for other JWST phasing algorithms. This setup has a much larger range of motion than the lab setup used to perform previous FICSM experiments, and is a 1/6th scale model of much of the JWST optical train. In November 2013, we were allocated several days to test FICSM on this setup.

Due to problems with foreign nationals accessing national facilities hosting US military technology, the data collection and setup work was carried out by US PhD student Alexandra Greenbaum with help from D. Scott Acton from Ball Aerospace. The data analysis was shared between myself and Alexandra, while the experiment was coordinated by Anand Sivaramakrishnan and myself. Anand invited me to Baltimore to provide the intellectual leadership for these tests, since I had devised and tested its methods and software. All changes to the algorithm required by the differences between setups for the previous FICSM experiments and that of the TBT were implemented by myself.

Ultimately, significant issues were encountered with the TBT setup that prevented the successful testing of FICSM. However, the robustness of the algorithm was significantly improved in response to these problems, and further testing is planned following repairs to be carried out on the TBT.

3.2.1 Setup

Many specifics for the TBT setup are proprietary or ITAR restricted, and so a broad overview is presented here. In essence the basis of the setup is similar to that used in Sydney. An 18 element hexagonal segmented mirror was illuminated by a broadband light source and focussed onto an infrared camera. However, rather than using a lens to focus the light, the TBT segments themselves are curved in a similar way to the JWST primary. A curved secondary mirror also contributes to this task.

The TBT is a double-pass optical system, where light is injected from a bench below the primary mirror, reflected off a tertiary mirror onto the suspended convex secondary mirror and onto the parabolic primary mirror. From there, the collimated light is reflected off a flat mirror suspended above the secondary before returning back through the optical train onto the bench, where it is sent onto the camera. A schematic is shown in Figure 3.5.

The TBT primary mirror segments can be moved to an accuracy of 5 nm in piston and 1.4 mas in tilt, with a range of motion of 500 μm in piston and 25 arcmin in tilt (Kingsbury and Atcheson, 2004). These specifications exceed the requirements to test the capture range of FICSM at visible or near infrared wavelengths.

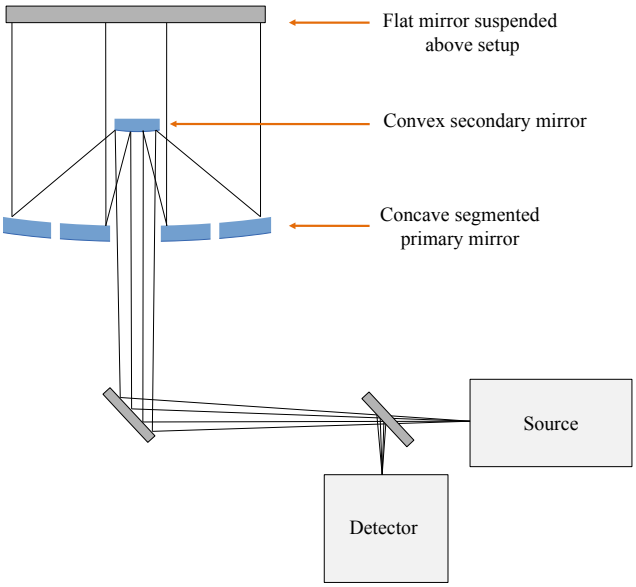

Figure 3.5: A schematic diagram of the TBT optical train. From the light source on the optical bench, light passes onto a convex secondary mirror and onto a curved segmented primary mirror. The resulting collimated light is reflected off a flat mirror suspended above the primary mirror and returns along the same optical path. Finally, a beamsplitter placed in front of the light source separates the return beam from the outbound beam and focusses it onto a detector. Fold mirrors have been omitted for clarity.

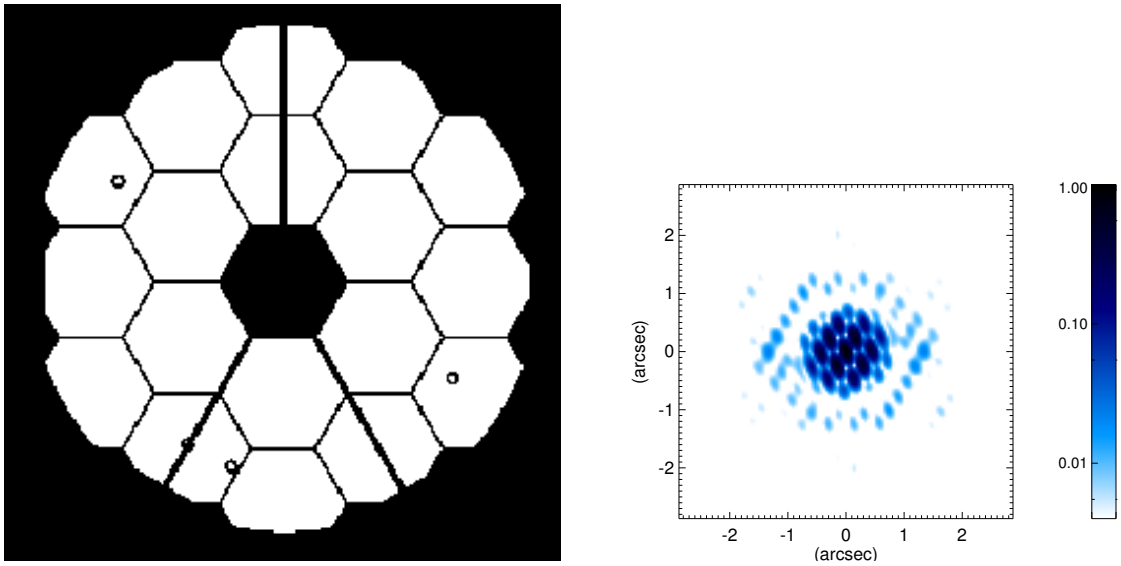

Figure 3.6: *Left*: A diagram of the TBT pupil. The outer ring of hexagonal segments is significantly clipped by the round outer edge of the pupil. The spiders that support the secondary mirror are also clearly visible, and cross several of the mirror segments. Several circular non-reflective regions are also present in the pupil.
Right: The resulting PSF after incorporating the TBT pupil shape.

3.2.2 Issues Encountered and Improvements to FICSM

The TBT pupil has a known problem with clipping that affects the outer ring of segments. In addition to the JWST-like spiders that cross the primary mirror, this changes the shape of many of the segments so that they are not hexagonal. A sketch of the Ball pupil is shown in Figure 3.6. In order to allow FICSM to incorporate this pupil shape, significant changes had to be made to the existing routines. While JWST will not suffer from the same clipping issues, these changes were necessary to include in order to model the TBT, and some are also applicable to JWST itself such as the spiders that support the secondary mirror.

While previously the Fourier transform of each segment was calculated analytically at the time of image generation, for the TBT the complex electric field resulting from each segment was calculated in advance using the known shape of each. This complex electric field was combined with the phase distribution resulting from the piston and tip/tilt on each segment to generate images for use in the fitting algorithms. This seemingly small change to the algorithm results in FICSM being capable of phasing mirror segments of arbitrary shapes, generalizing its application far beyond its original incarnation as a phasing method for JWST.

The PSF resulting from including the TBT pupil shape is also shown in Figure 3.6 for an example segment group. Despite the addition of the spiders and the clipping issues, the PSF shape is superficially similar to that seen in the Sydney setup.

The segment figure errors present on the TBT segments were also significantly above those

previously tested or simulated. For JWST, the measured segment figure errors of 13.5 nm rms equate to 0.3% of a wavelength, while the corresponding figure for the Sydney testbed was 6-20 nm, approximately 3% of a wavelength. The TBT segments instead contained 1.5 μm of peak-to-peak wavefront error with an rms of 110 nm. At a mean wavelength of 1.6 μm, this corresponds to 7% of a wavelength.

The known wavefront errors were incorporated into the pre-calculated Fourier transforms of each segment, so that additional wavefront errors arising from imperfect alignment between segments would be measured on top of the known aberrations. To minimize the effects of the segment figure errors, the 3 least affected segments were chosen to test the algorithm. Two simulated PSFs resulting from incorporating the known wavefront error are shown in Figure 3.7.

Due to the unavailability of broad IR filters for the experiment, it was necessary to combine two narrow bandwidth filters. This was accomplished by taking images with an identical setup with both filters, then adding the two images together before processing. Preliminary simulations showed that this approach was viable and would not affect the overall accuracy of FICSM. The filters used consisted of 1550 nm and 1640 nm with a FWHM bandwidth of $\sim$20 nm each.

However, it was determined via inspection of the Fourier transform of images taken with the 1640 nm filter that an extra spectral feature at longer wavelengths was present. Further testing of the filter revealed a second transmission peak located at approximately 1950 nm and with a peak throughput more than 10% of the 1640 nm peak. This second peak had insufficient flux for the 1640 nm filter to be used as a broad bandwidth filter for FICSM on its own, and combination with the 1550 nm filter was still required.

Unfortunately, the large wavelength difference between the 1550 nm filter and the 1950 nm spectral feature resulted in overlap between the spatial frequencies of the most widely separated pair of holes at 1550 nm and the closest pair of holes at 1950 nm. This breaks the strict non-redundancy criteria that forms the foundation of FICSM.

In addition to the problems described above, the TBT segments had suffered a failure of their radius of curvature actuators prior to beginning the experiment. A schematic diagram of the functionally identical JWST segment actuators is shown in Figure 3.8. Each mirror segment for both JWST and the TBT has 7 actuators to control its position and shape. 6 actuators are mounted towards the edge of each segment to allow movement in piston, tip/tilt and segment clocking. These are rigid body movements that control the position of the segment but do not affect its shape. The final actuator controls the radius of curvature of the segment by pushing and pulling on its centre. The failure of the radius of curvature actuators on each segment meant that each segment had an unknown amount of wavefront error in focus.

While the magnitude of the focus error due to the loss of the radius of curvature actuators is unknown, analysis of images suggested that it was substantially more than a wavelength. This led to an extremely degraded PSF that was unable to be used for the purposes of testing FICSM. An image resulting from the mirror in its nominal phased position is shown in Figure 3.7, with the expected image based on known aberrations shown for comparison.

3.2.3 Discussion

Due to the myriad of difficulties encountered, FICSM could not be successfully tested with the JWST TBT. However, substantial improvements were made to the previously used methods that

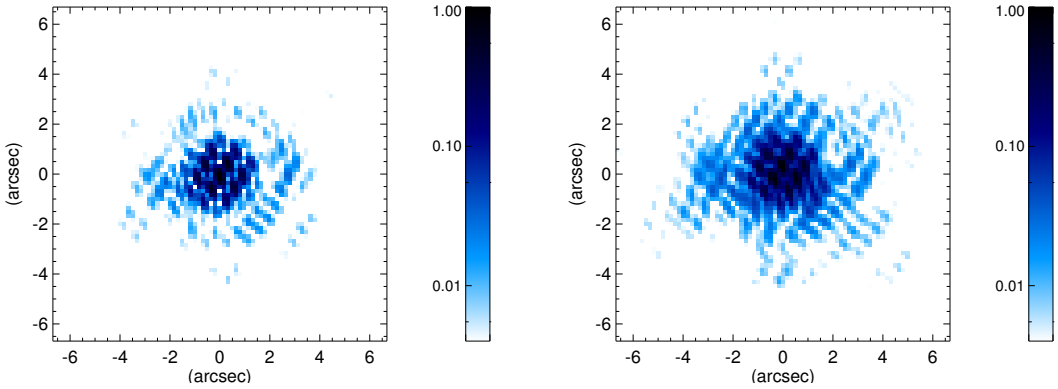

Figure 3.7: *Left*: The resulting PSF after incorporating the TBT pupil shape and known segment figure errors, shown at 1550 nm.
Right: An image taken at 1550nm with the TBT setup. The large differences between these images shows that the focus error introduced by the radius of curvature of each segment is much larger than the impact of the segment figure errors. The light is spread over a much larger area, the peaks and nulls of the fringes are less defined and the first Airy ring is indistinguishable from the central peak.

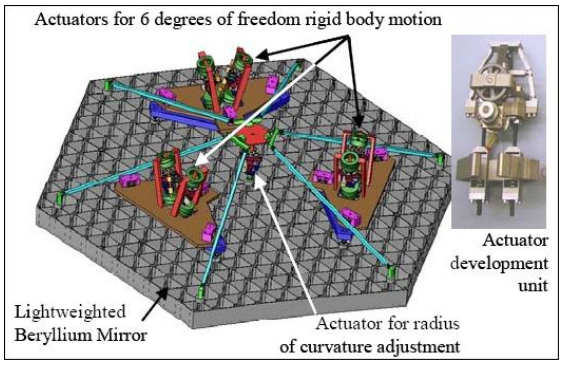

Figure 3.8: A schematic diagram of the actuators mounted onto a JWST segment. This setup is functionally equivalent to that of the TBT mirror segments.

allow FICSM to deal with aberrated segments, static wavefront error introduced by the optical system and arbitrary pupil shapes. In particular, incorporating a method for dealing with arbitrary pupil shapes into the FICSM algorithm is an extremely important requirement for the successful development of the technique. Telescope spiders are ubiquitous in modern on-axis telescopes, including JWST, and it is important that potential cophasing techniques are robust to their presence. In addition, two of the next generation of ground based ELTs contain many hundreds of segments (TMT Nelson and Sanders 2008; E-ELT Gilmozzi and Spyromilio 2007). These segments require regular maintenance, and so at any time many will be missing from the primary mirror. For the E-ELT, the number of spares will not be sufficient to replace missing segments, leading to a telescope primary mirror shape that varies night to night, and so cophasing methods to be employed on this telescope must be able to cope with such scenarios.

3.3 Future Work

To date, FICSM has been tested extensively through numerical simulations and shown to be robust to many of the types of noise that are expected to be present on a space telescope. Substantial testing has also been conducted on a lab testbed that demonstrated its success in a real-world optics laboratory environment. This is an important stepping stone in the development of the algorithm from a technical readiness standpoint.

The next stages of progression for the purposes of JWST cophasing involve rigorous testing in situations closer to those expected aboard the spacecraft. Two crucial milestones on this path require testing on simulation-level hardware and testing in a space-like environment.

Testing FICSM on JWST-grade hardware can be accomplished through use of the Ball TBT. Following the unsuccessful attempt reported above, the radius of curvature actuators have been repaired and a test is now possible. Using the lessons learnt (including careful planning of filters), this would be an ideal environment to test the algorithm in a more rigorous fashion.

A demonstration of FICSM in a space-like environment looks to be a more difficult challenge. One candidate for achieving such a milestone would involve the use of a sounding rocket. Sounding rockets offer a 5-20 minute window in which to conduct an experiment in a space-like environment. A similar testbed to that used to demonstrate FICSM in Cheetham et al. (2014) could be loaded onto such a rocket and used to conduct an experiment during this time.

In addition to progression towards readiness for JWST, FICSM has potential applications on ground based telescopes. However, the marked differences between ground and space based environments introduces significant problems for many phasing algorithms, FICSM included. As a technique reliant upon the measurement of Fourier phases, the turbulent effect of the atmosphere add a large, rapidly varying component to this measurement that must be accounted for.

In order to reduce the effects of seeing on the performance of FICSM, images can be taken quickly to freeze the atmosphere during an image. By taking a large number of measurements, the atmospheric component of the measured piston will average to zero, while the contribution from the misaligned mirrors will remain. Operating at a long wavelength, where the effect from the atmosphere is lessened, would also help with this task.

Another problem for FICSM on a ground based telescope is that the tip/tilt component of atmospheric-induced wavefront error would be apparent in all images. This would bias the mea-

surement of piston and cause the algorithm to fail, since measurement of piston requires the tip/tilt contribution to the overall wavefront error to be negligible. This can be achieved through the use of smaller subapertures (scaled with r_0), which will ensure that the dominant wavefront error across any subaperture will be that due to piston. However, it also prevents the measurement of tip/tilt across any subaperture, a fact that can be remedied by the placement of multiple mask holes on each segment. 3 such mask holes per mirror segment would be sufficient to measure both the piston and tip/tilt of each segment.

To employ FICSM on a ground based telescope with a large number of segments (such as the E-ELT or TMT), the technique will need to be scaled from tens to hundreds of segments. The number of segment grouping required to completely phase a mirror may change substantially as the number of segments increases, and is an important consideration in determining whether FICSM is a practical phasing technique on these telescopes. Preliminarary work suggests that FICSM can be applied on a 36-segment layout similar to Keck with at most 7 groupings (the same number as for the 18-segment JWST), however this number may increase on much larger telescopes, increasing the time taken to apply the technique.

The extent to which FICSM is affected by segment aberrations and higher order wavefront errors has yet to be fully investigated. Simulations involving the known JWST segment figure error maps are an important step in preparing FICSM for application on that telescope, and should give an indication as to the expected effects of the larger aberrations present on ground based telescopes.

One promising application for FICSM is its combination with an upstream adaptive optics system. Through the use of a non-redundant aperture mask, the local piston and tip/tilt behind each mask hole can be measured for both segmented and monolithic mirrors, acting as a check on residual non-common path errors. An estimate of low order aberrations such as focus or spherical aberration can be given through this approach. The reduction of time varying wavefront errors provided by an adaptive optics system could also allow FICSM to be applied to ground based telescopes with little modification from the space based approach investigated in this thesis.

Chapter 4

Binary Searches

4.1 Adaptive Optics Imaging of Brown Dwarf Binaries

In the following section, I present the results of a survey targeting brown dwarf binary systems. The observations were obtained in service mode by staff at the VLT, based on a proposal written by myself, Benjamin Pope and Peter Tuthill. The observing strategy was developed primarily by myself, with input from Benjamin and Peter. The data analysis was performed by myself, using a pipeline I developed for this purpose.

4.1.1 Motivation and Observations

While investigations into star formation have supported an extensive literature stretching back for decades, comparatively little is known about the formation mechanisms and evolution of brown dwarfs. Their masses are more than an order of magnitude below the typical Jeans mass in star-forming regions, and the unexpected lack of brown dwarf companions in close orbits to field stars (the "brown dwarf desert" Marcy and Butler, 2000; Grether and Lineweaver, 2006) suggests profoundly different pathways, rather than scalings of known physics. Furthermore, brown dwarf evolutionary tracks rely heavily on models and are constrained by very few direct mass measurements.

To date the most extensive imaging survey of brown dwarfs was undertaken by Reid et al. using Hubble Space Telescope (HST) data (Reid et al., 2006, 2008). By studying the multiplicity of L dwarfs within 20 pc, they revealed the presence of 10 binary systems. A recent reanalysis of this data using the processing technique of Kernel Phase Interferometry (Martinache, 2010) revealed a more complete census of companions in this sample, raising the number of detected binary systems to 15, with a further 4 objects detected at marginal significance (Pope et al., 2013).

In order to rectify the lack of observations with which to test evolutionary models, we are performing an orbital monitoring survey of these brown dwarf binary systems. By tracking these objects over many years, we can calculate their orbital parameters and obtain model independent dynamical masses. This fundamental quantity is important for constraining down brown dwarf evolutionary models, and the Pope et al. (2013) sample presents an ideal opportunity to add to the handful of robust mass estimates for brown dwarfs that currently exist. The list of targets is shown in Table 4.1.

Observing these faint objects at the angular resolution necessary to resolve the binary compo-

Table 4.1: Brown Dwarf Binary Target List based on Pope et al. (2013), with the separation (ρ) and contrast ratio (C) of the detected companions.

Name	2MASS Number	RA	Dec	ρ (mas)	C	J (mag)	K (mag)
J0004	J00043484-4044058	00 04 34.84	-40 44 05.8	84	1.04	13.1	11.4
J0025	J00250365+4759191	00 25 03.65	+47 59 19.1	329	1.32	14.8	12.9
J0036	J00361617+1821104	00 36 16.17	+18 21 10.4	44	1.85	12.5	11.1
J0045	J00452143+1634446	00 45 21.43	+16 34 44.6	50	1.11	13.1	11.4
J0109	J01092170+2949255	01 09 21.70	+29 49 25.5	49	40	12.9	11.7
J0147	J01473282-4954478	01 47 32.82	-49 54 48.0	139	2.37	13.1	11.9
J0314	J03140344+1603056	03 14 03.44	+16 03 05.6	124	70	12.5	11.2
J0429	J04291842-3123568	04 29 18.42	-31 23 56.8	525	3.51	10.9	9.8
J0700	J07003664+3157266	07 00 36.62	+31 57 26.3	179	4.52	12.9	11.3
J0830	J08300825+4828482	08 30 08.25	+48 28 48.2	48	29	15.4	13.8
J0915	J09153413+0422045	09 15 34.15	+04 22 04.7	738	1.11	14.5	13.0
J1539	J15394189-0520428	15 39 41.89	-05 20 42.8	35	4	13.9	12.6
J1707	J17072343-0558249	17 07 23.44	-05 58 24.9	1010	10	12.1	10.7
J1936	J19360187-5502322	19 36 02.63	-55 02 36.7	67	18	15.4	15.0
J2028	J20282035+0052265	20 28 20.35	+00 52 26.5	46	1.52	14.3	12.8
J2152	J21522609+0937575	21 52 26.09	+09 37 57.5	254	1.09	15.2	13.3
J2252	J22521073-1730134	22 52 10.73	-17 30 13.4	126	2.46	14.3	12.9
J2255	J22551861-5713056	22 55 18.61	-57 13 05.6	179	5.05	14.1	12.6
J2351	J23515044-2537367	23 51 50.44	-25 37 36.7	63	2.4	12.5	11.3

nents is difficult with existing instruments. Brown dwarf spectra peak at infrared wavelengths and have extremely low luminosities, leaving very little light for an adaptive optics system operating in the visible band. As nearby field objects, these targets cannot be observed with laser guide star adaptive optics due to the lack of nearby tip/tilt stars. In order to observe these systems, either space based observations or ground based observations with an infrared wavefront sensor are required. For this reason, our orbital monitoring survey utilises the NAOS-CONICA instrument on the VLT, which has an infrared wavefront sensor suitable for this purpose.

4.1.2 Observations and Data Analysis

Detailed analysis of the detectability of each possible target was performed, taking into account the faintness of the system as well as the separations and contrasts between the components. A successful observing proposal was submitted for the 2013A semester (Period 90), involving observations in two infrared bands (H and K_s) so that instrumental effects on the PSFs (which scale with wavelength) could be separated from real structure. The observations were obtained in July-August 2013, and are summarized in Table 4.2. In total, data were obtained for 10 targets: J0004, J0036, J0045, J0109, J0147, J0429, J2029, J2252, J2255 and J2351.

The raw images were first cleaned by flat fielding and background subtracting. Cosmic rays

Table 4.2: Log of observations

Date	Filter	Targets	Conditions
2013-07-02	H, K_s	J0004	Bad seeing
2013-07-18	H, K_s	J2028	Cloudy
2013-07-23	H, K_s	J0036	Bad seeing
2013-07-30	H, K_s	J2252	Good
2013-08-02	H, K_s	J0045, J0036	Good
2013-08-03	H, K_s	J2028, J2351	Good
2013-08-05	H, K_s	J2028, J0004, J0147, J2255	Cloudy
2013-08-11	H, K_s	J0004, J0147	Bad seeing
2013-08-15	H, K_s	J2028, J2255	Great
2013-08-17	H, K_s	J2351	Great
2013-08-23	H, K_s	J0004	Great
2013-08-28	H, K_s	J0004, J0036, J0109	Good, but deteriorated
2013-08-30	H, K_s	J0004, J0036, J0109	Good, but deteriorated
2013-08-31	H, K_s	J0109, J0429	Good

and bad pixels were then removed from the images, and replaced by the local median. Images were then centred and rotated to remove sky rotation using an FFT based algorithm (Cox and Tong, 1999). To analyse the cleaned data, a custom PSF fitting pipeline was written to fit a binary model to the images.

The level of AO correction varied substantially based on the brightness of the target and the conditions during the observations. This led to marked differences in PSF shape between targets and between nights. Visually, it was apparent that residual wavefront errors were large enough to prevent the formation of a recognisable ideal diffraction pattern (Airy disk). In order to best match the observed data, a multi-parameter prescription for the PSF $I(x, y)$ was adopted, based on a Gaussian-like function of the following form:

$$I(x,y) = Ae^{-(w_x[(x-x_0)\cos\phi+(y-y_0)\sin\phi]+w_y[(y-y_0)\cos\phi-(x-x_0)\sin\phi])^\gamma}, \tag{4.1a}$$

where A is a flux scaling parameter, w_x and w_y control the widths in two orthogonal directions, ϕ allows a rotation of w_x and w_y with respect to the x and y axes, (x_0, y_0) are the coordinates of the PSF centre and γ is a smoothness parameter that controls how steeply the PSF drops off. This description of the PSF provided an adequate fit to the data and was chosen more on heuristic principles than any theoretical expectation for the PSF to closely match this form. Since the purpose of the PSF fitting was to calculate the binary parameters, an exact PSF match was not required.

Each fit consisted of 10 parameters: the 7 PSF shape parameters described above ($x_0, y_0, A, w_x, w_y, \phi, \gamma$) as well as the binary separation ρ, position angle θ and contrast ratio C.

Due to the significant differences in PSF shape between frames, a bootstrapping approach was taken to estimate parameter uncertainties (Efron, 1979). In order to obtain reasonable starting parameters, the nested sampling implementation MULTINEST was first applied to the regular

stacked image. MULTINEST is a PYTHON implementation of the importance nested sampling algorithm (Feroz et al., 2009; Feroz and Hobson, 2008; Feroz et al., 2013). 200 stacked images were then generated from the set of data frames by resampling and stacking the frames with replacement. The best fit nested sampling parameters were then used as a starting point for nonlinear least squares fits to each of the resampled stacked images using the modified Levenberg-Marquadt module LEASTSQ from Python's SCIPY package. The mean and standard deviation of the resulting parameters were then taken as the value and uncertainty of each.

4.1.3 Results

The brown dwarfs with recovered companions are listed in Table 4.3. Our observations allow the detection of 6 companions, including 4 of the 5 binaries reported in Reid et al. (2006, 2008) that were observed and 2 of the 4 binaries reported in the Pope et al. reanalysis (Pope et al., 2013). The sole marginally detected binary from Pope et al. (2013) that was reobserved did not result in a detection. Each of the detected companions was obvious from both the raw data and the stacked frames.

Of the 5 observed targets for which a secondary component was not resolved, only the J2252 secondary would have been detectable in our data at the same separation and contrast as its HST detection epoch. Given the large amount of orbital motion expected since the HST observations, it may have moved to a smaller separation. The lack of a detected secondary component for these 5 targets therefore should not be taken as evidence of the non-existence of a co-moving companion.

Significant orbital motion was observed for all detected companions. The observed changes in relative position are not consistent with those expected from a background star, suggesting that the detected objects are bound companions. The binaries J2351 and J2028 that were both observed with small angular separations in the HST data have had motion primarily in the radial direction, substantially increasing their angular separation between epochs and making them easily detectable in our data.

The companion detections made for J2028 and J2351 are an important milestone in interferometric techniques for high angular resolution astronomy. They represent the first independent confirmation of a companion originally detected through the use of kernel phase interferometry.

Both J0004 and J0147 exhibit substantial disagreement between their calculated positions in each band. Due to the poor AO correction during observations of these objects, the secondary components were not completely resolved. It is likely that the uncertainties on the separation and contrast ratio were underestimated due to the degeneracy between these parameters at small separations that allows a closer and brighter companion to be confused for a more distant and fainter one.

Additionally, the calculated contrast ratio of J0004 both at the HST epoch and here are consistent with unity. Due to difficulties establishing which component is brighter, the secondary component may have been wrongly identified, leading to a 180°ambiguity in the position angle for this system.

Table 4.3: Results of PSF Fitting to Data

Star	Band	ρ (mas)	$\Delta\rho$	θ (°)	$\Delta\theta$ (°)	C	ΔC
J0004	H	93.8	1.8	96.3	0.7	1.06	0.07
J0004	Ks	82.8	0.4	94.7	0.4	1.018	0.011
J0147	H	91	2	232	2	1.82	0.12
J0147	Ks	98.9	0.5	230.8	0.5	2.21	0.04
J0429	H	504.1	1.6	232.8	0.2	2.73	0.02
J0429	Ks	502.2	0.5	232.86	0.07	2.517	0.015
J2028	H	53	4	114	3	2.5	0.9
J2028	Ks	49	3	124	3	1.3	0.2
J2255	H	147.5	1.5	21.2	0.5	3.76	0.12
J2255	Ks	150.3	1.7	23.4	0.4	3.29	0.07
J2351	H	260.7	0.8	39.6	0.27	2.37	0.03
J2351	Ks	261.5	0.5	40	0.1	2.05	0.02

4.1.4 Next Steps

Preliminary estimates for the orbital periods of these objects suggests that significant orbital motion should be observable for most targets with a time baseline of just a few years. Subsequent observations with NACO are planned for the near future.

A complete orbital solution consists of 7 parameters: period (P), time of periastron (T_0), semi-major axis (a), eccentricity (e), orbital inclination (i), and two angles (ω) and (Ω) that define the orientation of the orbit in the sky. To get an estimate for each of these parameters, at least 3 measurements consisting of the 3 measurable variables (ρ, θ and time T) are required. After sufficient observations of each target have been obtained, an orbit will be derived.

The total mass of each system can be directly calculated using Kepler's third law by combining the period and semi-major axis of each orbit with the measured parallax. The combination of measured parameters and luminosities for these systems will then allow important constraints to be placed on brown dwarf formation and evolutionary models.

4.2 Brown Dwarf Companions to Intermediate Mass Stars

The most stringent tests of brown dwarf formation models come from combining information on the masses, ages and luminosities of such systems. However, calculation of these quantities is not straightfoward for brown dwarfs in the field. As discussed in the previous section, calculation of the masses and luminosities of brown dwarfs can be accomplished for brown dwarfs in binary systems through measurement of their orbital parameters and parallax. However, measuring the age of such systems in a model-independent way is difficult.

One simple way to avoid problems with estimating brown dwarf ages is to tie them to another, better calibrated measurement. This can be accomplished for brown dwarfs in nearby associations or moving groups when the age of the group can used as an estimate. An alternative method involves measuring these quantities for brown dwarfs in binary systems involving stellar mass primaries. In this case, well calibrated stellar evolutionary models can be used to calculate the age of the primary star, which can be used as a robust estimate for the brown dwarf component.

In the following paper published in the Astrophysical Journal in June 2015, we report the discovery of a group of brown dwarf and low mass stellar companions to intermediate mass stars in the nearby Scorpius-Centaurus star forming region. My contribution to this work involved 50% of the processing and analysis of the data, resulting in the detection and observed parameters (ρ, θ, C) for 4 brown dwarf companions to 3 targets. The observations and remaining data analysis were performed by the coauthors.

The following manuscript was published in the Astrophysical Journal Letters (2015) vol. 806, issue 1, L6.

Discovery of Seven Companions to Intermediate Mass Stars with Extreme Mass Ratios in the Scorpius-Centaurus Association

Sasha Hinkley,[1] Adam L. Kraus,[2] Michael J. Ireland,[3] Anthony Cheetham,[4] John M. Carpenter,[5] Peter Tuthill,[4] Sylvestre Lacour,[6] Thomas M. Evans,[1] Xavier Haubois,[7,4]

[1]University of Exeter, Physics Department, Stocker Road, Exeter, EX4 4QL, United Kingdom
[2]Department of Astronomy, The University of Texas at Austin, Austin, TX 78712, USA
[3]Research School of Astronomy & Astrophysics, Australian National University, Canberra ACT 2611, Australia
[4]Sydney Institute for Astronomy, School of Physics, The University of Sydney, NSW 2006, Australia
[5]Department of Astronomy, California Institute of Technology, 1200 E. California Blvd., MC 249-17, Pasadena, CA 91125, USA
[6]LESIA, CNRS/UMR-8109, Observatoire de Paris, UPMC, Université Paris Diderot, 5 place Jules Janssen, 92195 Meudon, France
[7]European Southern Observatory (ESO), Alonso de Cordova 3107, Casilla 19001, Vitacura, Santiago 19, Chile

Abstract

We report the detection of seven low mass companions to intermediate-mass stars (SpT B/A/F; $M\sim$1.5-4.5 $M_{\odot}$) in the Scorpius-Centaurus Association using nonredundant aperture masking interferometry. Our newly detected objects have contrasts $\Delta L'\approx$4–6, corresponding to masses as low as $\sim$20 $M_{\rm J}$ and mass ratios of $q\sim$0.01-0.08, depending on the assumed age of the target stars. With projected separations $\rho\sim$10-30 AU, our aperture masking detections sample an orbital region previously unprobed by conventional adaptive optics imaging of intermediate mass Scorpius-Centaurus stars covering much larger orbital radii ($\sim$30-3000 AU). At such orbital separations, these objects resemble higher mass versions of the directly imaged planetary mass companions to the 10-30 Myr, intermediate-mass stars HR 8799, β Pictoris, and HD 95086. These newly discovered companions span the brown dwarf desert, and their masses and orbital radii provide a new constraint on models of the formation of low-mass stellar and substellar companions to intermediate-mass stars.

4.2.1 Introduction

Observing the population of planetary and brown dwarf companions orbiting young ($\sim$5-10 Myr) stars, soon after the dissipation of the primordial gaseous disk, is a key measure that will lend support to competing formation models of substellar objects (e.g. Delgado-Donate et al., 2004; Stamatellos and Whitworth, 2009). Specifically, direct measurements of the *orbital* distribution of these objects shortly after formation (e.g. Dodson-Robinson et al., 2009; Kratter et al., 2010) will serve as essential constraints to theoretical and numerical models of planetary formation. Thus, observing low mass companions as early as possible (e.g. Kraus et al., 2014) will then serve as a "snapshot" of nascent system architecture, and largely eliminate any confusion about the initial conditions of companion formation caused by subsequent dynamical processes (e.g. Scharf and Menou, 2009; Chatterjee et al., 2008). Moreover, observing the luminosities of substellar companions in the first few million years is essential to constrain models of the intial entropy and temperatures of substellar objects (e.g. Fortney et al., 2008; Marleau and Cumming, 2014).

However, due to the scarcity of young stars in the solar neighborhood, assembling a statistically robust sample of low-mass companions requires observations of large, newly-formed stellar associations. One such region, the Scorpius-Centaurus (hereafter "Sco-Cen") association, with a

Table 4.4: Table of Observations

Target HIP	Region	$P_{\rm mem}$ (%)	SpT	dist (pc)	V (mag)	$W1$ (mag)	A_V (mag)	$M_{\rm bol}$ (mag)	$\log(T_{\rm eff})$ (K)	M ($M_\odot$)	Observatory & UT Date
71724	UCL	94%	B8.5	157^{+16}_{-13}	6.63	6.82±0.05	0.04±0.23	0.03±0.55	4.072±0.087	$3.41^{+0.53}_{-0.75}$	VLT: 2011 June 10
73990	UCL	92%	A9	125^{+15}_{-12}	8.23	7.28±0.03	0.30±0.17	2.48±0.28	3.872±0.022	$1.72^{+0.08}_{-0.11}$	VLT: 2011 June 10
74865	UCL	96%	F4	115^{+19}_{-14}	9.00	7.78±0.03	0.20±0.07	3.50±0.31	3.822±0.006	$1.42^{+0.04}_{-0.06}$	VLT: 2011 June 10
78196	USco	95%	A0	127^{+9}_{-8}	7.03	7.09±0.05	-0.05±0.25	1.36±0.45	3.987±0.076	$2.46^{+0.31}_{-0.59}$	Keck: 2010 May 24
78233	USco	79%	F0	145^{+15}_{-15}	9.17	7.64±0.03	0.84±0.11	2.55±0.25	3.857±0.012	$1.67^{+0.07}_{-0.12}$	Keck: 2010 April 25
79124	USco	93%	A0	123^{+11}_{-9}	7.83	6.96±0.05	0.88±0.25	1.30±0.46	3.987±0.076	$2.48^{+0.32}_{-0.58}$	Keck: 2010 April 05

Table 4.5: "UCL" and "USco" refer to the Upper Centaurus Lupus, and Upper Scorpius regions of Sco-Cen, respectively. Membership probabilies in column three are taken from Rizzuto et al. (2011)

distance of ∼120-150 pc (de Zeeuw et al., 1999) and 5-20 Myr age (e.g. Pecaut et al., 2012; Song et al., 2012) is the nearest OB Association. The young age of this association ensures that any planetary and brown dwarf companions will have elevated luminosity (e.g. Baraffe et al., 2003), allowing access to planetary mass objects even with observations achieving modest relative contrasts.

In addition to selecting young targets, observing stars more massive than solar ("intermediate mass stars", 2-5 $M_{\odot}$) may also enhance the probability of detection of substellar objects. Indeed, some studies suggest the fraction of super-Jupiter companions may be higher for stars more massive than $\sim$2 $M_{\odot}$ (Crepp and Johnson, 2011; Vigan et al., 2012; Rameau et al., 2013; Reffert et al., 2015), possibly due to initially more massive circumstellar disks (e.g. Andrews et al., 2013), or possibly to serve as a reservoir for the conserved initial angular momentum of the star forming cloud (e.g. Kouwenhoven et al., 2007b). The relatively short main-sequence lifetimes of these intermediate mass stars implies young associations such as Sco-Cen should have a greater fraction of these stars compared to the local solar neighborhood, making Sco-Cen a particularly promising region to study young, intermediate mass stars.

To date, the only companions to Sco-Cen *intermediate-mass* stars lie at wide separations (∼30-3200 AU, e.g. Kouwenhoven et al., 2007b; Aller et al., 2013; Janson et al., 2013; Lafrenière et al., 2014; Bailey et al., 2014). The ∼120–150 pc distance to Sco-Cen stars means that orbital separations of substellar companions to these stars located near the ice line (5-10 AU), where planet formation is thought to be most efficient (e.g. Pollack et al., 1996), corresponds to angular separations very close to the near-infrared diffraction limit of 10 m telescopes ($\lambda/D \approx$ 30-45 miliarcsec). Thus, sensitivity near, and within, the diffraction limit of large telescopes is needed to access smaller orbital separations for Sco-Cen stars (Kraus et al., 2008, 2011).

Aperture masking interferometry (e.g. Tuthill et al., 2000; Ireland, 2013, and references therein), provides sensitivity at scales up to, and somewhat within, the usually defined diffraction limit ($\sim\frac{1}{3}\lambda/D - 4\lambda/D \simeq$ 20-300 mas for Keck L'-band imaging). Applications of this technique (e.g., Ireland and Kraus, 2008; Hinkley et al., 2011; Kraus and Ireland, 2012, and references therein) use AO along with an opaque mask containing several holes, constructed such that the baseline between any two holes samples a unique spatial frequency in the pupil plane. Further, no coronagraphic mask is used, which avoids problems associated with measuring the relative astrometry between the occulted host star and a detected companion (e.g. Digby et al., 2006). Despite its very good sensitivity to small inner working angles, aperture masking interferometry usually only achieves typical contrasts of ∼5-8 mag (Kraus et al., 2008; Hinkley et al., 2011). Nonetheless, these modest contrasts are still sensitive to planetary mass companions at young ages (Kraus et al., 2008; Kraus and Ireland, 2012).

This paper presents discoveries of companions with extreme mass ratios, $q = M_{\rm companion}/M_{\rm host} \approx$ 0.01-0.08, from an ongoing multiplicity survey of ∼140 intermediate mass stars (SpT=B0-F2) in the Sco-Cen region using aperture masking interferometry. We have selected our targets based on the refined Bayesian Sco-Cen membership selection technique described in Rizzuto et al. (2011), which uses radial velocity information to confirm or reject candidates. Since high-mass stars frequently host one or more binary companions (e.g. Duchêne and Kraus, 2013) which prevents the required contrast from being achieved, the targets in this study have been screened using past literature to eliminate binary systems with typical separations of >30 mas and masses

$>0.1\,M_{\odot}$. Following this, we used results from our own ongoing snapshot AO imaging programs at Keck, VLT, and Palomar Observatories to eliminate other systems with evidence for binarity. A more comprehensive discussion of our target selection and broad survey results will be given in a subsequent work (Rizzuto et al., *in prep*). In §4.2.2, we describe the host star properties for our discoveries, followed by our observations and analysis strategy (§4.2.3). In §4.2.4 and §4.2.5 we summarize our findings and place them in context.

4.2.2 Target Star Properties

In Table 4.5, we list the basic properties of the targets described in this work. With an ultimate goal of calculating host star mass, we start by calculating the bolometric magnitude ($M_{\rm bol}$) from the V magnitude plus an estimate of the visual extinction A_V and bolometric correction BC_V. We first estimated the visual extinction for each of our targets by comparing the observed $(V-K)$ colors of our target stars with the $(V-K)$ colors for the corresponding spectral types tabulated by Pecaut et al. (2012). As noted in Table 4.5, the spectral types we assume come either from the HD catalog (Houk and Smith-Moore, 1988) or from Pecaut and Mamajek (2013). Our spectral types have uncertainties of ±2 subclass for the spectral types listed in the HD catalog, and ±1 for those listed in Pecaut et al. (2012). We assume that our uncertainties in spectral type result in $(V-K)$ color uncertainties of 0.1-0.2 mag, while the uncertainties in the color versus spectral type relation do not exceed 0.05 mag. Next, using this estimate and the observed $(V-K)$ color, we estimate A_V using the relation between A_V and A_K from Schlegel et al. (1998). Using the spectral types and uncertainties, we adopt BC_V values from Pecaut and Mamajek (2013), where the uncertainty in BC_V is set by the uncertainty in the spectral type. We then combine V mag, A_V, BC_V, and the distance modulus to calculate bolometric absolute magnitudes $M_{\rm bol}$, and its uncertainty. Next, we estimate $T_{\rm eff}$ and its uncertainty using the spectral type (SpT) along with the tabulated values in Pecaut and Mamajek (2013). Lastly, we use the $T_{\rm eff}$ and $M_{\rm bol}$ values calculated above to calculate the mass for each target star by calculating a two-dimensional surface, mass($T_{\rm eff}$, $M_{\rm bol}$), and then marginalizing the probability distribution function of ($T_{\rm eff}$, $M_{\rm bol}$) to obtain 1σ confidence intervals. These masses are listed in Table 4.5.

As Table 4.5 shows, all of the stars considered in this paper are members of either the Upper Centaurus Lupus (hereafter "UCL") or the Upper Scorpius (hereafter "U Sco") subgroups. Rather than assign distances to each star that reflect the average distances of the Sco-Cen subgroups (e.g. 125$\pm$15 pc and 145$\pm$15 pc for UCL and U Sco, respectively), we use the individual Hipparcos parallaxes recorded for these stars, since the individual parallax uncertainties associated with each target are comparable to the subgroup distance uncertainties ($\sim$10%). However, HIP 78233 has a recorded Hipparcos parallax inconsistent with the median U Sco members, with large uncertainty (4.84$\pm$1.37 mas). So we assign to it a distance of 145$\pm$15 pc, the median distance to U Sco.

While we have selected our targets partly based on their high probabilities of Sco-Cen membership as stated in Rizzuto et al. (2011), placement of the host stars on an HR diagram using the values calculated in Table 4.5 verifies all targets can be well fit between the 10 and 20 Myr isochrones from Bressan et al. (2012). These ages are broadly consistent with the reported ages of UCL and U Sco. Some disagreement persists over the age of U Sco, which ranges from 5 Myr (Preibisch and Zinnecker, 1999; Preibisch et al., 2002) to as high as 11 Myr (Pecaut et al., 2012).

Table 4.6: Properties of Newly Detected Companions

Companion	$\Delta L'$ (mag)	Sep (mas)	PA (degrees)	Confidence Level	$M_{L'}$ (mag)	10 Myr Mass (M_J)	20 Myr Mass (M_J)	Sep (AU)	q=$M_{\rm comp}/M_{\rm star}$ (10 Myr, 20 Myr)
HIP71724B	$4.86^{+0.09}_{-0.08}$	103^{+4}_{-5}	202^{+2}_{-2}	>99.9%	$5.70^{+0.33}_{-0.34}$	146^{+45}_{-32}	217^{+67}_{-47}	16^{+2}_{-2}	$0.04^{+0.03}_{-0.01}$, $0.06^{+0.04}_{-0.02}$
HIP73990B	$6.04^{+0.52}_{-0.34}$	161^{+12}_{-13}	281^{+7}_{-6}	>99.9%	$7.84^{+0.77}_{-0.62}$	21^{+30}_{-5}	50^{+31}_{-33}	20^{+4}_{-3}	$0.01^{+0.02}_{-0.05}$, $0.03^{+0.02}_{-0.02}$
HIP73990C	$5.95^{+0.55}_{-0.44}$	254^{+12}_{-38}	48^{+13}_{-3}	>99.9%	$7.75^{+0.80}_{-0.72}$	22^{+38}_{-6}	54^{+40}_{-30}	32^{+5}_{-7}	$0.01^{+0.02}_{-0.01}$, $0.03^{+0.03}_{-0.02}$
HIP74865B	$5.03^{+0.28}_{-0.23}$	201^{+19}_{-12}	115^{+3}_{-3}	>99.9%	$7.51^{+0.59}_{-0.60}$	28^{+37}_{-10}	65^{+36}_{-25}	23^{+6}_{-4}	$0.02^{+0.03}_{-0.01}$, $0.04^{+0.03}_{-0.02}$
HIP78196B	$4.61^{+0.18}_{-0.22}$	74^{+10}_{-10}	266^{+4}_{-4}	$\lesssim$99%	$6.18^{+0.37}_{-0.42}$	98^{+42}_{-12}	152^{+56}_{-28}	9^{+2}_{-2}	$0.04^{+0.03}_{-0.01}$, $0.06^{+0.05}_{-0.02}$
HIP78233B	$4.72^{+0.11}_{-0.12}$	133^{+3}_{-3}	20^{+1}_{-1}	99.9%	$6.55^{+0.38}_{-0.36}$	86^{+12}_{-21}	124^{+27}_{-24}	19^{+2}_{-2}	$0.05^{+0.01}_{-0.01}$, $0.07^{+0.02}_{-0.02}$
HIP79124B	$4.30^{+0.10}_{-0.10}$	177^{+3}_{-3}	242^{+1}_{-1}	99.9%	$5.81^{+0.32}_{-0.34}$	135^{+38}_{-33}	201^{+56}_{-44}	22^{+2}_{-2}	$0.05^{+0.04}_{-0.02}$, $0.08^{+0.05}_{-0.02}$

Table 4.7: Masses are derived from Chabrier et al. (2000) and Baraffe et al. (1998, 2003) models.

Indeed, a 5 Myr age is required to place low mass U Sco stars on an HR diagram (Rizzuto et al. *in prep*, Preibisch and Mamajek, 2008; Kraus et al., 2015). Further, when placed on an HR diagram at least half of our targets (HIP71724, HIP78196 and HIP79124) have positions in the HR diagram that are consistent with a 5 Myr isochrone. Nonetheless, for overall consistency we report our derived masses using a 10-20 Myr age range.

4.2.3 Observation Strategy & Analysis

All the data presented in this work were obtained at L'-band wavelengths (3.76 μm) using the NIRC2 infrared camera and AO system at the W. M. Keck Observatory using , as well as the ESO Very Large Telescope ("VLT") NACO AO system and infrared camera. An observing sequence consisted of observing a target star in two opposed quadrants of the infrared camera: NIRC2 at Keck, and CONICA at the VLT. A nine hole aperture mask is used at Keck, and a seven hole mask was used at VLT, producing interferograms like that shown in Figure 1 of Hinkley et al. (2011). At both detector positions, we typically obtained 15 images (30 images total) with an effective exposure time of 20s each. Usually two to four such 30-image sequences of each target star were obtained.

We did not explicitly observe calibrator stars for each of our target stars, as is common practice. Rather, we use all of the stars in a given observing night as mutual calibrators. Those with closure phase signals indicative of a companion are weighted lower in the list of calibrators than those without. In a single observing night, this method allows roughly twice the number of Sco-Cen targets to be observed. To use the closure phase quantity to search for companions, we follow the analysis outlined in Kraus et al. (2008), Ireland and Kraus (2008) and Hinkley et al. (2011), briefly summarized here. The data are initially flatfielded, sky subtracted, aligned, and corrected for cosmic rays. The bispectrum, the complex triple product of visibilities defined by the three baselines formed from any three subapertures, is then calculated. The phase of this complex quantity is the closure phase.

As discussed in Kraus et al. (2008) and Hinkley et al. (2011), the calibrated object closure-phase is found by subtracting a weighted average of the closure-phase for the calibrator stars. For the analysis in this paper, which is motivated by the search for point sources, the squared visibilities were not used as they were noisier than the closure-phases. Each target was calibrated against all other stars to search for any deviations from single point-like sources. The Root Mean Square (RMS) calibrated closure-phase was found for each of these target-calibrator pairs, and all calibrations that resulted in an RMS closure phase more than 1.5 times the minimum for each target over all calibrators were assigned a weight of zero. In practice, this meant that each target data set was calibrated by an average of the two or three calibrator data sets obtained closest in time. The lack of perfect closure phase calibration is still the dominant source of closure-phase noise in this analysis.

4.2.4 Results

In Table 4.7 we present the key properties of our newly detected companions, including the relative L'-band contrast ratios, angular separations, position angles, absolute magnitudes for the detected companions, as well as confidence levels of each of the detected companions to these

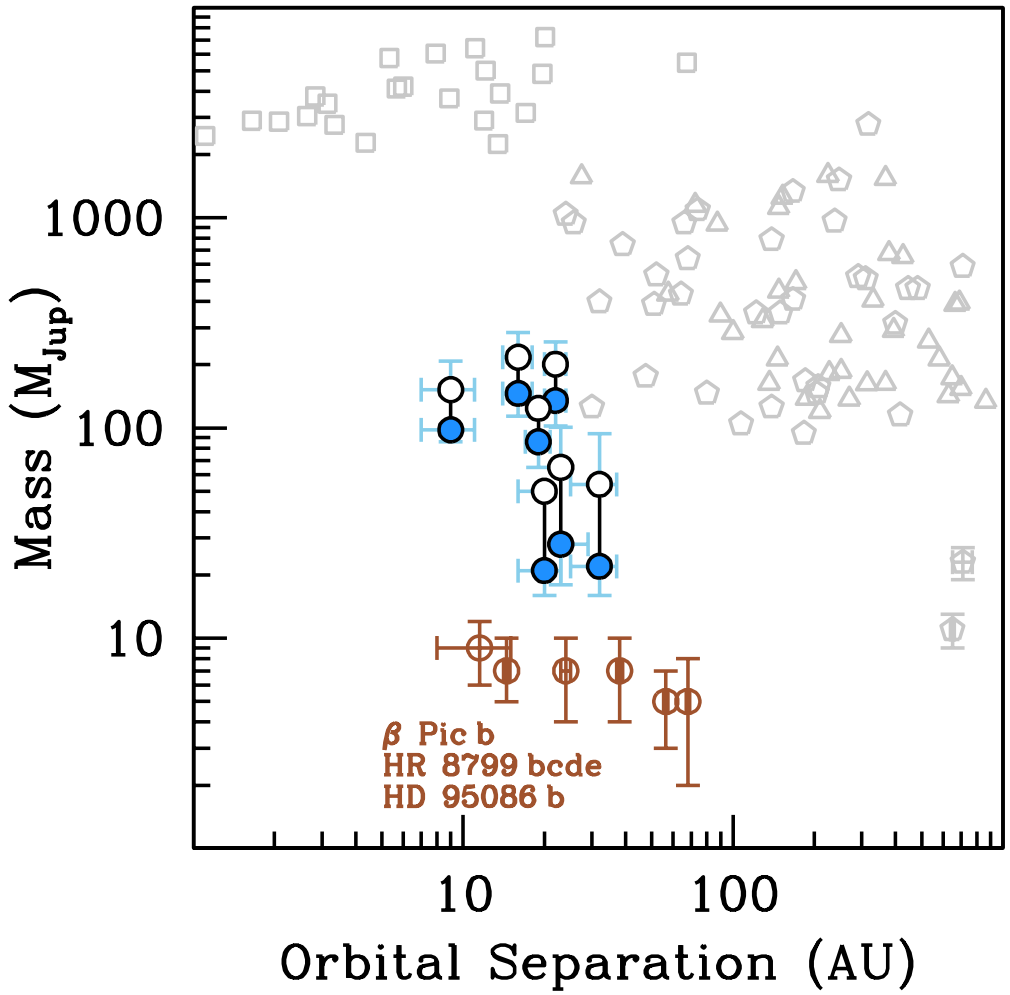

Figure 4.1: Companions to Sco-Cen stars of spectral type B, A, and F ($\gtrsim$1.5$M_{\odot}$) expressed in terms of Jupiter masses (M_J) and projected orbital separation (AU). The blue and white circles denote our new detections of companions to Sco-Cen BAF stars using aperture masking interferometry (see Table 4.7), assuming a lower limit age of 10 Myr (blue circular points), and an upper limit age of 20 Myr (white circular points). The gray symbols denote previous identifications from the literature of companions to Sco-Cen BAF stars obtained through conventional AO imaging (triangles Kouwenhoven et al., 2005), interferometry (squares Rizzuto et al., 2013) and more recent imaging studies (pentagons, Janson et al., 2013; Lafrenière et al., 2014; Bailey et al., 2014). For comparison, the brown circular symbols indicate the planetary mass companions to the young A-stars HR 8799, β Pic, and HD 95086, respectively (Marois et al., 2010; Lagrange et al., 2010; Rameau et al., 2013)

Sco-Cen BAF stars. For masses less than 0.1 $M_{\odot}$, we convert these absolute magnitudes into physical masses for the DUSTY models (Chabrier et al., 2000) corresponding to ages of 10 and 20 Myr. For masses greater than 0.1 $M_{\odot}$, we interpolate the Baraffe et al. (1998) models, assuming a mixing length parameter L_{mix}=1.9H_p, with H_p denoting the pressure scale height. Our L'-band photometry for the host stars, used to calculate the relative brightness of the companions, is obtained from the WISE W1 channel.

Figure 4.1 shows our newly detected objects in a mass versus semi-major axis diagram, where we plot the lower (upper) limit age of 10 Myr (20 Myr) for each object using the values tabuated in Table 4.7. For context, Figure 4.1 also shows several other detections of objects orbiting Sco-Cen stars of spectral type B, A, and F using conventional AO (Kouwenhoven et al., 2005; Janson et al., 2013; Lafrenière et al., 2014; Bailey et al., 2014). Also in the figure, we also show recent interferometric detections of companions with primarily stellar masses ($\gtrsim$1 $M_{\odot}$) taken from Rizzuto et al. (2013). In addition, the Figure shows the directly imaged exoplanets orbiting the closer, young ($\sim$10-30 Myr) A-stars HR 8799, β Pic, and HD 95086b (Marois et al., 2010; Lagrange et al., 2010; Rameau et al., 2013). Our objects occupy a similar orbital range (10 to 30 AU) to these directly imaged exoplanets, but with larger masses. Some works (e.g. Vigan et al., 2012) have suggested the peak of the companion distribution lies in this orbital range.

Three of our newly detected objects, HIP 73990B, HIP 73990C, and HIP 74865B, have mass ratios clearly below the Hydrogen burning limit ($\sim$72 M_{Jup}), even assuming the older 20 Myr age. These are objects at 10–30 AU that unambiguously occupy the so-called "brown dwarf desert" (e.g. Kouwenhoven et al., 2007a; Kraus et al., 2008, 2011), an observationally determined dearth of brown dwarf objects traditionally categorized as having $q \lesssim 0.1$. Any detection of objects in this mass range will be particularly important to inform theoretical and numerical models of multiple systems (e.g. Bate, 2009, and references therein).

Given the very small angular separations at which aperture masking interferometry performs ($\lesssim$0.25″), the likelihood of contamination from background stars is negligible. For our survey, the number of expected contaminants has been estimated based on the local surface density of stars in the vicinity of the targets in our sample. This density was estimated using both the 2MASS survey and a star count algorithm that combines a spatial and luminosity model for the Milky Way (for the thin/thick disk, halo, bulge and present-day mass function (Reid et al., 2002). Nonetheless, to obtain the number of expected false detections in our broad survey of 140 stars, we extrapolate the false alarm rate from Kraus et al. (2008), which predicts 0.3 false detections for 60 Sco-Cen stars. With this rate in hand, for our survey of 140 stars, we would expect $\sim$0.7 false detections. Thus, the probability of identifying seven companions, as we have done in this work, would require a false alarm rate an order-of-magnitude greater than that of Kraus et al. (2008). Such a circumstance is exceedingly unlikely, since the current study also focusses on the Sco-Cen region. Thus, the conventional need to confirm common proper motion is much less urgent. Nonetheless, we will continue to monitor these targets with the goal of fully characterizing the orbital motion of the companions, as well as establishing common proper motion with the host stars.

Of the six stars targetted in this study, only HIP 73990 has evidence for significant excess emission at 22 μm as measured by the NASA WISE mission ([3.6]-[22] μm = 1.62), suggesting the presence of a debris disk. At the same time, none of our six target stars have any statistically significant excess emission at 4.6 μm or 12 μm, which would suggest the presense of more opti-

cally thick, protoplanetary disks. HIP73990 is also our only target with more than one detected companion. We devoted several additional post-processing tests to ensure the dual detections were not spurious (e.g. optical "ghosts" in the field of view, a companion present around another mutual calibrator star, etc.). A thorough reprocessing of the data while varying the calibration scheme revealed that both detections were present irrespective of the number of mutual calibrators stars used. Furthermore, the NACO L27 camera and L'-band filter have well characterized optical ghosts present in the focal plane. However, the position of these artifacts are fixed, and are easily excluded by a mask. Nonetheless, as an additional check, we performed a data reduction using only those files with the interferograms in identical places on the focal plane. The detection of the companions were robust against these changes as well. Lastly, we rule out the possibility that the closure phase signal could perhaps be caused by aliasing from a more distant source, since Janson et al. (2013) do not mention any detection of faint companions in their observations of this star using conventional AO imaging.

4.2.5 Conclusions & Summary

In this work, we report the detection of seven companions to intermediate-mass stars of spectral types B, A, and F in the Sco-Cen association. With assumed ages of 10-20 Myr, our newly detected objects are observed shortly after the epoch of formation, residing on orbital scales comparable to objects in our solar system ($\sim$10-30 AU). The young age of these stars allows detection of brown dwarf (and potentially planetary) mass objects even with modest achieved contrasts $\Delta L' \approx$4-6 mags. We highlight our main findings in this work as follows:

1) All of our newly detected companions are unambiguously "brown dwarf desert" objects with mass ratios $q\sim$0.01-0.08. The derived masses of our newly detected companions suggest they are more massive analogs of the planetary mass companions HR8799 bcde, (Marois et al., 2010). HIP 73990 is perhaps the strongest analog for HR 8799, with multiple detected objects with masses $\sim$20-50 $M_{\rm Jup}$ ($q \approx$ 1–3%). Along with HIP 74865B, these three objects are all clearly below the Hydrogen burning limit, even assuming an age of 20 Myr.

2) The objects presented in this paper have much smaller orbital separations than the previously reported substellar companions to Sco-Cen BAF stars detected through conventional AO (Kouwenhoven et al., 2007b; Janson et al., 2013; Lafrenière et al., 2014).

3) The infrared brightnesses presented here will further serve as luminosity measurements of very young objects against which evolutionary models can be compared, thereby constraining the initial entropy of forming low mass companions (e.g. Marleau and Cumming, 2014).

4) This study also begins to fill an important gap in our knowledge of the multiplicity of intermediate mass stars at young ages (e.g. Delgado-Donate et al., 2004). Specifically, some studies suggest (e.g. Kouwenhoven et al., 2007b) that multiplicity is an *essential* outcome of the formation of intermediate mass stars, serving as a reservoir for the conserved initial angular momentum.

5) The new companions presented in this paper will be prime targets not only for follow-up spectroscopy (e.g. Hinkley et al., 2015), but also to search for fainter companions at large separations using the latest generation of dedicated exoplanet imagers such as GPI and SPHERE. Finally, as GAIA parallaxes are derived for these objects, follow-up high resolution host star spectroscopy

will be highly beneficial to better determine the host star physical properties, such as $T_{\rm eff}$, $\log(g)$, and metallicity.

Chapter 5

The Brown Dwarf Desert: Multiplicity and Formation

5.1 Multiplicity Survey of the Ophiuchus Star Forming Region

Non redundant masking interferometry offers insights into an angular regime that is difficult to target with other techniques. This offers a unique window into the processes of star formation and stellar multiplicity. In the following paper I use NRM to perfom a multiplicity survey of the nearby Ophiuchus star forming region, one of the youngest such nearby regions. This represents a sample less affected by dynamical evolution than previous work, and offers insights into the time evolution of binary parameters, important predictions of star formation theories.

Critically, by combining the multiplicity information with a census of disk hosting stars we are also able to look at the effects of stellar multiplicity on the evolution of protoplanetary disks. Previous studies of older stellar populations have shown that the presence of a close binary significantly speeds up the process of disk dispersal. This has a severe impact on the formation of giant planets in these systems, since the timeline for disk dispersal becomes shorter than the time needed to form such planets. This would lead to close binary systems having a relative lack of giant planet companions, a prediction that should be testable in the coming years with the combination of next generation radial velocity, transit and direct imaging searches.

The majority of this work was performed by myself, including the compilation of the target list, processing and analysis of the data, and the statistical analysis of the combined results (including writing software to perform this task). Interpretation of results was aided by the coauthors, as well as consultation about individual targets. The observations were conducted by several coauthors as part of a larger ongoing campaign, however the paper itself was entirely drafted by myself and improved by comments from coauthors.

The following manuscript was submitted to the Astrophysical Journal in March 2015. The version presented here has been modified from the published version based on feedback from reviewers of both this thesis and the paper.

Mapping the shores of the brown dwarf desert. IV. Ophiuchus

Anthony C. Cheetham,[1,2] Adam L. Kraus,[3] Michael J. Ireland,[4] Lucas Cieza,[5,6] Aaron C. Rizzuto[3] and Peter G. Tuthill[1]

[1]Sydney Institute for Astronomy, School of Physics, University of Sydney, NSW 2006, Australia
[2]Observatoire de Genève, Université de Genève, 51 chemin des Maillettes, 1290, Versoix, Switzerland
[3]Department of Astronomy, The University of Texas at Austin, Austin, TX 78712, USA
[4]Research School of Astronomy & Astrophysics, Australian National University, Canberra ACT 2611, Australia
[5]Nucleo de Astronomia, Universidad Diego Portales, Av. Ejército 441, Santiago, Chile
[6]Millennium Nucleus Protoplanetary Disks in ALMA Early Science, Universidad Diego Portales, Av. Ejercito 441, Santiago, Chile

Abstract

We conduct a multiplicity survey of members of the ρ Ophiuchus cloud complex with high resolution imaging to characterize the multiple star population of this nearby star forming region and investigate the relation between stellar multiplicity and star and planet formation. Our aperture masking survey reveals the presence of 4 new binary companions beyond the reach of previous studies, but does not result in the detection of any new substellar companions. We find that $43\pm6\%$ of the 114 stars in our survey have stellar mass companions between 1.3-780 AU, while $7^{+8}_{-5}\%$ host brown dwarf companions in the same interval. By combining this information with knowledge of disk-hosting stars, we show that the presence of a close binary companion (separation < 40 AU) significantly influences the lifetime of protoplanetary disks, a phenomenon previously seen in older star forming regions. At the $\sim$1-2 Myr age of our Ophiuchus members $\sim$2/3 of close binary systems have lost their disks, compared to only $\sim$30% of single stars and wide binaries. This has significant impact on the formation of giant planets, which are expected to require much longer than 1 Myr to form via core accretion and thus planets formed via this pathway should be rare in close binary systems.

5.1.1 Introduction

Multiplicity surveys provide some of the most stringest tests of stellar formation theories. The distribution and frequency of companions are key predictions of these theories that are easily tested. Radial velocity (RV) surveys have had great success at revealing close stellar and substellar companions, especially around older stars, while high resolution imaging surveys have increased our understanding of companions at wider separations.

RV surveys have revealed a wealth of both stellar and planetary mass companions in close orbits around their host stars. However, they have revealed a surprising lack of brown dwarf mass companions in close orbits, with estimates suggesting frequencies of $< 1\%$ (Marcy and Butler, 2000; Grether and Lineweaver, 2006). This phenomenon has been labelled the "brown dwarf desert".

In contrast, imaging surveys targeting wider separations have found that the frequency of such companions may not be anomalously low, but rather an extension of the binary mass-ratio function to lower masses (Metchev and Hillenbrand, 2009).

In this paper we investigate the crucial separations between these two approaches, following on from previous work in Kraus et al. (2008) and Kraus et al. (2011). These studies investigated

the Upper Scorpius subgroup of the Sco-Cen OB association and the Taurus-Auriga star forming region respectively. Both studies resulted in companion distributions consistent with a flat mass ratio distribution, finding 5 and 6 companions with mass ratios q≤ 0.1 respectively. This provides further evidence that the frequency of brown dwarf companions is consistent with the observed trend for stellar mass companions.

The distributions of orbital parameters in binary stars offers another key test of star formation models, through comparison of their predictions to the observed properties of multiple systems. Several studies have targeted binaries in the field, finding evidence that these properties are mass-dependent (Duquennoy and Mayor, 1991; Fischer and Marcy, 1992; Close et al., 2003; Raghavan et al., 2010). For example, companions to Solar mass stars have a higher mean separation than companions to low mass stars. In addition, the number of low mass companions to Solar mass stars appears high, while the distribution of companion mass ratios for low mass stars is peaked more towards unity.

However, surveys of young star forming regions have shown significant differences in many of these properties. The overall binary frequencies in these regions appear to be much higher than the field ($\gtrsim 80\%$ Ghez et al., 1993; Simon et al., 1995; Köhler et al., 2000; Kraus et al., 2008, 2011), and the shapes of the separation and mass ratio distributions appear different. Dynamical interactions may play a significant role in causing these differences, since studies of denser regions such as young clusters have shown similar results to the field (Duchêne et al., 1999; Köhler et al., 2006). A large fraction of stars in the field are thought to originate from these dense clusters, and the similarities between their properties echoes this idea.

Samples less affected by dynamical interactions provide simpler tests of binary formation processes, and so obtaining robust statistics for young star forming regions like Ophiuchus are important to test multiple star formation theories.

The relationship between binarity and disk evolution is another key link to understanding star and planet formation. While a large body of work has concentrated on the evolution and formation of planets in single star systems, the majority of solar type stars exist in multiple systems which may have a profound effect on the way in which these processes occur.

Surveys targeting disks and stellar multiplicity in nearby star forming regions have shown correlations between the presence of a binary companion and the properties and presence of a circumstellar disk (Ghez et al., 1997; Cieza et al., 2009; Duchêne, 2010; Kraus et al., 2012). These studies found that the presence of a close (≤ 40 AU) binary companion can significantly speed up the dispersal or inhibit the formation of protoplanetary disks.

By combining the results of previous multiplicity surveys of several star forming regions, Cieza et al. (2009) found that close binaries with separations less than 40 AU were half as likely to retain their disks as binary systems with larger separations. However, the timescale of this effect remains unclear.

Comparing the results for different star forming regions by age, Kraus et al. (2012) found that $\sim$2/3 of all close binaries have no disk at ages of 1-2 Myr in Taurus. Despite this, stable configurations appear to exist that allow some disks around close binaries to persist for ~ 10 Myr in Upper Scorpius. In contrast, the presence of a wider companion does not appear to affect the lifetime of protoplanetary disks at these ages. Comparison of results from the 1-2 Myr old Ophiuchus region with the regions investigated in previous studies will provide information on the

age dependent properties of these effects and the scatter between individual regions.

The relationship between the timescales of disk dispersal and giant planet formation defines the relative abundance of such planets. The two canonical giant planet formation theories of core accretion (Pollack et al., 1996) and disk instability (Boss, 2001) predict different timescales. Core accretion requires several Myr to form giant planets from protoplanetary disks (Hubickyj et al., 2005), while disk instability is most efficient at much younger ages ($\lesssim$0.5 Myr, Boss 2001). The short lifetime of disks in close binary systems would lead to a low occurence rate of giant planets that formed through core accretion, a key prediction to differentiate between the two theories.

We utilise the technique of Sparse Aperture Masking (SAM) to perform a high-resolution survey of the nearby Ophiuchus star forming region. The relatively small distance to this association as well as its relative youth provide an ideal opportunity to investigate changes in both the prevalence of brown dwarf companions and the relationship between disk evolution and multiplicity. Comparison of results from the $\sim$1-2 Myr old Ophiuchus region with the older regions investigated in previous studies will provide information on the age dependent properties of these effects.

5.1.2 Survey Sample

This survey consists of observations of members of the ρ Ophiuchus cloud complex. The star formation history of this region is complex, with several periods of recent star formation. Its similar location and distance to the Sco-Cen OB association has led to the suggestion that the most recent episode of star formation in this region was triggered by an interaction between the large L1688 cloud and a shock wave from the Upper Scorpius sub group, occuring approximately 1-1.5 Myr ago (Vrba, 1977; Loren and Wootten, 1986).

The first estimates of the distance to the cloud complex suggested a value of around 160 pc Bertiau (1958); Whittet (1974). However, more recent studies have measured the distance to be between 119-135 pc de Geus et al. (1989); Lombardi et al. (2008); Mamajek (2008). In this study, we adopt a value of 130 pc for all of our association members.

Members of Ophiuchus have a wide range of ages consistent with several episodes of star formation in different regions. A young population of Young Stellar Objects (YSOs) in the centre of the cloud with a median age of 0.3 Myr was identified by Greene and Meyer (1995) and Luhman and Rieke (1999), but an older population of YSOs covering a larger area has an age of 2 Myr, as noted by Wilking et al. (2005). These studies estimated the age of observed members through the comparison of H-R diagram positions to model evolutionary tracks, a process that can introduce large systematic effects, as illustrated by the analysis of F-type stars in Sco-Cen by Pecaut et al. (2012). In this study we adopt an age of 1-2 Myr and focus on members close to the L1688 cloud core.

Our target list was arrived at by considering membership of the ρ Ophiuchus cloud complex. Since no canonical survey exists, a conservative approach was taken where all possible members from the literature were considered and then subject to a cut in right ascension and declination (16 20 00 to 16 40 00 and -23 00 00 to -27 00 00 respectively). This was chosen to cover a wide region around the L1688 cloud that hosts ongoing star formation. The initial target list was made by compiling targets from Herbig and Bell (1988), Bouvier and Appenzeller (1992), Meyer et al.

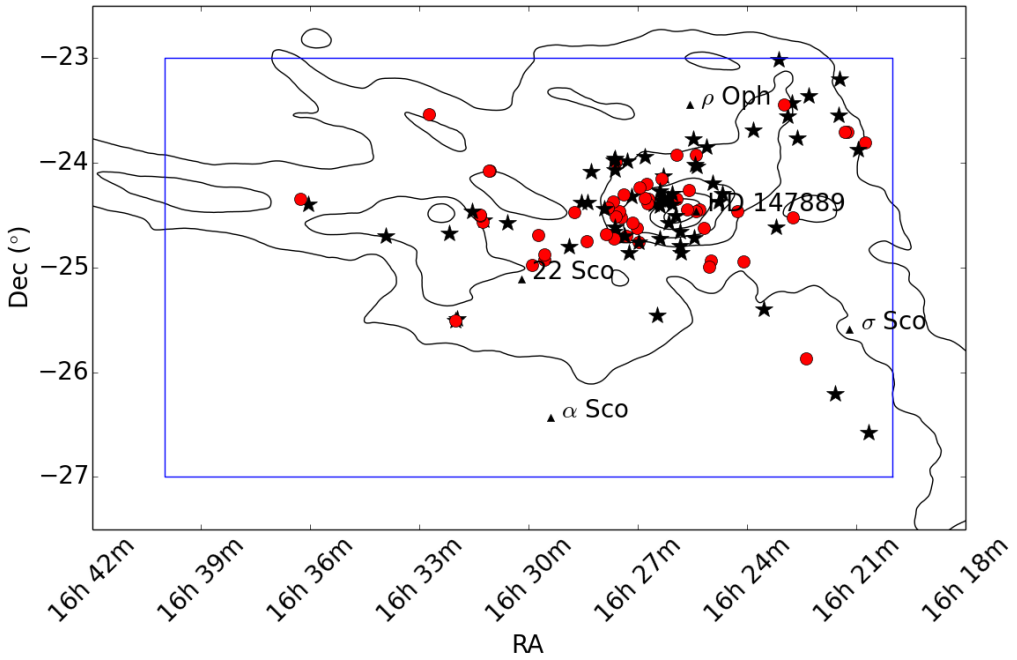

Figure 5.1: Distribution of targets that fit the criteria described in section 5.1.2, plotted over contours marking 1, 2.5, 5, 10 and 15 mag of (B-V) extinction from Schlegel et al. (1998). Several prominent nearby stars are marked with triangles and labelled for reference, as well as HD 147889, the highest mass target in our sample. Targets marked with red circles were not obseved with aperture masking.

(1993), Martin et al. (1998), Preibisch et al. (1998), Luhman and Rieke (1999), Wilking et al. (2005), Cieza et al. (2010), and Erickson et al. (2011).

Table 5.1: Survey Sample

Name	RA (J2000)	Dec (J2000)	SpT[1]	Mass [$M_\odot$]	R[2] [mag]	K[3] [mag]	Ref.[4]	Disk?	Multiple System?
DoAr 13	16 20 39.60	-26 34 28.4	M2	0.61	14.89	9.921	6	Y	N
GSC 6794-480	16 20 45.96	-23 48 20.8	K3	2.07	12.66	8.927	7	N	N
[MMG98] RX J1620.9-2352	16 20 57.87	-23 52 34.3	K3	2.07	9.88	8.393	6	N	N
[MMG98] RX J1621.2-2342a	16 21 14.50	-23 42 20.0	K7	0.98	12.51	8.99	6	N	N
HIP 80126	16 21 19.18	-23 42 28.7	B5	5.90	6.98	6.418	12	Y	N
[MMG98] RX J1621.4-2312	16 21 28.44	-23 12 11.0	K7	0.98	13.55	8.739	6	N	N
[MMG98] RX J1621.4-2332b	16 21 28.81	-23 32 38.9	M0	0.82	11.02	7.167	6	N	Y
WSB 9	16 21 34.69	-26 12 26.9	K5	1.20	12.88	8.864	5	Y	N
WSB 12	16 22 18.52	-23 21 48.0	K5	1.20	13.03	8.109	12	Y	N
WSB 13	16 22 22.31	-25 52 19.9	M4	0.29	14.56	9.438	5	N	N
[MMG98] RX J1622.6-2345	16 22 37.57	-23 45 50.8	M2.5	0.57	14.89	9.734	6	N	N
SSTc2d J162245.4-243124	16 22 45.39	-24 31 23.7	M3	0.48	14.82	9.063	12	Y	Y
[MMG98] RX J1622.7-2325a	16 22 46.80	-23 25 33.1	M1	0.72	14.23	8.233	6	N	Y
[MMG98] RX J1622.8-2333	16 22 53.36	-23 33 10.1	K7-M0	0.89	15.2	9.394	6	N	N
[MMG98] RX J1622.9-2326	16 22 59.85	-23 26 34.8	K7-M0	0.89	14.27	8.945	6	Y	N
GSC 6794-537	16 23 07.83	-23 00 59.6	K2	2.66	11.31	8.183	7	N	N
SSTc2d J162312.5-243641	16 23 12.56	-24 36 41.3	M2	0.61	15.39	8.571	12	Y	N
2MASS J16233234-2523485	16 23 32.34	-25 23 48.5	G1	3.69	11.22	7.695	7	N	N
[MMG98] RX J1623.8-2341a	16 23 49.40	-23 41 27.2	K5	1.20	14.04	8.599	6	N	N
2MASS J16240632-2456468	16 24 06.32	-24 56 46.8	K0	3.40	12.79	8.28	6	N	N
[MMG98] RX J1624.2-2427	16 24 15.86	-24 27 35.2	M0.5	0.77	14.99	9.231	6	N	N
[E2011] 4-29	16 24 41.04	-24 17 48.8	M2	0.61	17.96	8.976	13	N	N
[E2011] 3-37	16 24 46.80	-24 22 21.0	K7	0.98	15.95	7.966	13	N	N
[WMR2005] 2-15	16 24 57.29	-24 11 24.0	M3.5	0.38	16.07	9.233	10	N	N
WSB 18	16 24 59.74	-24 56 00.8	M3.5	0.38	16.35	9.441	13	Y	Y
WSB 19	16 25 02.08	-24 59 32.3	M4.5	0.20	15.45	9.22	13	Y	Y
SSTc2d J162506.9-235050	16 25 06.92	-23 50 50.2	M3	0.48	15.55	9.509	12	Y	N
2MASS J16251188-2437081	16 25 11.88	-24 37 08.1	K6	1.09	17.2	9.275	13	N	N
EM* SR 2	16 25 19.23	-24 26 52.6	G9	3.53	9.49	7.798	11	N	Y
[MMG98] RX J1625.3-2402	16 25 22.43	-24 02 05.6	K5	1.20	15.11	8.763	6	N	N
EM* SR 1	16 25 24.30	-24 27 56.5	B2	10.90	7.49	4.581	3	N	N
ROXs 2	16 25 24.34	-23 55 10.3	K3	2.07	14.74	8.378	4	N	Y
[E2011] 3-45	16 25 26.12	-24 01 05.8	K7	0.98	17	9.185	13	N	N
EM* SR 8	16 25 26.86	-24 43 08.9	K7	0.98	13.01	8.662	6	N	N
EM* SR 6	16 25 28.63	-23 46 26.5	K1	2.95	11.02	7.822	6	N	Y
YLW 19	16 25 36.73	-24 15 42.4	K4	1.63	15.47	8.38	13	Y	Y
WLY 2-3	16 25 39.58	-24 26 34.9	M2	0.61	12.53	8.954	13	Y	Y
ROXs 3	16 25 49.64	-24 51 31.8	K8	0.92	12.97	8.784	13	N	N
WLY 2-10	16 25 50.52	-24 39 14.5	K5.5	1.15	13.88	8.33	10	N	N
[E2011] 1-3	16 25 50.56	-24 47 35.8	K0	3.40	15.3	9.122	13	N	N
ROXs 5	16 25 55.82	-23 55 09.9	K7	0.98	13.32	8.382	4	N	Y
EM* SR 4	16 25 56.15	-24 20 48.1	K4.5	1.35	12.11	7.518	10	Y	N
GSS 20	16 25 57.52	-24 30 31.7	K5.5	1.15	14.79	8.319	10	N	N
DoAr 21	16 26 03.02	-24 23 36.0	K1	2.95	9.34	6.227	12	Y	N

[4]For targets whose most recent classification in the literature provided a range of possible spectral types, the mid-range spectral type was used.

[4]R magnitudes taken from NOMAD (Zacharias et al. (2004)).

[4]K magnitudes taken from 2MASS (Skrutskie et al. (2006)).

[4]Spectral Type References: (1) Elias (1978); (2) Herbig and Bell (1988); (3) Houk and Smith-Moore (1988); (4) Bouvier and Appenzeller (1992); (5) Meyer et al. (1993); (6) Martin et al. (1998); (7) Preibisch et al. (1998); (8) Luhman and Rieke (1999); (9) Doppmann et al. (2003); (10) Wilking et al. (2005); (11) Torres et al. (2006); (12) Cieza et al. (2010); (13) Erickson et al. (2011).

Table 5.1: Survey Sample

Name	RA (J2000)	Dec (J2000)	SpT[1]	Mass [$M_\odot$]	R[2] [mag]	K[3] [mag]	Ref.[4]	Disk?	Multiple System?
VSSG 19	16 26 03.29	-24 17 46.4	M2	0.61	15.4	9.115	13	N	N
EM* SR 3	16 26 09.31	-24 34 12.1	B6	5.20	10.6	6.504	1	N	N
GSS 26	16 26 10.33	-24 20 54.8	K8	0.92		8.474	8	Y	N
GSS 29	16 26 16.84	-24 22 23.1	K6	1.09	18.01	8.201	13	Y	N
DoAr 24	16 26 17.06	-24 20 21.6	K4.5	1.35	13.21	8.063	10	Y	N
[MMG98] RX J1626.3-2407a	16 26 18.77	-24 07 19.0	M3.25	0.38	15.7	9.353	13	N	Y
WSB 28	16 26 20.97	-24 08 51.8	M2	0.61	15.49	9.502	13	N	Y
GSS 31	16 26 23.35	-24 20 59.7	G6	3.62	13.61	6.57	10	Y	Y
DoAr 25	16 26 23.67	-24 43 13.8	K5	1.20	12.99	7.847	10	Y	N
GSS 32	16 26 24.04	-24 24 48.0	K5	1.20	18.68	7.323	13	Y	N
Elia 2-24	16 26 24.07	-24 16 13.4	K5.5	1.15	16.87	6.684	10	Y	N
ROXs 12	16 26 27.74	-25 27 24.7	M0	0.82	15.3	9.211	4	Y	Y
GSS 35	16 26 34.16	-24 23 28.2	B3	7.60	15.24	6.317	10	N	Y
GSS 37	16 26 42.85	-24 20 29.9	M1	0.72	16.7	7.878	13	Y	Y
GSS 39	16 26 45.02	-24 23 07.7	K8	0.92		8.955	8	Y	N
WSB 38	16 26 46.43	-24 12 00.0	G3.5	3.65		7.485	10	Y	Y
WSB 40	16 26 48.64	-23 56 34.1	K5.5	1.15	15.42	8.448	13	Y	N
VSSG 3	16 26 49.23	-24 20 02.9	K6	1.09	20.8	8.686	8	N	Y
ISO-Oph 83	16 26 56.77	-24 13 51.5	K7	0.98	19.42	9.25	10	Y	N
EM* SR 24 N	16 26 58.43	-24 45 31.8	K8	0.92		7.549	8	Y	Y
EM* SR 24 S	16 26 58.50	-24 45 36.8	K1	2.95	10.6	7.057	13	Y	Y
YLW 5	16 27 02.33	-24 37 27.2	B8-A7	2.45		8.064	8	..	N
[GY92] 211	16 27 09.10	-24 34 08.1	K8	0.92		8.915	8	Y	N
EM* SR 21	16 27 10.27	-24 19 12.7	G1	3.69	13.25	6.719	6	Y	Y
WSB 46	16 27 15.13	-24 51 38.8	M2	0.61	13.84	9.392	10	Y	N
[E2011] 6-62	16 27 17.81	-23 58 45.4	K8	0.92	15.12	8.731	13	N	N
EM* SR 12	16 27 19.51	-24 41 40.3	M0	0.82	13	8.407	10	N	Y
WLY 1-13	16 27 21.46	-24 41 43.0	<K0	3.40		8.483	8	Y	N
VSSG 22	16 27 22.91	-24 17 57.3	K6	1.09		9.454	8	N	N
VSSG 25	16 27 27.38	-24 31 16.5	M0	0.82		9.316	8	Y	Y
VSSG 17	16 27 30.18	-24 27 43.3	K8	0.92		9.023	8	Y	Y
WLY 1-18	16 27 33.11	-24 41 15.2	M2	0.61	18.77	7.806	9	Y	N
ROXs 30A	16 27 37.14	-23 59 33.0	K3	2.07	14.74	10.06	13	N	N
YLW 46	16 27 37.18	-24 30 35.0	A0	2.90	17.44	7.581	13	Y	N
DoAr 32	16 27 38.32	-23 57 32.4	K6	1.09	13.88	7.94	13	Y	N
YLW 47	16 27 38.32	-24 36 58.5	K5.5	1.15	18.87	8.271	10	Y	N
[MMG98] RX J1627.2-2404a	16 27 38.33	-24 04 01.3	K5.5	1.15	15.67	9.003	13	N	N
DoAr 33	16 27 39.01	-23 58 18.7	K5.5	1.15	13.88	8.205	10	Y	N
WSB 52	16 27 39.42	-24 39 15.5	K5	1.20	17.04	8.464	10	Y	N
YLW 45	16 27 39.82	-24 43 15.0	G5-K7	2.95		8.99	8	Y	Y
EM* SR 9	16 27 40.28	-24 22 04.0	K5	1.20	11.87	7.207	10	Y	Y
VSSG 14	16 27 49.87	-24 25 40.2	A7	1.84	14.33	7.301	10	N	Y
WLY 2-55	16 27 52.09	-24 40 50.3	K7.5	0.95	14.92	8.126	10	N	Y
EM* SR 10	16 27 55.58	-24 26 17.9	M2	0.61	13.42	8.896	10	Y	N
[MMG98] RX J1628.2-2405	16 28 16.73	-24 05 14.2	K6	1.09	16.15	8.859	13	Y	N
[WMR2005] 2-30	16 28 23.33	-24 22 40.5	K5	1.20	16.3	8.622	10	Y	N
HIP 80685	16 28 25.16	-24 45 00.9	F2	1.52	7.3	6.511	13	N	N
EM* SR 20	16 28 32.66	-24 22 44.9	G7	3.60	12.93	6.849	10	Y	Y
EM* SR 13	16 28 45.27	-24 28 19.0	M3.75	0.38	13.29	7.996	13	Y	Y
WSB 63	16 28 54.07	-24 47 44.2	M1.5	0.66	15.41	8.904	10	Y	N
ROXs 35A	16 29 33.97	-24 55 30.3	K3	2.07	12.41	8.531	4	N	N
EM* SR 14	16 29 34.41	-24 52 29.2	G4	3.64	10.04	8.878	4	N	N
SSTc2d J162944.3-244122	16 29 44.27	-24 41 21.8	M4	0.29	14.71	9.144	12	Y	Y
HIP 80799	16 29 54.59	-24 58 45.9	A2	2.54	7.75	7.309	4	Y	N
ROXs 39	16 30 35.63	-24 34 18.8	K6	1.09	12.3	8.025	8	N	Y
CoKu Haro 1-14 c	16 31 04.40	-24 04 33.3	K3	2.07	11.87	7.784	2	Y	N
Haro 1-14	16 31 05.16	-24 04 40.1	M0	0.82	12.75	8.576	2	Y	N
ROXs 42B	16 31 15.01	-24 32 43.6	M0	0.82	13.64	8.671	4	N	Y

Table 5.1: Survey Sample

Name	RA (J2000)	Dec (J2000)	SpT[1]	Mass [$M_{\odot}$]	R[2] [mag]	K[3] [mag]	Ref.[4]	Disk?	Multiple System?
ROXs 42C	16 31 15.74	-24 34 02.2	K6	1.09	10.99	7.129	12	Y	Y
ROXs 43A	16 31 20.12	-24 30 05.2	G0	3.71	10.36	6.729	4	N	Y
ROXs 43B	16 31 20.19	-24 30 00.9	K5	1.20		7.089	4	N	Y
Haro 1-16	16 31 33.46	-24 27 37.3	K3	2.07	12.35	7.61	4	Y	N
ROXs 45D	16 31 57.68	-25 29 33.6	K0	3.40	14.11	9.865	4	N	N
DoAr 49	16 32 00.58	-25 30 28.7	K7	0.98	13.08	9.478	4	N	N
DoAr 50	16 32 01.60	-25 30 25.3	K7-M0	0.89	11.07	9.394	4	N	N
ROXs 47A	16 32 11.79	-24 40 21.3	K2	2.66	12.52	7.929	4	Y	Y
[MMG98] RX J1632.7-2332	16 32 44.37	-23 32 12.7	M3	0.48	14.63	10.699	6	..	N
SSTc2d J163355.6-244205	16 33 55.60	-24 42 04.9	K7	0.98	15.04	8.797	12	Y	N
SSTc2d J163603.9-242344	16 36 03.95	-24 23 44.5	M4	0.29	16.51	8.881	12	Y	N
[MMG98] RX J1636.2-2420	16 36 16.87	-24 20 34.5	M3	0.48	14.98	9.99	6	N	N

Our targets were further restricted to those members with measured photometry and known spectral types. Considering the limiting magnitudes for reasonable AO correction at Keck and the VLT, targets fainter than R = 15 mags and K = 9.5 mags (for the Keck NIRC2 visible WFS and the VLT NACO IR WFS respectively) were not included. In an attempt to give a sample with better mass completeness, stars with spectral types later than M4 were observed but excluded from statistical analysis.

Out of the 236 possible Ophiuchus members from the literature, 114 fit these criteria. These targets are listed in Table 4, and their distribution on the sky is shown overlaid on an extinction map of the Ophiuchus L1688 cloud in Figure 5.1.

We have compiled the results of previous multiplicity surveys of ρ Ophiuchus members performed by Simon et al. (1995), Koresko (2002), Barsony et al. (2003), Ratzka et al. (2005) and Cieza et al. (2010), which contain 38 companions to members of our target list. Due to difficulties with observing wide equal binary systems the majority of known multiple systems were not reobserved, which will introduce a bias against the detection of higher order systems. The exceptions to this were the stars ROXs 12, ROXs 42B, ROXs 47A, EM* SR 20, EM* SR 21, EM* SR 24 S-N and GSS 31. The secondaries in these systems were either wide enough to allow the individual components to be studied separately, close enough to be unresolved by the AO system, or faint enough to allow the AO system to lock on the primary. The EM* SR 24 S-N and ROXs 43A-B components were bright enough to make our target list individually and are included separately.

The 0.9 arcsec binary [MMG98] RX J1622.7-2325a was also added. This companion was found by Prato (2007), from AO images taken in conjunction with their spectroscopic observations. Both components were spectrally classified, and so we adopt a contrast ratio that preserves this classification.

Two of our targets host known wide companions with masses close to or below the deuterium burning limit (ROXs 42B and ROXs 12). Both have been confirmed as comoving with their host star (Kraus et al., 2014; Currie et al., 2014).

The star DoAr 21 was also found to be a binary in VLBA measurements by Loinard et al. (2008). However, the small angular separation of the components (5 mas) put it outside our region of interest and so it was reobserved and considered a single star in our analysis to avoid biasing our results.

We have included the detection limits from the multiplicity surveys in the literature for both

observed multiples and non-detections to provide information on more widely separated companions. Combined, this data covers 80 of our targets.

Two M dwarfs that failed our spectral type cut were observed: EM* SR 22 (M4.5) and SSTc2d J162224.4-245019 (M5). The stars [MMG98] RX J1625.2-2455b, [MMG98] RX J1624.8-2359 and WSB 74 were also observed. These were considered as possible members by several surveys, but have not have their membership firmly established. Finally, Elia 2-29 was observed, despite having no measured spectral type. The results of these observations are reported here, but are not included in our statistical analysis or target list.

Stellar and companion properties

Stellar properties for pre-main sequence stars are difficult to estimate, due to a lack of observational data to constrain stellar evolutionary models. Masses can be uncertain by factors of 2 or more, due to unresolved multiplicity or intrinsic variability. For these reasons, any inferred properties should be treated with caution. Relative properties, such as the mass ratio q are less affected by these systematics and are much less uncertain.

Masses for each target were estimated using the methods outlined in Kraus and Hillenbrand (2007). Since no single set of stellar models spans the entire range of spectral types found here, it was necessary to combine several independent models. For high mass stars (spectral type F2 and earlier) the temperature scales of Schmidt-Kaler (1982) were used to estimate masses directly from the spectral type. For lower mass stars the effective temperatures were estimated by combining the temperature scales of Schmidt-Kaler (1982) with the M dwarf temperature scales from Luhman et al. (2003). The masses were then calculated using the isochrones of Chabrier et al. (2000) (C00), Baraffe et al. (1998) (B98) and Siess et al. (2000) (S00) at 1 Myr, approximately the median age of Ophiuchus members. The C00 isochrones were used for 0.001-0.1 $M_{\odot}$, B98 was used for 0.1-0.5 $M_{\odot}$, a mass weighted average of B98 and S00 was used for the range 0.5-1.0 $M_{\odot}$, and S00 was used for $M > 1.0\,_{\odot}$.

Companion masses were calculated using the predicted absolute magnitudes from the isochrones and the measured contrast in the observed band.

Disk Hosting Stars

To determine which of our targets host disks, we use data from the "From Molecular Cores to Planet Forming Disks" Spitzer legacy survey (Evans et al., 2003), which covered most of Ophiuchus. One product of this survey was the identification of YSO candidates based on the presence of infrared excesses across SED measurements covering 4.5-24 μm[5], and we adopt these results.

For those targets without a classification, we use the infrared excess measured by WISE (Wright et al., 2010). We use an approach similar to Luhman and Mamajek (2012), by comparing the K_s-$W4$ colour as a function of spectral type for all targets. This metric easily separates the disk hosting population.

[5]For futher details on the criteria used to identify disk hosting stars in the Spitzer survey, see Evans et al. (2007).

5.1.3 Observations and Data Analysis

Observations

The targets were observed over several years using the Keck NIRC2 instrument with its visible AO system, from 2008 through 2013. One dataset was also taken with the VLT NACO instrument and IR AO system, allowing targets with bright IR magnitudes to be observed. Both instruments have several aperture masks installed in a pupil wheel (Tuthill et al., 2006; Tuthill et al., 2010). A summary of the observations can be seen in Table 5.2.

The observing strategy for our observations was similar to that used in Kraus et al. (2008). Targets were observed in groups of $\sim 5-19$ objects based on their brightness and location in the sky, with nearby calibrator stars regularly observed to estimate instrument systematics. Calibrators were chosen to have similar visible and infrared magnitudes to the targets in each group. In total 63 targets were observed, with total integration times between $8-160$ s based on the target brightness and chosen to give a similar number of total counts on the detector.

Data Analysis and Detection Limits

The aperture masking data was analysed with a data pipeline developed at the University of Sydney, one of two commonly used software packages for processing such data. A more thorough description of this pipeline can be found in other work (e.g. Kraus et al., 2008), but a short summary follows. Images are background subtracted, flat fielded and windowed with a super-Gaussian function with a FWHM of 500 mas, before complex visibilities are measured from the Fourier transform of the image. These raw visibilities are then turned into closure phases using a matched filter approach.

Closure phase calibration is achieved by estimating the intrumental closure phases from the average of those measured on the calibrator stars, then subtracting this estimate from the target closure phases. Targets that showed no sign of a closure phase signal were used as additional calibrator stars for the remaining targets in their observing group.

To determine the limits for companion detection, a Monte-Carlo approach was taken. For each dataset a set of 10,000 random closure phases was drawn from a Gaussian distribution, with a width set by the uncertainty on each closure phase. A model fit was performed for each set of closure phases, yielding a list of 10,000 fake detections that were fit only to noise. To be considered bona-fide, a companion had to have a contrast ratio lower than a 99.9% (3.3σ) detection limit, calculated as the contrast ratio for which 99.9% of the fake detections with a similar separation had a higher contrast.

The detection limits calculated from each observation are shown plotted in Figure 5.2, expressed as the smallest detectable mass of the secondary component.

For the star ROXs 47A, a different calibration scheme was used. This star is a known tertiary system from Barsony et al. (2003). The wider secondary companion was well within the instrument field of view, and appeared to have a significant influence on the measured closure phases of the primary. To account for this, the closure phases from the secondary component were measured and used to calibrate those from the primary. This resulted in a significant improvement in calibration, and a clean detection of the tertiary component.

Table 5.2: Summary of aperture masking observations

Date	Telescope	Aperture Mask	Filter	Targets Observed
18/06/2008	Keck	9 hole	Kp	[MMG98] RX J1620.9-2352, [MMG98] RX J1621.4-2312, WSB 12, GSC 6794-537, 2MASS J16233234-2523485, DoAr 21, EM* SR 3, EM* SR 24 S, EM* SR 21, EM* SR 10, [MMG98] RX J1621.4-2332b, EM* SR 6, [MMG98] RX J1625.2-2455b
31/05/2009	Keck	18 hole	Hcont	HIP 80126
01/06/2009	Keck	9 hole	CH4_short	EM* SR 6, ROXs 47A
05/04/2010	Keck	9 hole	CH4_short	EM* SR 24 S, ROXs 47A, Haro 1-16
23/04/2011	Keck	9 hole	Kp	DoAr 25, EM* SR 8, WSB 12, DoAr 49, DoAr 24, WSB 46, WLY 2-10, DoAr 32, SSTc2d J162506.9-235050, WSB 63, SSTc2d J163355.6-244205, [MMG98] RX J1624.8-2359, WSB 74
24/04/2011	Keck	9 hole	Kp	ROXs 3, DoAr 25, ROXs 12, GSS 31, WLY 2-10, DoAr 32, DoAr 33, [MMG98] RX J1623.8-2341a, ROXs 45D, SSTc2d J162506.9-235050, WSB 74, [MMG98] RX J1622.7-2325a
04/06/2011	Keck	9 hole	Lp	DoAr 21, EM* SR 21, Haro 1-16
05/06/2011	Keck	9 hole	Lp	DoAr 21, EM* SR 3, EM* SR 21, Haro 1-16
23/06/2011	Keck	9 hole	Kp	EM* SR 24 S, ROXs 42B, EM* SR 6, EM* SR 20
14/04/2012	Keck	9 hole	CH4_short	EM* SR 24 S, GSS 31, GSS 20, Haro 1-16, [MMG98] RX J1625.3-2402, WSB 40, [WMR2005] 1-21, EM* SR 22, EM* SR 20, GSS 35
06/05/2012	Keck	9 hole	Lp	EM* SR 24 S, DoAr 25, EM* SR 21, GSS 31, DoAr 32, Haro 1-16
07/07/2012	Keck	9 hole	Kp	WLY 2-10, [MMG98] RX J1622.6-2345, [MMG98] RX J1622.8-2333, EM* SR 6
08/07/2012	Keck	9 hole	Kp	DoAr 25, GSS 31, DoAr 33, [MMG98] RX J1623.8-2341a, [MMG98] RX J1625.2-2455b
09/03/2013	VLT	7 hole	Ks	SSTc2d J162224.4-245019, [E2011] 3-37, WLY 1-18, ROXs 39, GSS 29, YLW 47, WSB 52, SSTc2d J162312.5-243641, WLY 1-13, GSS 26, [E2011] 6-62, SSTc2d J163603.9-242344, WSB 9, SSTc2d J162224.4-245019
10/03/2013	VLT	7 hole	Ks	Elia 2-29, GSS 32, Elia 2-24, [E2011] 1-3, [E2011] 4-29, VSSG 19, [MMG98] RX J1627.2-2404a , [MMG98] RX J1628.2-2405 , [WMR2005] 2-30, [MMG98] RX J1626.3-2407a , [E2011] 3-45, [WMR2005] 2-15, DoAr 13
06/08/2013	Keck	9 hole	Kp	ROXs 42B

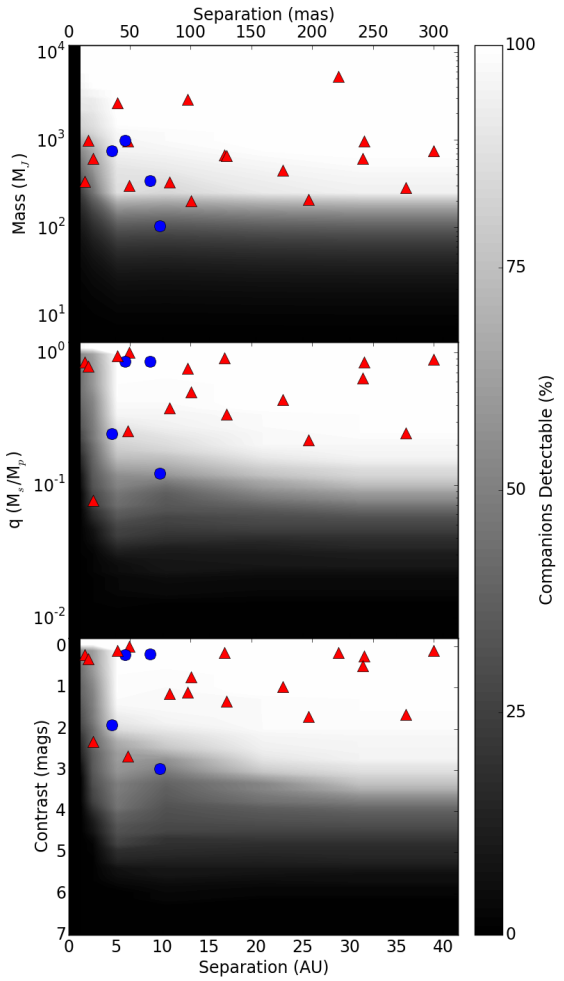

Figure 5.2: Plots showing the number of targets around which a companion at a certain separation with a certain contrast, mass or mass ratio would have been detectable. Masses are calculated using the properties from Table 4 and the approach described in Section 5.1.2. The detected companions are also plotted. Known binaries are marked with red triangles, while the new detections are shown with blue circles. The greyscale levels indicate the number of targets in our sample that reached that contrast.

Table 5.3: Non Detections

Primary	Date	Filter	Δm					
			10-20	20-40	40-80	80-160	160-240	240-320
DoAr 21	18/06/2008	Kp	2.08	3.78	4.65	4.51	4.32	4.35
DoAr 21	18/06/2008	Kp	1.53	3.41	4.34	4.03	4.06	4.06
DoAr 21	04/06/2011	Lp	0.0	3.0	4.84	5.35	5.11	5.08
DoAr 21	05/06/2011	Lp	0.0	3.18	4.98	5.49	5.3	5.26
[MMG98] RX J1620.9-2352	18/06/2008	Kp	2.15	3.82	4.69	4.58	4.38	4.4
[MMG98] RX J1620.9-2352	18/06/2008	Kp	1.53	3.41	4.34	4.05	4.06	4.06
EM* SR 3	18/06/2008	Kp	3.01	4.53	5.36	5.28	5.22	5.28
EM* SR 3	05/06/2011	Lp	0.0	2.81	4.67	5.17	4.98	4.95
EM* SR 24 S	18/06/2008	Kp	0.0	0.82	2.34	1.92	1.29	0.92
EM* SR 24 S	18/06/2008	Kp	0.0	1.4	2.79	2.45	2.46	2.46
EM* SR 24 S	14/04/2012	Lp	0.0	2.15	4.14	4.69	4.46	4.42
EM* SR 24 S	06/05/2012	Lp	0.0	2.67	4.58	5.12	5.02	5.09
2MASS J16233234-2523485	18/06/2008	Kp	2.82	4.34	5.21	5.13	5.07	5.13
GSC 6794-537	18/06/2008	Kp	2.3	3.93	4.8	4.54	4.53	4.53
EM* SR 24 S	05/04/2010	CH4_short	0.39	2.76	2.84	2.46	2.46	2.46
EM* SR 24 S	23/06/2011	Kp	1.6	3.43	4.31	4.0	4.08	4.08
ROXs 3	24/04/2011	Kp	0.96	3.06	4.07	3.79	3.84	3.84
DoAr 25	23/04/2011	Kp	0.13	2.16	3.2	3.05	2.91	3.0
DoAr 25	24/04/2011	Kp	1.89	3.63	4.58	4.32	4.37	4.37
DoAr 25	06/05/2012	Lp	2.78	4.64	5.29	5.15	5.21	5.03
DoAr 25	08/07/2012	Kp	0.0	0.14	1.46	1.11	1.07	1.07
EM* SR 8	23/04/2011	Kp	2.39	4.0	5.06	4.8	4.82	4.82
WSB 12	18/06/2008	Kp	3.12	4.62	5.45	5.33	5.28	5.33
WSB 12	23/04/2011	Kp	0.2	2.21	3.3	2.98	3.08	3.08
DoAr 49	23/04/2011	Kp	2.61	4.19	5.23	5.1	5.02	5.03
DoAr 24	23/04/2011	Kp	2.33	3.98	4.88	4.64	4.66	4.66
EM* SR 21	18/06/2008	Kp	1.69	3.5	4.41	4.12	4.16	4.16
EM* SR 21	18/06/2008	Kp	2.6	4.2	5.1	4.94	4.83	4.88
EM* SR 21	04/06/2011	Lp	0.0	3.0	4.86	5.37	5.16	5.13
EM* SR 21	05/06/2011	Lp	0.0	3.52	5.29	5.81	5.63	5.66
EM* SR 21	06/05/2012	Lp	0.0	3.29	5.09	5.67	5.51	5.51
EM* SR 10	18/06/2008	Kp	2.08	3.77	4.66	4.5	4.32	4.41
ROXs 12	24/04/2011	Kp	2.66	4.26	5.12	4.85	4.93	4.93
ROXs 12	24/04/2011	Kp	2.46	4.06	4.93	4.66	4.73	4.73
[MMG98] RX J1621.4-2312	18/06/2008	Kp	1.55	3.39	4.3	4.18	4.02	4.09
GSS 31	24/04/2011	Kp	2.54	4.14	4.93	4.68	4.75	4.75
GSS 31	14/04/2012	Lp	0.0	1.88	3.95	4.5	4.3	4.23
GSS 31	06/05/2012	Lp	0.0	2.22	4.19	4.73	4.52	4.49
GSS 31	08/07/2012	Kp	0.67	2.84	3.83	3.58	3.56	3.56
WSB 46	23/04/2011	Kp	2.23	3.89	4.85	4.54	4.61	4.61
WLY 2-10	23/04/2011	Kp	2.09	3.88	4.98	4.69	4.73	4.73
WLY 2-10	24/04/2011	Kp	3.12	4.63	5.57	5.25	5.32	5.32
WLY 2-10	07/07/2012	Kp	0.88	3.02	3.97	3.75	3.75	3.75
DoAr 32	23/04/2011	Kp	1.24	3.47	4.69	4.38	4.45	4.45
DoAr 32	24/04/2011	Kp	0.0	2.47	4.51	4.28	4.38	4.38
DoAr 32	24/04/2011	Kp	2.45	4.07	4.99	4.7	4.79	4.79
DoAr 32	06/05/2012	Lp	0.0	3.01	4.85	5.48	5.37	5.4
DoAr 33	24/04/2011	Kp	1.92	3.68	4.83	4.52	4.59	4.59
DoAr 33	24/04/2011	Kp	1.84	3.6	4.52	4.25	4.29	4.29
DoAr 33	08/07/2012	Kp	1.02	3.11	4.05	3.8	3.81	3.81
[MMG98] RX J1623.8-2341a	24/04/2011	Kp	2.18	3.86	4.93	4.59	4.7	4.7
[MMG98] RX J1623.8-2341a	08/07/2012	Kp	0.0	0.84	2.99	2.72	2.8	2.8
ROXs 45D	24/04/2011	Kp	0.0	2.52	4.27	3.99	4.12	4.12
EM* SR 22	14/04/2012	Kp	1.77	3.56	4.5	4.2	4.25	4.25
GSS 20	14/04/2012	Kp	2.26	3.92	4.9	4.72	4.59	4.62
SSTc2d J162506.9-235050	23/04/2011	Kp	0.0	0.45	2.27	1.82	1.95	1.95
SSTc2d J162506.9-235050	24/04/2011	Kp	0.93	3.04	3.99	3.7	3.75	3.75
WSB 63	23/04/2011	Kp	0.0	1.53	2.86	2.69	2.61	2.74

Table 5.3: Non Detections

Primary	Date	Filter	Δm					
			10-20	20-40	40-80	80-160	160-240	240-320
SSTc2d J163355.6-244205	23/04/2011	Kp	2.86	4.39	5.3	5.19	5.16	5.25
Haro 1-16	14/04/2012	Lp	0.0	3.68	4.34	4.86	4.63	4.58
Haro 1-16	04/06/2011	Lp	0.0	2.83	4.72	5.23	5.03	5.03
Haro 1-16	04/06/2011	Lp	0.0	1.85	3.93	4.47	4.26	4.2
Haro 1-16	05/06/2011	Lp	0.0	3.68	5.43	5.97	5.77	5.82
Haro 1-16	06/05/2012	Lp	0.0	2.4	4.34	4.86	4.63	4.58
Haro 1-16	05/04/2010	CH4_short	0.26	2.7	2.78	2.41	2.41	2.41
ROXs 42B	23/06/2011	Kp	2.0	3.71	4.6	4.29	4.35	4.35
ROXs 42B	08/06/2013	Kp	0.49	2.6	3.54	3.25	3.28	3.28
[MMG98] RX J1625.3-2402	14/04/2012	Kp	0.0	1.92	3.19	2.89	2.94	2.94
WSB 40	14/04/2012	Kp	1.75	3.54	4.61	4.3	4.39	4.39
[WMR2005] 1-21	14/04/2012	Kp	0.62	3.05	4.27	3.93	4.02	4.02
[MMG98] RX J1622.6-2345	07/07/2012	Kp	0.0	1.96	3.3	2.99	3.05	3.05
[MMG98] RX J1622.8-2333	07/07/2012	Kp	0.0	0.66	2.36	1.99	2.07	2.07
SSTc2d J162224.4-245019	09/03/2013	Ks	0.89	1.51	3.82	2.85	3.55	3.55
[E2011] 3-37	09/03/2013	Ks	0.82	1.43	3.81	2.83	3.54	3.54
WLY 1-18	09/03/2013	Ks	0.53	1.15	3.63	2.57	3.43	3.43
GSS 29	09/03/2013	Ks	1.8	2.36	4.31	3.39	4.03	4.03
YLW 47	09/03/2013	Ks	1.17	1.76	4.04	3.07	3.77	3.77
WSB 52	09/03/2013	Ks	1.64	2.2	4.23	3.24	4.0	4.0
SSTc2d J162312.5-243641	09/03/2013	Ks	1.9	2.45	4.41	3.52	4.17	4.17
WLY 1-13	09/03/2013	Ks	0.0	0.61	3.92	3.13	3.7	3.7
GSS 26	09/03/2013	Ks	1.27	1.86	4.14	3.13	3.89	3.89
[E2011] 6-62	09/03/2013	Ks	2.02	2.57	4.57	3.64	4.33	4.33
SSTc2d J163603.9-242344	09/03/2013	Ks	1.29	1.88	3.94	3.05	3.72	3.72
WSB 9	09/03/2013	Ks	2.12	2.67	4.57	3.82	4.42	4.42
Elia 2-29	09/03/2013	Ks	0.22	0.82	3.32	3.26	3.26	3.26
GSS 32	09/03/2013	Ks	1.19	1.78	3.95	3.03	3.77	3.77
Elia 2-24	09/03/2013	Ks	1.44	2.01	4.02	3.16	3.83	3.83
[E2011] 1-3	09/03/2013	Ks	0.13	0.72	2.97	1.96	2.74	2.74
[E2011] 4-29	09/03/2013	Ks	0.22	0.83	3.25	2.28	3.07	3.07
VSSG 19	09/03/2013	Ks	0.31	0.91	3.24	2.22	2.99	2.99
[MMG98] RX J1627.2-2404a	09/03/2013	Ks	0.18	0.78	3.05	2.11	2.84	2.84
[MMG98] RX J1628.2-2405	09/03/2013	Ks	0.15	0.74	3.12	2.15	2.93	2.93
[WMR2005] 2-30	09/03/2013	Ks	0.41	1.03	3.5	2.52	3.29	3.29
[E2011] 3-45	09/03/2013	Ks	0.0	0.03	2.44	1.12	2.17	2.17
[WMR2005] 2-15	09/03/2013	Ks	0.0	0.39	3.06	2.11	2.82	2.82
DoAr 13	09/03/2013	Ks	0.41	1.01	3.32	2.86	3.29	3.29
HIP 80126	31/05/2009	Hcont	4.2	6.14	6.28	6.19	6.16	6.16
EM* SR 22	14/04/2012	Kp	1.77	3.56	4.50	4.20	4.25	4.25
SSTc2d J162224.4-245019	09/03/2013	Ks	0.89	1.51	3.82	2.85	3.55	3.55
[MMG98] RX J1625.2-2455b	18/06/2008	Kp	0.63	2.81	3.79	3.49	3.51	3.51
[MMG98] RX J1625.2-2455b	08/07/2012	Kp	0.49	2.63	3.64	3.41	3.40	3.40
[MMG98] RX J1624.8-2359	23/04/2011	Kp	0	1.7	2.82	2.52	2.58	2.58
WSB 74	23/04/2011	Kp	0.58	3.65	3.98	4.01	3.76	3.67
WSB 74	24/04/2011	Kp	1.45	3.33	4.23	3.94	4.03	4.03
Elia 2-29	10/03/2013	Ks	0.22	0.82	3.32	3.26	3.26	3.26

5.1.4 Statistical framework

To turn the measured detection limits and detections into estimates of the companion frequency distributions, we have employed a statistical framework similar to that of Carson et al. (2006), Lafrenière et al. (2007a) and Evans et al. (2012). Further details may be found in these publications and the references therein, but a brief summary follows.

Table 5.4: Companions identified with aperture masking

Primary	Date	Filter	Separation [mas]	P.A. [deg]	Δm	q $[M_s/M_p]$	Mass [$M_\odot$]
[MMG98] RX J1621.4-2332b[a]	18/06/2008	Kp	74.98 ± 0.42	50.96 ± 0.30	2.97 ± 0.03	0.12	0.10
[MMG98] RX J1626.3-2407a[a]	10/03/2013	Ks	66.67 ± 0.45	299.32 ± 0.45	0.19 ± 0.02	0.85	0.33
EM* SR 20	23/06/2011	Kp	50.60 ± 0.30	240.50 ± 0.30	2.68 ± 0.02	0.23	0.83
EM* SR 20	14/04/2012	CH4_short	48.55 ± 0.31	233.52 ± 0.36	2.66 ± 0.03	0.26	0.92
EM* SR 6[a]	18/06/2008	Kp	35.60 ± 0.20	270.40 ± 0.15	1.91 ± 0.01	0.24	0.72
EM* SR 6[a]	01/06/2009	CH4_short	41.03 ± 0.22	286.46 ± 0.33	2.10 ± 0.02	0.22	0.66
EM* SR 6[a]	23/06/2011	Kp	57.80 ± 0.20	308.20 ± 0.22	1.94 ± 0.02	0.24	0.70
EM* SR 6[a]	07/07/2012	Kp	67.00 ± 1.20	314.10 ± 0.95	1.92 ± 0.07	0.24	0.71
GSS 35	14/04/2012	Kp	21.75 ± 0.39	205.11 ± 0.74	1.19 ± 0.19	0.19	1.45
GSS 35	09/03/2013	Ks	28.89 ± 3.47	268.54 ± 2.13	2.26 ± 0.43	0.08	0.60
ROXs 39[a]	09/03/2013	Ks	46.17 ± 0.18	191.10 ± 0.80	0.20 ± 0.01	0.86	0.94
ROXs 47A	01/06/2009	CH4_short	51.50 ± 0.20	99.20 ± 0.30	0.19 ± 0.01	0.90	2.39
ROXs 47A	05/04/2010	CH4_short	43.38 ± 0.18	109.06 ± 0.19	0.22 ± 0.01	0.88	2.33
[MMG98] RX J1622.7-2325a	24/04/2011	Kp	128.16 ± 0.28	280.53 ± 0.09	0.14 ± 0.01	0.90	0.65

[a]Companion reported for the first time in this work.

If f is the fraction of stars with a companion in the range of masses $[m_{min}, m_{max}]$ and semi-major axes $[a_{min}, a_{max}]$, a simple application of Bayes' Theorem results in the following expression for the probability of f given the set of data $\{d_j\}$:

$$P(f|\{d_j\}) = \frac{\mathcal{L}(\{d_j\}|f)P(f)}{\int_0^1 \mathcal{L}(\{d_j\}|f)P(f)df} \tag{5.1}$$

Each d_j is equal to 1 if a companion was detected and 0 otherwise. $\mathcal{L}(\{d_j\}|f)$ is the likelihood of the data. We adopt an ignorance prior of $P(f) = 1$.

If we let the probability of detecting a companion in the given ranges of masses and semi-major axes, if it was present, be p_j, then the probability of detecting a companion around any given star is fp_j. Similarly, the probability of not detecting a companion around that star is $1 - fp_j$. The calculation of p_j is described in section 5.1.5.

The likelihood of the data is then given by Equation 5.2.

$$\mathcal{L}(\{d_j\}|f) = \prod (1 - fp_j)^{1-d_j}(fp_j)^{d_j} \tag{5.2}$$

We then calculate a credible interval for f using the posterior $P(f|\{d_j\})$, such that the interval between $[f_{min}, f_{max}]$ contains a fraction α of the total probability. We choose an equal tail distribution, such that the probability contained in $[0, f_{min}]$ and $[f_{max}, 1]$ are equal. In the case where no companions are found in the stated interval, this is equivalent to solving Equation 5.3 for an upper bound on the companion fraction f_{max}.

$$\alpha = \int_0^{f_{max}} P(f|\{d_j\})df \tag{5.3}$$

If companions are found, the credible interval is found by solving the following two equations:

$$\frac{1-\alpha}{2} = \int_0^{f_{min}} P(f|\{d_j\})df \tag{5.4}$$

$$\frac{1-\alpha}{2} = \int_{f_{max}}^1 P(f|\{d_j\})df \tag{5.5}$$

In this work we choose a confidence level of $\alpha = 0.68$ for our analysis, equivalent to 1-σ limits, unless otherwise stated.

5.1.5 Calculation of p_j

In order to calculate the probability of detecting existing companions in the intervals of mass and semi-major axes described above, we perform a Monte Carlo simulation. This involves generating 10,000 companions with masses and angular separations according to known or proposed distributions, and then comparing their properties to the calculated detection limits. The fraction of companions that fall above the mass detection limits is then used as an estimate of p_j.

When drawing masses for our simulated companions, we considered two distributions. First is the universal mass function of Metchev and Hillenbrand (2009), proposed for companions to solar mass stars, given by

$$\frac{dN}{dq} \propto q^{-0.39} \tag{5.6}$$

We also consider a flat mass ratio distribution, consistent with the observed data from Kraus et al. (2008) and Kraus et al. (2011).

Our results indicate no significant difference in results between these distributions, and only the results of the flat mass ratio distribution are reported here.

Angular separations are calculated by combining information about semi-major axes, eccentricities, orbital phases and inclinations. For the companion eccentricities, we follow the approach of Evans et al. (2012). In the absence of constraints on the eccentricity distribution of companions, we choose to draw them from a distribution of the form

$$f\left(e\right) = 2e \tag{5.7}$$

which is arrived at based on theoretical considerations (Ambartsumian, 1937).

We convert the semi-major axis a into a projected separation through multiplication by a projection factor s, which is calculated from the eccentricity distribution. Combining the above function with the assumption that observing an orbit from any direction is equally likely, Brandeker et al. (2006) showed that the cumulative probability distribution for s is well approximated by the function

$$F_s(s) = 0.5\left[1 - \cos\left(\frac{\pi}{2}s\right)\right]. \tag{5.8}$$

We consider s in the interval $[0, 2]$.

Finally, the semi-major axes of our simulated companions are drawn from a distribution of the form

$$\frac{dN}{da} \propto a^{-1}. \tag{5.9}$$

This is consistent with the results of Kraus et al. (2008, 2011).

Since our approach involves explicitly assuming forms for the distributions of mass and separation, it can introduce systematic biases to the calculated companion fractions. However, since these apply only within each bin of mass and angular separation we can check our assumptions by comparing the observed distributions of these parameters across many bins to those used in our simulations.

5.1.6 Stellar Multiplicity of Ophiuchus Members

Detected Companions

Our aperture masking observations were sensitive to stellar companions at separations between 10-320 mas, while the imaging results from the literature were sensitive to binary systems at up to 6 arcsec. The detection limits for stars that were identified as single stars in our masking observations are listed in Table 5.3.

Eight binary systems were identified from our observations, 4 for the first time, and are listed in Table 5.4. The known close binary EM* SR 20 was recovered in two epochs, with position angles that suggest at least one complete orbit since its earliest resolved observations in 1990. Both EM* SR 20 and the new multiple system EM* SR 6 have enough epochs to formally allow an orbital fit.

Observations of the EM* SR 24 system show that the contrast ratio between EM* SR 24 S and EM* SR 24 N has changed significantly over time, with the S component substantially brighter than at the epoch of its 2MASS photometric measurements. This component is a known transition disk system, and similar infrared variability is seen in many of these objects.

Our observations failed to recover the close companion to ROXs 42B detected in Simon et al. (1995) and Ratzka et al. (2005) at separations of 56 mas and 83 mas respectively. This companion should have been detectable at separations from 10-320 mas, and by examining the raw images we can extend the outer limit to beyond 1 arcsec. The non-detection of this companion in our two observation epochs separated by 2 years makes it unlikely that orbital motion may have carried it inwards beyond our inner working angle. We have included the previously reported companion in our analysis, but note that further study is required to determine the nature of this system.

None of the companions reported here have contrasts or calculated masses consistent with brown dwarfs, despite 44 of our 63 masking observations reaching contrasts deep enough to detect such components.

Binarity Fraction

By combining high resolution multiplicity data from the literature with our SAM observations, our survey covers binary and high mass substellar companions separated by 1.3-780 AU. Overall, we find that 38 of our stars have one or more companions, while 33 are single stars across the full range of separations. The remaining 43 targets are missing either imaging or SAM observations, and so have incomplete information. This yields an overall binary fraction of $53 \pm 6\%$ assuming completeness across the whole range of separations and ignoring targets that were not observed in either imaging or SAM.

When restricting the spatial scales to 1.3-41.6 AU to coincide with those explored by the SAM observations, we find 41 single stars and 22 stars with one or more companions, yielding a binary fraction of $35 \pm 6\%$.

Using the Bayesian techniques described above we are able to include the completeness of coverage of each target to estimate the total companion frequency. Considering a range of separations between 1.3-780 AU and companion masses between 0.08-6 $M_{\odot}$, we find a total companion frequency of 43 ± 6 %. This value is between the companion frequency of $35^{+5}_{-4}\%$ found in Upper Scorpius (Kraus et al., 2008) and $64^{+11}_{-9}\%$ in Taurus-Auriga (Kraus et al., 2011).

Previous surveys of Ophiuchus members have reported similar companion frequencies. Ratzka et al. (2005) found that $29 \pm 4\%$ of targets were in multiple systems over the range 0.13-6.4 arcsec (17-830 AU), compared with our value of $32.3 \pm 5.3\%$ over the same range. Our results reflect that of Ratzka et al. (2005), who found significant differences in stellar multiplicity between the Ophiuchus and Taurus-Auriga star forming regions. Despite similarities between the two regions, the companion fraction of Ophiuchus is notably lower.

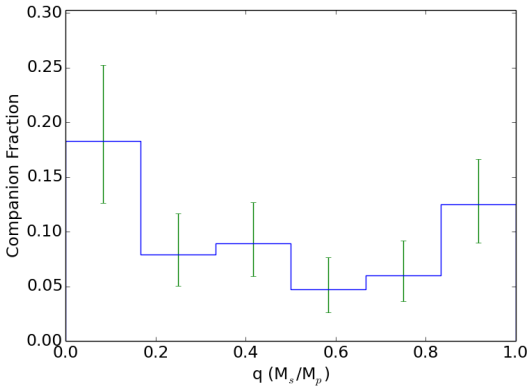

Figure 5.3: The observed binary fraction of our targets as a function of the mass ratio between the primary and secondary components. Companion separations between 1.3-780 AU were considered.

Across the range of separations explored here, nine of our targets are part of systems with 3 components (EM* SR 13, EM* SR 24 N/S, WSB 18, WSB 38, SSTc2d J162944.3-244122, ROXs 42B, ROXs 43 A/B, ROXs 47A, [MMG98] RX J1622.7-2325a), but we find no evidence of higher order multiplicity across this separation range.

The Mass Ratio Distribution

A large survey of nearby field dwarfs by Fischer and Marcy (1992) found that the distribution of companion masses is consistent with a flat mass ratio distribution for ratios $q > 0.4$. In addition, they found some evidence for a slight excess of equal mass binaries for M types, a conclusion echoed by Reid and Gizis (1997). The results of Fischer and Marcy (1992) also indicated a lack of equal mass binaries around G type stars. Similarly, Kraus et al. (2008) found a flat mass ratio distribution holds across the entire range of mass ratios for binary systems in Upper Scorpius, although with no evidence for a peak close to unity.

In Figure 5.3 we have shown the observed fraction of stars with companions with separations between 1.3-780 AU as a function of their mass ratio. The observed distribution appears consistent with a flat mass ratio distribution. We find an excess of equal mass binaries at low significance, echoing the results of Fischer and Marcy (1992) and Reid and Gizis (1997). However, we also find a similar excess of low mass ratio companions at low significance.

A one-sided Kolmogorov-Smirnov test shows that the observed distribution is consistent with a flat mass ratio distribution, with test statistic D=0.15 and a p value of 0.21.

The Separation Distribution

Studies of binaries in the field have shown that the separation distribution is approximately log-normal across a wide range of masses. In addition to this, the mean and standard deviation appear

to be mass-dependent, with high mass stars having a higher mean separation (Duquennoy and Mayor, 1991). However, binaries in young star forming regions may be better matched by a log-flat distribution with an outer cutoff that increases with the mass of the primary (Kraus et al., 2008, 2011).

Figure 5.4 shows the observed fraction of stars with companions with masses between 0.08-6 $M\odot$ as a function of the separation between the components for our sample. We have opted to plot the minimum observed separation between components (when multiple detection epochs or multiple companions are present), rather than the more physically meaningful semi-major axis of the orbit. For the majority of our binary targets, not enough detection epochs or orbital motion has been observed to allow an orbital solution to be derived, and conversions between projected separations and semi-major axes rely on extrapolated properties of binaries with much smaller separations.

The observed distribution appears log-normal in shape, with a large standard deviation. Over the range of separations explored, there is little evidence to distinguish between the proposed log-normal and log-flat distributions. A one sided Kolmogorov-Smirnov test comparing the observed distribution with a log-flat distribution gives D=0.12 and p=0.46.

We can place limits on possible distributions by comparing the observed separations to a log-normal distribution with two parameters: the mean separation μ and the standard deviation σ. The likelihood of the observed separations r_i given particular values of these parameters is given by:

$$L\left(\{r_i\}|\mu,\sigma\right) = \prod_i \frac{\exp\left[-\left(\log\mu - \log r_i\right)^2/2\sigma^2\right]}{\int_{\log r_{\rm min}}^{\log r_{\rm max}} \exp\left[-\left(\log\mu - x\right)^2/2\sigma^2\right] dx} \tag{5.10}$$

where $r_{\rm min}$ and $r_{\rm max}$ are the minimum and maximum separations explored, set as 1.3-780 AU here.

Using a uniform prior on μ and σ, we find that the most probable values for μ and σ are given by 50 and 1.0 respectively. However, the family of solutions approximating flat distributions ($\sigma \gg 1$, μ unbound) are within our uncertainties. Restricting σ to be in the range $[0.5, 2]$, we find that the mean separation is given by $\mu = 50^{+100}_{-20}$ AU, while the standard deviation is $\sigma = 1.0^{+0.6}_{-0.2}$.

5.1.7 Substellar Companions

Several of the detection limits of our aperture masking survey reach the brown dwarf mass regime ($\sim$13-80 M_J), and combined with the detection limits estimated from the imaging data of previous surveys we can estimate the occurence rate of brown dwarf companions to our targets.

Two of our targets have known widely separated companions that are close to the deuterium burning limit and have been confirmed as co-moving with their host stars. Our mass estimates for these companions places ROXs 42B b in the planetary regime (10 M_J) and ROXs 12 b in the brown dwarf regime (25 M_J), close to the values of 10 ± 4 $M_J$and 16 ± 4 $M_J$calculated by Kraus et al. (2014) (which incorporated the individual estimated ages of these systems).

The companion to the star WSB 28 also has a mass consistent with a high mass brown dwarf (75 M_J) and is likely comoving. This companion was identified by Reipurth and Zinnecker (1993) and recovered by Ratzka et al. (2005).

We detect no additional brown dwarf companions to our targets. For companions with masses between 13-80 $M_J$and separations between 1.3-780 AU, we find an observed frequency of $7^{+8}_{-5}\%$.

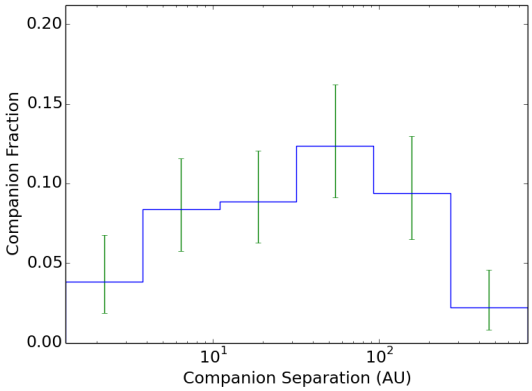

Figure 5.4: The observed binary fraction of our targets as a function of the separation between the primary and secondary components. Secondary masses between 0.08-6.0 $M_\odot$, and separations between 1.3-780 AU were considered.

For widely separated companions between 42-780 AU, we find the frequency to be $4^{+5}_{-3}\%$ while for close companions with separations between 1.3-42 AU we obtain a 1-σ upper limit of 12%.

5.1.8 The Effects of Multiplicity on Disk Evolution

Combining our census on the binarity of our targets with information on which stars host disks provides a fantastic opportunity to study the ways in which multiplicity affects the evolution of disks around young stars.

Since 17 of our targets were selected based on the infrared surveys of Luhman and Rieke (1999) and Cieza et al. (2010), their inclusion may introduce a bias towards disk hosting stars with infrared excesses and so we have not included them in the analysis presented in this section.

We find that 44 of our targets host disks, while 52 have no disk, and 1 has insufficient information to classify it. This gives an overall disk frequency of $46 \pm 5\%$, including those stars with no multiplicity information. However, this figure changes substantially depending on the binarity of the target. For binary targets, the ratio is $50 \pm 8\%$, while for confirmed single stars it is $70 \pm 9\%$.

Stars with incomplete multiplicity information have a disk frequency of $24 \pm 7\%$. This low disk frequency is likely due to the spatial distribution of those targets. Previous multiplicity surveys have targeted the central region of the L1688 cloud, which hosts the youngest stars in our sample. Evidence suggests that star formation has been ongoing in some regions of the Ophiuchus cloud complex for as long as 10 Myr (Martin et al., 1998), and the targets furthest from the L1688 central region show a correspondingly lower disk fraction. The spatial distribution of our targets and their disk hosting status are shown in Figure 5.5.

Figure 5.6 shows the result of splitting the stars based on the separation of the binary companions. From our survey we find that close binary systems (<40 AU) are less likely to host disks than wider binaries and single stars. This implies that the presence of a close binary companion either speeds up the process of disk dispersal or inhibits its formation. This conclusion echoes

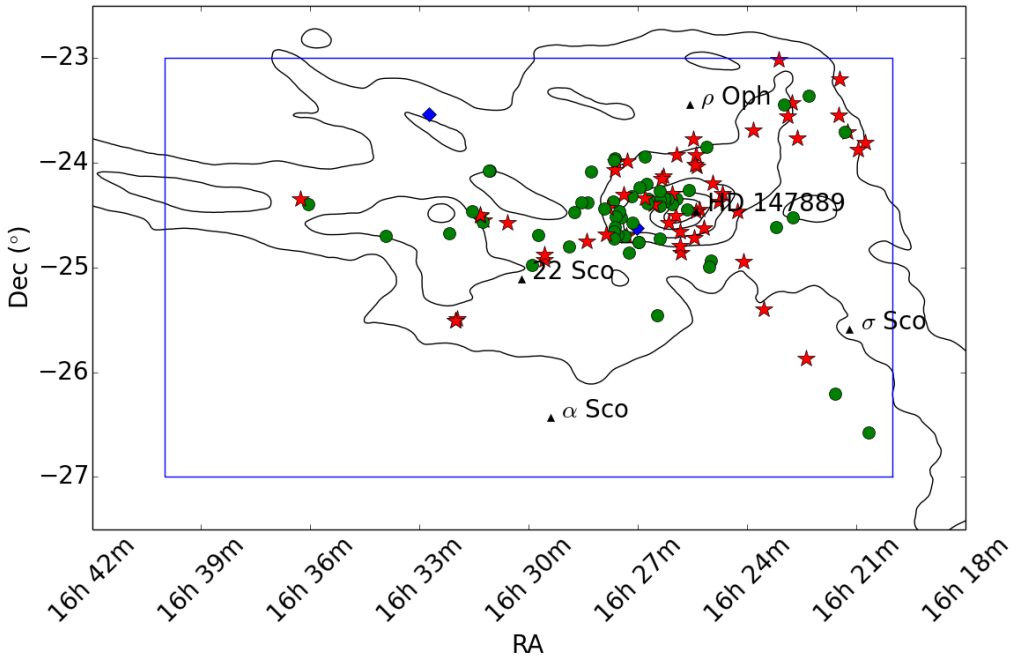

Figure 5.5: The spatial distribution of stars in our survey, labelled according to whether they possess circumstellar disks. Targets with no disk are marked with red stars, those with disks are labelled with green circles and targets with insufficient information to classify them are marked with blue diamonds. A high fraction of stars in the highest density regions have disks, while the disk fraction is lower in the West and North-West. Stars in these regions are expected to be older than those in the core, and many have lost their disks.

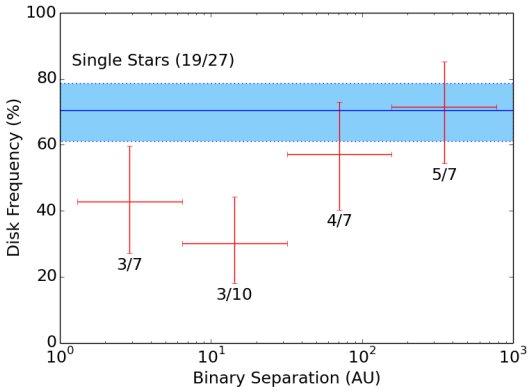

Figure 5.6: The fraction of observed binary stars that host disks as a function of the separation between the host star and the binary companion.

that of Kraus et al. (2012), who found that only $\sim 1/3$ of stars with companions at separations smaller than 40 AU hosted disks at ages of only 1-2 Myr. At the 1-2 Myr age of Ophiuchus, we find a similar result.

At the age of our sample, stars with a wide companion (>40 AU) have a similar disk frequency as single stars ($69\pm12\%$ compared to $70\pm9\%$). This implies that the presence of a wide companion does not signicantly affect disk evolution at an age of $\sim$1-2 Myr.

The fraction of stars that host circumstellar disks at such young ages is of critical importance for the formation of giant planets. The core accretion mode of star formation (Pollack et al., 1996) requires several Myr to efficiently produce giant planets. Since only $\sim 1/3$ of close binary systems in star forming regions still possess disks at an age of only 1-2 Myr, this implies that giant planets around such systems would be rare. This supports early results from radial velocity and transit surveys (Desidera and Barbieri, 2007; Roell et al., 2012; Wang et al., 2014).

A significant population of our targets have SED gaps indicative of a transition disk. 13 transition disk candidates were identified by Cieza et al. (2010): WSB 12, SSTc2d J162506.9-235050, DoAr 25, DoAr 32, DoAr 33, WSB 63, SSTc2d J163355.6-244205, SSTc2d J162245.4-243124, WSB 38, EM* SR 9, SSTc2d J162944.3-244122, ROXs 42C and DoAr 21. In addition, 4 more stars have been identified as transition disks: EM* SR 24 S, Haro 1-16 (DoAr 44), EM* SR 21 and YLW 46 (Oph IRS 48) (Andrews et al., 2011; Geers et al., 2007).

Of these 17 targets, 4 have close companions and may be circumbinary rather than transitional (DoAr 21, ROXs 42C, SSTc2d J162944.3-244122, WSB 38). In addition, EM* SR 24 S, SSTc2d J162245.4-243124, EM* SR 9 and EM* SR 21 have companions at wider separations that are not likely to be the source of their disk gaps. However, the remaining 9 targets have no detected stellar or substellar companion.

Many scenarios have been proposed for the origin of the disk gaps in transition disks. The favoured scenario invokes dust clearing due to the presence of giant planets forming in the disk. However, for the majority of the transition disk candidates in our survey we find a lack of stellar or brown dwarf companions capable of causing such gaps. This lends weight to the giant planet

formation hypothesis, showing that most of these disks are not circumbinary in nature.

5.1.9 Conclusion

We have performed a multiplicity survey of the ρ Ophiuchus cloud complex, studying the occurrence rates of stellar and sub-stellar companions. This information was combined with knowledge of circumstellar disks among our targets from Spitzer to investigate how these properties relate. Our results point to several significant conclusions for the processes of star and giant planet formation.

1. We have identified 36 multiple systems, including 9 systems with 3 components. This gives a binarity fraction of $43\pm6\%$, intermediate between the results of similar star forming regions in Upper Scorpius (Kraus et al., 2008) and Tauris-Auriga (Kraus et al., 2011).

2. The observed distribution of companion masses is consistent with a flat mass ratio distribution when considering components with separations between 1.3-780 AU, while the separation distribution is consistent with a log-normal or log-flat distribution over the same range when considering companions with masses between 0.08-6.0 $M_{\odot}$. These results agree with previous surveys of star forming regions and the field.

3. The fraction of disk hosting stars depends strongly on the existence of a close ($\lesssim$40 AU) stellar-mass companion. Only $\sim$1/3 of stars in close binary systems still host circumstellar disks after only 1-2 Myr, suggesting that the presence of such companions significantly speeds up the process of disk dispersal or inhibits their formation. The lack of disks around close binary systems suggests that giant planets formed by the slow process of core accretion should be rare around such systems, a prediction supported by the results of early RV and transit surveys.

4. In contrast, a more widely separated companion appears to have no effect on the presence of a disk at 1-2 Myr. We find that $\sim 80\%$ of both single stars and wide binaries retain their circumstellar disks at the age of Ophiuchus members.

Chapter 6

Non Redundant Masking with the Gemini Planet Imager

The following chapter relates to the Gemini Planet Imager (GPI) instrument, specifically the commissioning and first results from the NRM mode. The instrument was designed and built by a large collaboration of US and Canadian researchers (the "GPI team"). The aperture mask installed on GPI was designed by Barnaby Norris and Peter Tuthill, and installed by members of the GPI team. The task of commissioning the NRM mode was shared between myself and Alexandra Greenbaum, both under the supervision of Peter Tuthill and Anand Sivaramakrishnan (the GPI NRM lead). Observations were carried out by the GPI team, myself and Alexandra. I conducted all of the data analysis reported here, although the same data were processed separately by Alexandra using an independent analysis pipeline to verify results. The post-cube extraction data pipeline used in this work was based on the Sydney aperture masking pipeline, but with very signifcant modifications and expansion in scope implemented by myself so as to accept and process GPI NRM data. Planning of observations and discussion of results were shared between myself and Alexandra with input and supervision by Peter and Anand.

6.1 The Gemini Planet Imager

The Gemini Planet Imager (GPI) is a dedicated instrument developed for the purpose of direct imaging of exoplanets. This is accomplished through the use of an Extreme Adaptive Optics (ExAO) system that offers a level of wavefront correction significantly better than of previous generation AO systems (Macintosh et al., 2008b). By providing a highly stable and well corrected PSF, GPI allows much better calibration of systematic errors that make it difficult to directly detect exoplanets.

Several competing instruments have also been developed for this purpose, including the Spectro-Polarimetric High contrast Exoplanet REsearch instrument (SPHERE) (Beuzit et al., 2008) and the Subaru Coronagraphic Extreme AO instrument (SCExAO) (Martinache and Guyon, 2009).

The primary operational mode of GPI involves an Apodized Pupil Lyot Coronograph (Aime et al., 2002; Soummer et al., 2003), a system combining an opaque occulting spot and Lyot stop with an apodizing plate. This technique relies on changing the PSF shape to maximise the amount of on-axis starlight blocked by the coronagraph while allowing the faint light from nearby exoplanets to pass through unimpeded.

The performance of previous generation AO systems was limited by the presence of quasi-static speckles caused by uncorrected or non-common path wavefront errors (Soummer et al., 2007) and GPI was designed to attack this problem in several ways. The ExAO system leads to less uncorrected wavefront error, and the resulting highly stable PSF allows better calibration when using PSF subtraction algorithms and Angular Differential Imaging (ADI Schneider and Silverstone, 2003; Marois et al., 2006).

GPI also contains a low spectral resolution (R$\sim 35-80$) Integral Field Unit (IFU), resulting in simultaneous images across what are effectively 17 independent wavelength channels. This was motivated by the use of advanced differential imaging techniques such as Simultaneous Differential Imaging (SDI Marois et al., 2000), and the ability to provide spectral characterisation of detected objects. Since the size of the PSF and hence the angular positions of the quasi-static speckles depends on wavelength, comparison of images at different wavelengths allows image artefacts to be identified and removed while preserving stationary structures inherent to the observed object (such as an exoplanet).

The high level of wavefront control provided by the GPI ExAO system also allows a smaller coronagraph spot and hence a smaller inner-working angle than previous instruments. Reducing the coronagraph spot size is a huge advantage, since the majority of exoplanets reside close to their parent star. At the median distance of the targets in the GPI campaign target list (40 pc), the GPI H-band coronagraph blocks the inner 5 AU of each target. High contrasts are difficult to achieve close to the coronagraph edge due to leakage of light around the occulting spot, and so the effective inner working angle is signficantly larger. At a distance of 40 pc, a bright exoplanet would need to be at a larger orbital radius than Jupiter to be detectable with the GPI coronagraph.

In addition to an IFU, GPI also contains an imaging polarimetry mode, allowing faint polarized structure around stars to be investigated. The addition of a polarimeter is primarily motivated by the study of circumstellar material around young stars, such as debris disks. The GPI polarimetry mode utilises a novel technique referred to as "Integral Field Polarimetry" (Perrin et al., 2015). Conventional polarimeter designs use a Wollaston prism to separate light of different polarizations then focus the two beams using a lens onto a detector, introducing large non-common path errors between the two channels. In contrast, the GPI polarimeter uses a Wollaston prism after the same microlens array used for the IFU, producing much less differential wavefront error between the channels (Perrin et al., 2015).

6.2 GPI-NRM

As part of GPI's baseline design, a non-redundant aperture mask was included to explore complementary search space to the default coronagraph mode (Sivaramakrishnan et al., 2010). NRM provides access to angular regimes inside the region blocked by the GPI coronagraph, at contrasts unachievable through conventional imaging.

The interferometric field of view of NRM is set by the shortest baseline. For GPI, the shortest baseline of 0.97 m provides some overlap with the range of angles accessible through coronagraphy. The key advantage of NRM, however, is the ability to access angular scales down to 0.5 λ/D, with a relatively flat contrast curve outside of λ/D. For GPI-NRM, the minimum angular scale varies between 16–36 mas depending on the observing band (0.95–2.4 μm).

While NRM has been used extensively in previous generation instruments for faint companion searches at or close to the diffraction limit, the combination of NRM on GPI offers many advantages and unique opportunities. The PSF stability and wavefront control provided by the GPI ExAO system allows much higher contrasts to be reached than have previously been attainable with NRM. Previously, these searches have been mostly limited to the brown dwarf mass regime, but GPI NRM will allow routine detections into the giant planet regime.

The GPI IFU also allows access to a new range of wavelength differential quantities – such as wavelength differential closure phase – that have the potential to provide a higher degree of calibration and even higher contrasts, as well as allowing investigation of structure that varies with wavelength.

NRM can also be used with the GPI polarimeter mode, where calibrating visibilities and closure phases from orthogonal polarizations provides a further level of calibration. This has been demonstrated on previous generation instruments for the study of polarized dust around massive evolved stars (Norris et al., 2012). The higher precision measurements provided by GPI allow for the study of fainter polarized structure, such as the circumstellar disks of young stars.

6.2.1 The Non-Redundant Mask

The GPI NRM provides a reasonable tradeoff between throughput and Fourier coverage while maintaining strict non-redundancy, even with the large GPI filter bandwidths in polarized mode. The final design was a 10 hole mask, a photo of which is shown in Figure 6.1. A composite of images taken with the pupil viewing camera is also given, showing the mask holes in green, orange and red. The telescope spiders are shown in dark blue, as well as several broken deformable mirror actuators that are masked off during regular observations. The mask was designed to avoid these regions.

The positions of the mask holes projected onto the Gemini pupil are given in Table 6.1. A gap between the edge of the Gemini pupil and the mask holes helps to mitigate problems with pupil alignment. This has the added advantage of making the NRM PSF Nyquist sampled in all GPI filters, since 8 m baselines are not Nyquist sampled in other observing modes in Y band. Each hole has a diameter of 0.66 m when projected onto the primary mirror.

An example PSF with the aperture mask is shown in Figure 6.2. This image was taken on the star HD 63852 in March 2014 in H band. The corresponding power spectrum is also presented, showing the Fourier coverage provided by the mask.

6.2.2 Observing and Exposure Times

The throughput of the 10-hole mask is about 6.5% of the unobstructed pupil, and the light from a point source is spread over a much larger diffraction pattern. Taking these effects into account, the peak flux for the NRM PSF is approximately 225 times less than the peak of the unocculted PSF in the same mode. Since the range of observable visible magnitudes is set by the wavefront sensor (which receives unocculted light) the I band range of 1–9 mag also applies to NRM mode. However, due to the attenuation of the mask, targets 5.8 mag brighter than the direct mode limit of $\sim$8 mag across Y–K bands may be observed without saturating the detector. A minimum exposure time of 1.45 seconds is available for GPI.

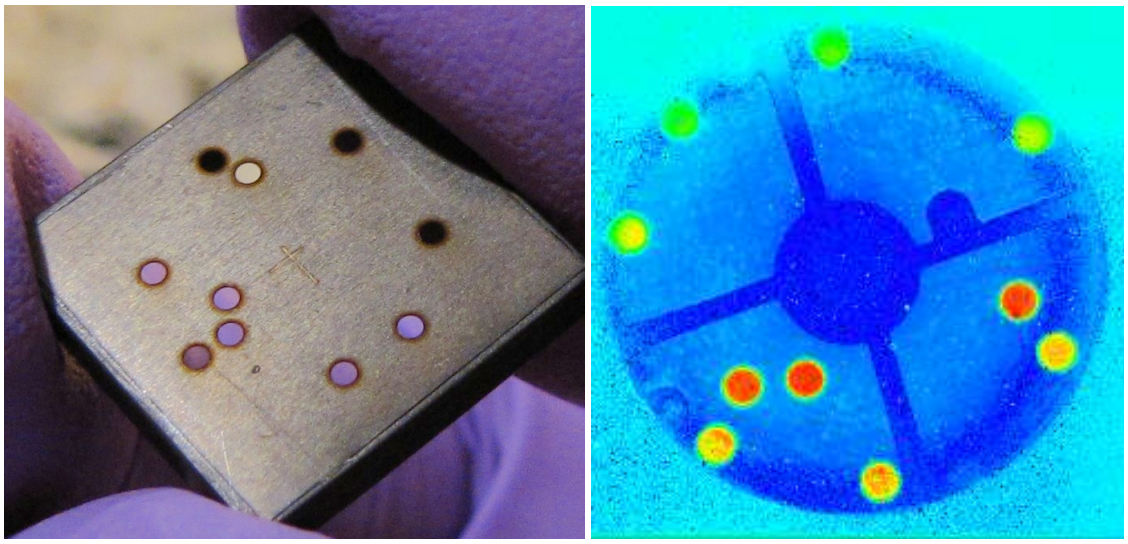

Figure 6.1: *Left:* A photo of the GPI NRM.
Right: A composite of images from the GPI pupil viewing camera. Images of the GPI pupil with the aperture mask and with the Lyot stop were combined to show the location of the NRM holes with respect to the GPI pupil, spiders and bad actuators.

Table 6.1: GPI NRM hole positions as projected onto the primary mirror, measured with respect to the centre of the mirror.

X (m)	Y (m)
2.05	-1.65
3.01	-1.60
0.884	1.62
0.353	2.43
-2.76	-1.94
-3.39	0.529
0.223	-3.43
2.81	1.74
0.786	3.29
-2.53	2.25

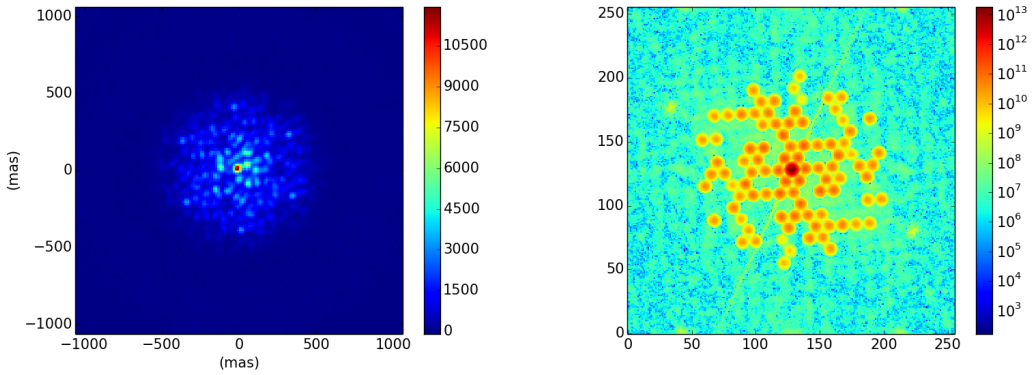

Figure 6.2: *Left:* The observed NRM PSF in H band, taken in March 2014 on the point source HD 63852.
Right: The resulting power spectrum, showing the Fourier coverage of the GPI aperture mask.

The combined bandwidth of one GPI IFU cube is similar to broadband filters of previous generation AO fed infrared cameras (e.g. NIRC2, NACO). Since the light is instead split over 17 independent spectral channels, much longer exposures are required. This results in observing blocks that take substantially longer than with previous instruments and introduces a new problem: the sky rotation during a sequence of frames leads to the signal produced by a faint companion or resolved structure changing systematically over time. The usual approach to processing NRM data involves dividing the data into blocks, from which the mean and standard error of each observing quantity is extracted and a single sky rotation is assigned. For GPI, this scheme was modified to instead measure the standard deviation of each observing quantity over each block, and preserve the unaveraged quantities and sky rotations of each frame for analysis. This alternative method is more resilient to sky rotation, but is more sensitive to outlying measurements. The measured uncertainties are also likely to be slightly overestimated, since systematic changes are treated as stochastic.

6.3 Processing GPI NRM Data

At present, the current method for processing GPI NRM data involves first using the GPI data reduction pipeline (Perrin et al., 2014) to extract calibrated data cubes from the raw data, both for polarimetry and spectral modes. This includes background subtraction, bad pixel identification and flat fielding. The GPI pipeline treats NRM data in the same way as data taken in other modes.

To extract the relevant quantities from the NRM data cubes, two pipelines currently exist: one developed in Baltimore that relies on fringe fitting to the images, and the Sydney aperture masking pipeline. In the Sydney pipeline GPI NRM data is treated in a similar way to data from previous instruments (Tuthill et al., 2000; Ireland et al., 2008; Tuthill et al., 2010), with the closure phases and visibilities measured from each wavelength channel individually and treated as independent

measurements.

For polarimetry mode, an additional program was developed to calculate polarized differential quantities. A general overview of this method is given in Norris et al. (2012). Due to the high level of wavefront correction, GPI presents an opportunity to use polarized differential phase as an additional robust observable to complement the polarized differential visibilities and closure phases used in previous work.

Polarized differential quantities are constructed with a double differential approach. This consists of calibrating observed quantities first with those quantities from the opposite Wollaston channel, then with those taken with the half-wave plate rotated by an extra 45°.

The square visibilities $V^2_{i,j}$ measured with the half wave plate rotated by $i°$ and from Wollaston channel j are combined to give polarized differential visibilities by the following equations:

$$V_Q = \sqrt[4]{\frac{V^2_{0,0}}{V^2_{0,1}} \div \frac{V^2_{45,0}}{V^2_{45,1}}} \tag{6.1}$$

$$V_U = \sqrt[4]{\frac{V^2_{22.5,0}}{V^2_{22.5,1}} \div \frac{V^2_{67.5,0}}{V^2_{67.5,1}}} \tag{6.2}$$

Similarly, polarized differential phases (or closure phases) can be constructed from the phases (closure phases) $P_{i,j}$ by the following equations:

$$P_Q = (P_{0,0} - P_{0,1}) - (P_{45,0} - P_{45,1}) \tag{6.3}$$

$$P_U = (P_{22.5,0} - P_{22.5,1}) - (P_{67.5,0} - P_{67.5,1}) \tag{6.4}$$

The first differential step comparing quantities from different Wollaston channels removes any systematic processes affecting both channels. By rotating the half wave plate 45° from its initial position, the polarization of each channel is reversed. The second differential step then removes non-common path error between the two channels.

6.4 Commissioning Performance

In 2013 and 2014, several observing runs were carried out to commission GPI, and most instrument modes were successfully commissioned and opened to community proposals in 2014B. Several data sets were taken with the NRM mode, and the results of a further run in 2015 (not reported here) should complete the commissioning process. The current timescale has GPI NRM fully available for proposals in the 2016A semester. The results of the commissioning observations from 2013 and 2014 are presented in the following sections, and a summary of all observations is shown in Table 6.2.

6.4.1 Spectral Mode Performance

To measure the performance of GPI NRM in IFU mode, the star HR 2690 was observed in December 2013 in H band, along with two point source calibrator stars (HR 2716 and HR 2839). This target is a close binary system, with a separation $<$100 mas and a contrast ratio of $\sim$5:1.

Table 6.2: Summary of GPI NRM observations in 2013–2014.

Date	Observer	Targets Observed	Mode	Target Description	Purpose
Nov 2013	GPI Team	HD 31996	Y, J, H spec	Carbon star	AO system tests
Dec 2013	GPI Team	HR 2690	H spec	Binary star	Test measurement precision
		HR 2716	H spec	Point source	Calibrator
		HR 2839	H spec	Point source	Calibrator
Mar 2014	A. Cheetham	VY CMa	Y, H spec	Resolved object	Test imaging capability, measurement precision, mask alignment and orientation
		HD 63852	Y, H spec	Point source	Calibrator
		HR 6494	J pol	Point source	Test polarization mode
		HIP 75230	H spec	Point source	Test long exposure stability
May 2014	A. Greenbaum	HD 142527	J spec	Faint companion	Test measurement precision
		HD 142384	J spec	Point source	Calibrator
		HD 142695	J spec	Point source	Calibrator
		HD 142384	H pol	Point source	Test measurement precision
		HD 142527	H pol	Possible structure	Test measurement precision

Fitting a grey binary model to the data produced the best fit parameters given in Table 6.3. The uncertainties given include the systematic uncertainties in both the plate scale and orientation from Konopacky et al. (2014). HR 2690 does not have a published orbit, but does have two published measurements of the secondary component, also shown in the table.

The observed separation of the companion is similar to previous measurements, but the change in position angle between the GPI observations and those from the literature is much larger than can be plausibly explained with orbital motion. However, re-analysis of archival 2005 AO-assisted K band NACO observations of HR 2690 (originally reported in Oudmaijer and Parr, 2010) shows a binary at a position angle of $\sim$180°, consistent with the GPI observations. The detections reported in the literature were based on speckle interferometry, a technique that can suffer a 180°ambiguity in measured position angles, and so it is likely that this is the cause of the disagreement between measurements. Another possibility is that the secondary component could host a bright gaseous disk that contributes significant infrared excess, causing the secondary to appear brighter in infrared wavelengths and causing the position angle to change by 180°. The HR 2690 system has a combined spectral type consistent with a Be star (Slettebak, 1982), suggesting that at least one component hosts a disk.

There is some discrepancy between the observed contrast ratios of HR 2690 reported in the literature, as shown in Table 6.3. However, it is difficult to examine the extent of the mismatch given the lack of uncertainties provided for the measured contrasts. Our infrared observations do not help to resolve this discrepancy.

In H band, the average calibrated closure phase uncertainty using the Sydney IDL pipeline from 8 frames is around 1 degree. Several improvements to the AO system after this measurement have resulted in a more recent figure of 1.2 degrees in J band during poor weather. The performance of NRM is typically better at longer wavelengths, so the closure phase uncertainty in H band is expected to be less than 1 degree at present. It should be noted that these values appear to be largely independent of exposure time and visible magnitude of the star in the ranges tested so far (1.5 - 60 seconds, 5.5-9 magnitudes).

While this level of closure phase stability is typical of that achieved with Keck NIRC2, the simultaneous measurement across a range of wavelengths provides a huge increase in the achievable contrast. The resulting detection limits are shown in Figure 6.3, showing that with just 8 exposures, a contrast of more than 6 magnitudes was reached at separations as small as 40 mas. This compares favourably to the typical contrast limit of 5 magnitudes attained with NRM using the NIRC2 instrument on the larger Keck II telescope from 24 exposures (e.g. Kraus et al., 2008, 2011).

6.4.2 Polarization Mode Performance

To measure the performance of GPI NRM in polarized mode, the stars HD 142527 and HD 142384 were observed in May 2014 under poor seeing. HD 142384 was used as a calibrator star to give an estimate of the residual signals after calibration, due to the expectation that it has no resolved polarized structure. The observations for HD 142527 are reported in Section 6.5. 8 frames were obtained in each of the 4 half-wave plate rotation angles (0°, 22°, 45°, 67°) for each

Table 6.3: Results of HR 2690 H band binary 3 parameter fit to the separation (rho), position angle (θ) and contrast ratio (C) assuming a flat contrast spectrum.

Year	Band	ρ [mas]	θ [°]	C	Ref.
1996	V	42	340	6 ± 4	Mason et al. (1997)
2010	V	91	7.8	20	Hartkopf et al. (2012)
2012	V	88.8 ± 1.3	11.1 ± 0.7	6	Tokovinin et al. (2014)
2013	H	88.6 ± 0.3	193.2 ± 1.2	5.76 ± 0.03	This work

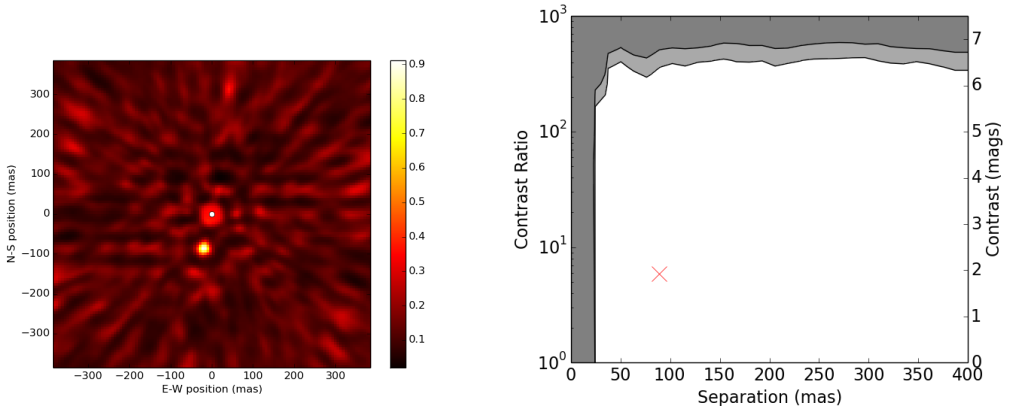

Figure 6.3: *Left*: The likelihood map for the binary HR 2690 at a fixed contrast ratio of 5.8:1. *Right*: The calculated detection limits. The white region indicates combinations of separation and contrast for which a companion would have been detected according to our 99.9% confidence limit, the light grey region marks the region of 99% confidence, and the dark grey region shows companions that would have fallen below 99% confidence. The contrast and separation of the detected companion are shown with a red cross.

target[1]. From the total of 32 frames taken on HD 142384, 8 were discarded due to loss of lock or poor performance by the AO system and the remaining frames had very low visibility at the long baselines.

The closure phases, square visibilities and raw phases were calculated from each image and turned into polarized differential quantities using the double differential approach described above. When calculated in this way, resolved polarized structure manifests as a change in differential visibility as a function of azimuth. The strength of the effect also changes with baseline length. The observed differential visibilities for the calibrator star are plotted as a function of azimuth and colour coded by baseline length in Figure 6.4. Despite the large uncertainties on long baselines, no evidence of a signal is seen.

To show how the accuracy of each measurement varies as a function of baseline, the median uncertainty for a range of baseline lengths is plotted in Figure 6.5, for both calibrator and target star. The uncertainties for the calibrator are significantly larger at longer baselines due to the rapidly degrading conditions during its observation, which led to poor AO performance and noisier visibilities on long baselines. For this reason, the results for HD 142527 are considered more indicative of future performance and we concentrate on those.

For baselines shorter than 4 m, the median uncertainty on the differential visibilities was essentially constant, ranging between 0.2–0.3%. At longer baselines, the median uncertainties increased before plateauing at 1%. These values show the performance of GPI NRM polarimetry is significantly better than the 2–3% uncertainties seen with NRM on NACO (in so-called "SAMPol" mode) (Norris et al., 2012). The measured performance approaches that of the dedicated aperture masking polarimeter VAMPIRES deployed on SCExAO, which typically obtains a visibility scatter of 0.4% combined over baselines up to 7.2 m by employing a triple differential approach (Norris et al., 2015).

The level to which uncorrected systematics affect the differential quantities can be estimated from the reduced χ^2 of the data. For HD 142384, the calculated values were $\chi^2_V = 1.6$, $\chi^2_{cp} = 0.97$ and $\chi^2_\phi = 3.7$ for the differential visibilities, closure phases and phases respectively. This suggests that the visibility and phase uncertainties may be underestimated or that there may be underlying structure detected. Following our observations of HD 142384 a faint close companion was discovered, that may be responsible for some of the observed residual signals (Le Bouquin, 2014). Further measurements of calibrator stars in 2015 are expected to characterise the residual systematic noise more thoroughly.

[1]Typically, observations use half-wave plate rotations of 0°, 22.5°, 45°, 67.5°, but a software issue in early 2014 prevented non-integer rotations. This has now been fixed and future observations should use the standard rotation angles.

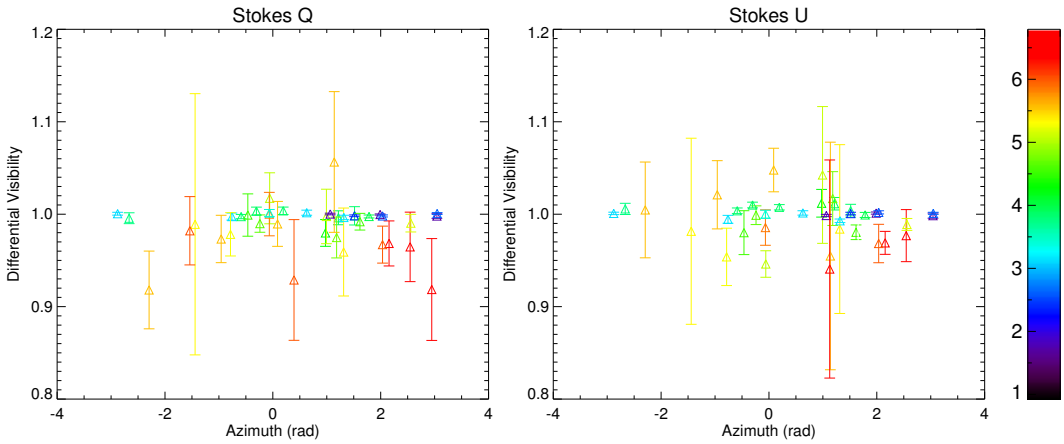

Figure 6.4: The observed polarized differential visibility amplitude plotted as a function of baseline azimuth for the calibrator star HD 142384. The colours identify the baseline lengths. Ten measurements with uncertainties larger than the plotted range (but consistent with 1.) have been ommitted for clarity.

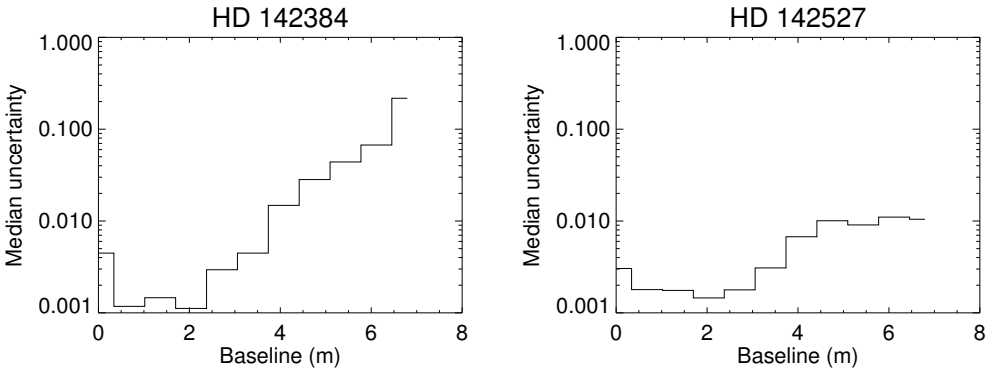

Figure 6.5: The calculated uncertainties for the polarized differential visibilities plotted as a function of baseline length for both HD 142384 (Left panel; a calibrator) and HD 142527 (Right panel; a target with possible resolved polarized structure, reported below).

6.5 GPI NRM Observations of HD 142527B, a circumbinary transition disk

6.5.1 Introduction

HD 142527 is a young (5 Myr), intermediate mass ($2M_{\odot}$) star associated with the nearby Upper Centaurus Lupus star forming region (Teixeira et al., 2000), suggesting it has a distance of 140 pc. Its mass and spectral type places it on the boundary between Herbig Ae/Be and T Tauri stars, often called Herbig Fe objects. Through study of its SED, it was identified as a transition disk- an object midway through the transition between the protoplanetary and debris disk stages.

Transition disks contain characteristic disk gaps that consist of an optically thin region around the star surrounded by an optically thick outer disk. Several hypotheses have been proposed for the origin of these inner opacity holes, including grain growth (Dullemond and Dominik, 2005) and photoevaporation (Alexander and Armitage, 2007). However, one of the leading candidates is the formation of a companion within the disk that sweeps up material, such as a binary star or giant planet (e.g. Ireland and Kraus, 2008; Kraus and Ireland, 2012).

Several companion candidates have been observed in transition disk gaps. Non-redundant aperture masking has been particularly successful in this endeavour, and was used to detect companion candidates to LkCa 15 (Kraus and Ireland, 2012), FL Cha (Cieza et al., 2013) and HD 142527 (Biller et al., 2012). However, some caution needs to be taken in interpreting such data, as an inclined outer disk can produce a similar signal to a substellar companion (Olofsson et al., 2013).

HD 142527 is a particularly interesting system with an angular separation large enough to allow it to be studied with full-pupil imaging in conjunction with ADI techniques (~ 80 mas) (Close et al., 2014; Rodigas et al., 2014). This has allowed measurement of the Hα luminosity of the companion, leading to an estimate of its mass accretion rate of $\dot{M}_{\rm companion} = 5.9 \times 10^{-10} M_{\odot} {\rm yr}^{-1}$ (Close et al., 2014). The companion mass has been estimated at $0.25 M_{\odot}$ (Biller et al., 2012), meaning it is most likely a low mass stellar companion rather than of planetary nature.

Recent ALMA observations have suggested an inclination of 28 ± 0.5 deg for the disk and a position angle of $\sim$70 deg (Perez et al., 2015). Assuming the orbit of the secondary component is coplanar with the disk, the observed companion separation corresponds to ~ 12 AU. Circumbinary disks are expected to be truncated at their inner edges with radii of ~ 2 times the binary semi-major axis (Artymowicz and Lubow, 1994). If the disk around HD 142527 was purely circumbinary, we would expect the inner radius of the outer disk to be approximately 24 AU. However, observations have shown a much larger radius of 90 ± 5 AU (Perez et al., 2015). It is therefore expected that another explanation for the large cavity is needed, with ongoing planet formation being a strong candidate.

Constraining the orbit and properties of the companion (HD 142527B) is crucial to understand this peculiar system which represents a unique laboratory for studying planet formation in situ.

6.5.2 Observations and Data Reduction

HD 142527 was observed in May 2014 in spectrally-dispersed J band and polarized H band. Two calibrator stars were also observed (HD 142695 and HD 142384) in spectral mode, and one in

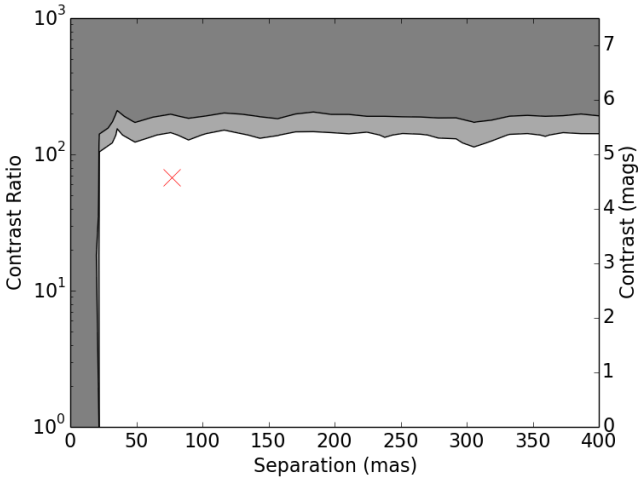

Figure 6.6: The point source detection limits for HD 142527. The contrast and separation of the detected companion is marked with a red cross. A contrast of more than 5 magnitudes was achieved at separations greater than 30 mas.

polarized mode (HD 142384). These observations were conducted in poor conditions, and the AO system was unable to correct for the atmosphere in several frames.

The spectral data were cleaned and turned into data cubes using the GPI pipeline, and the resulting cubes were processed and calibrated using the Sydney IDL aperture masking pipeline. The resulting data products were saved into the OIFITS standard format. A custom Python module designed for the analysis of OIFITS files was used to analyse the results and perform model fits using two numerical optimizers: the nested sampling implementation MULTINEST (Feroz et al., 2009; Feroz and Hobson, 2008; Feroz et al., 2013) and the MCMC algorithm emcee (Foreman-Mackey et al., 2013).

6.5.3 Results

HD 142527B was extracted at high significance and well above the calculated detection limits, shown in Figure 6.6. The final marginalised posterior distributions are shown in Figure 6.7, yielding a separation of 77.0 ± 0.6 mas, position angle of 116.8 ± 0.6 deg and contrast ratio of 67.4 ± 2.5 by assuming a constant contrast ratio with wavelength across the GPI J band spectral range. These observations represent the highest precision astrometry of HD 142527B to date by a factor of 2. Clear evidence of orbital motion is seen between observations.

The spectral resolution of GPI makes it possible for strong spectral features to be identified. Strong Hα emission has been previously detected from HD 142527B at $3\times$ the continuum flux (Close et al., 2014). This data allows us to search for corresponding Paβ emission at 1.28μm, which falls within our wavelength range. However, the spectral resolution of GPI at J band is $\sim$ 37 (i.e. 35 nm at 1.2 μm) compared to the 6 nm filter width used in the discovery of its Hα

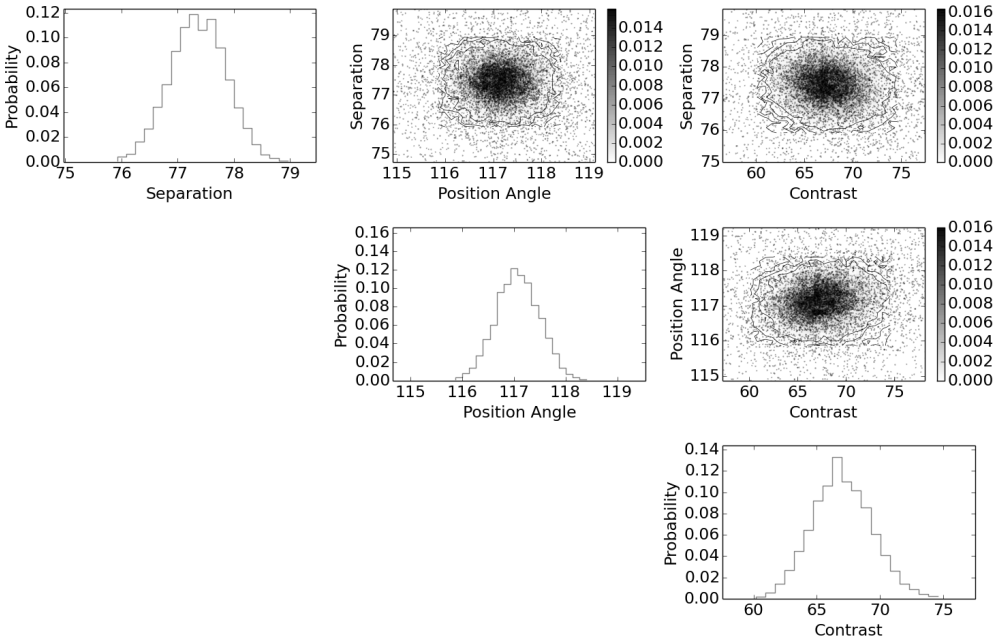

Figure 6.7: The marginalised 1D and 2D posteriors for the separation, position angle and contrast of HD 142527B.

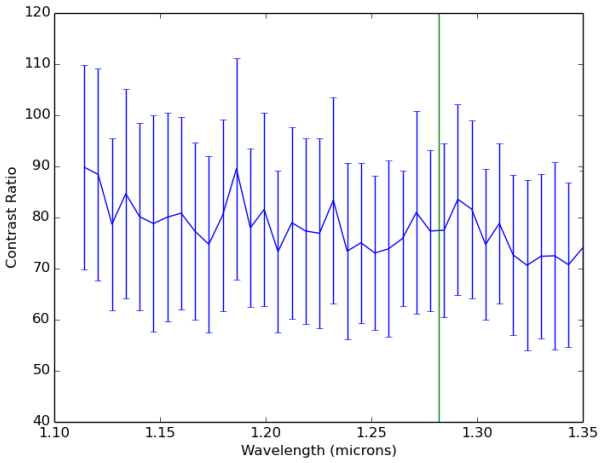

Figure 6.8: The measured contrast ratio of HD 142527 as a function of wavelength, assuming a fixed separation of 77 mas and position angle of 117 deg. The location of the Paβ line is shown in green. Strong emission from the secondary would lead to a decrease in the contrast ratio, but we find no evidence of any change in contrast ratio across the line. The spectrum shows 37 individual data points, however neighbours are not independent and this represents interpolation over approximately 17 independent wavelength channels.

emission, making detections of such lines difficult. By fixing the separation and position angle of the secondary and fitting to the contrast ratio as a function of wavelength, we are able to get an estimate of the differential spectrum of the two components.

The resulting differential spectrum is shown in Figure 6.8. Paβ emission from the secondary component should show up as a decrease in the contrast ratio, which is not observed. We find the flux in the wavelength channel encompassing the emission line to be the same (within a multiplicative factor 1.0 ± 0.4) as the continuum flux estimated from the neighbouring wavelength channels. A signal with a similar strength to that seen in Hα would show up as a 35% change in flux when observed with the spectral resolution of our data, which is below the precision of our measurement.

The observed differential visibilities from polarized mode are shown in Figure 6.9. The data show a higher degree of precision than the observed calibrator star from Section 6.4.2, and appear to vary with azimuth, suggesting the detection of a polarized signal. Typical signals produced by polarized circumstellar structures show a similar variation, such as those seen for resolved dust shells around red giant stars in Norris et al. (2012). However, due to the lack of a confident non-detection of polarized structure on a calibrator star with a similar or greater level of precision, it is difficult to estimate the degree to which systematic errors affect the data. Without further information to constrain the contribution from systematic errors, we cannot conclusively determine the origin of the observed differential visibility signal.

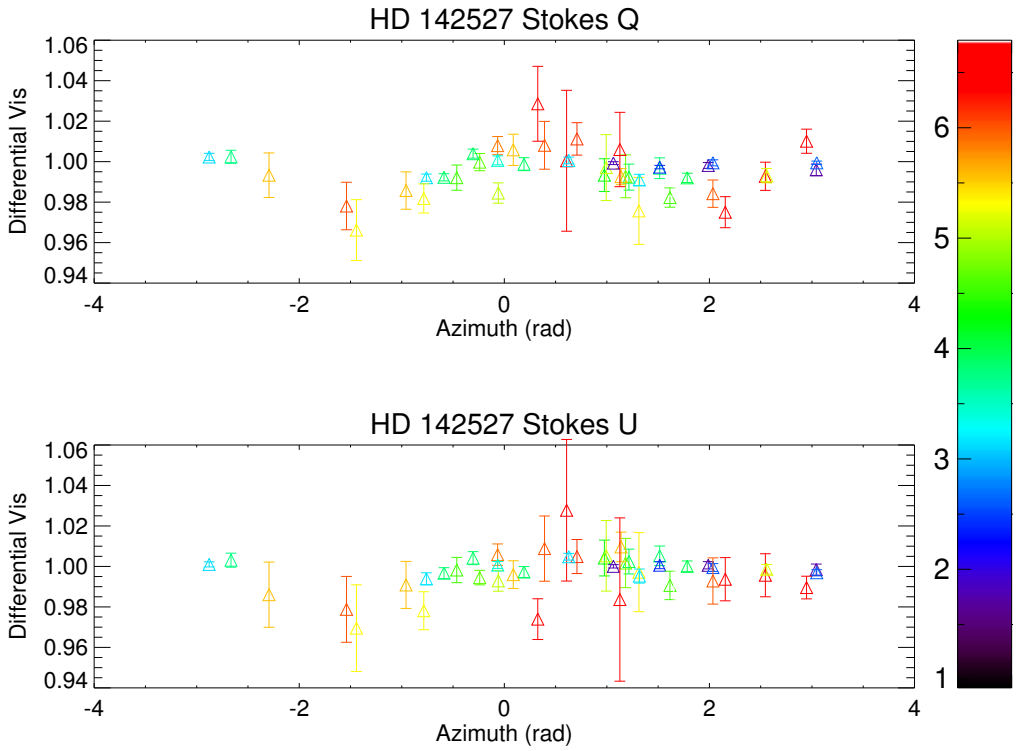

Figure 6.9: The observed polarized differential visibility amplitudes for HD 142527, plotted as a function of baseline azimuth. The colours identify the baseline lengths.

6.5.4 Conclusion

We have recovered the HD 142527 companion at high significance, demonstrating the capability of GPI NRM to detect high contrast companions. These observations have provided the most precise measurement of the position of this companion to date, and is crucial in determining a precise orbital fit both now (e.g. Lacour et al., 2015, in prep.) and as more orbital coverage is attained. The spectrally dispersed nature of our observations also allowed us to search for Paβ emission from the companion, which was not detected.

Finally, a tentative polarized differential visibility signal was found, which may indicate the presence of faint resolved polarized structure. However, further calibration observations are needed to confirm that this signal is not caused by uncorrected systematics.

6.6 GPI NRM Observations of VY CMa: Imaging the winds of a mass-losing supergiant

6.6.1 Introduction

VY CMa is a red supergiant star of spectral type M2.5–M5e Ia (Houk and Smith-Moore, 1988), and one of the most luminous stars in the galaxy. It has an extremely high rate of mass loss ($3 \times 10^{-4} \mathrm{M}_{\odot} \mathrm{yr}^{-1}$ (Danchi et al., 1994)), that has led to the suggestion that it will explode as a supernova in $\sim 10^5$ years. Despite its distance of 1.1-1.25 kpc, large ejected clumps of warm dust have been spatially resolved on scales across a range of angular scales and wavelengths (Monnier et al., 1999; O'Gorman et al., 2015; Richter et al., 2013; Alcolea et al., 2013). Due to its known morphology and bright structure on angular scales relevant for NRM, VY CMa is a perfect candidate for testing the imaging capabilities of GPI NRM.

6.6.2 Observations and Data Analysis

VY CMa was observed with GPI NRM in H band in March 2014 in excellent conditions, along with the point source calibrator star HD 63852. Observations were conducted using GPI's spectrally-dispersed mode with a total exposure time of 30 s.

The data were processed using the method described in Section 6.3, and turned into calibrated OIFITS files. Image reconstruction was then performed on the data using the MACIM package (Ireland et al., 2008).

6.6.3 Results

The calibrated visibilities (V) are shown in Figure 6.10. A significant drop in V^2 was observed at baselines as short as 2 m, indicative of bright well-resolved structure. The visibilities in the N-S and E-W directions also displayed significant differences and a large closure phase signal was observed, showing strong asymmetries in the observed structure.

The reconstructed image of VY CMa in H band is seen in Figure 6.11. This image was generated using the assumption that the brightness of any structure is constant across the range

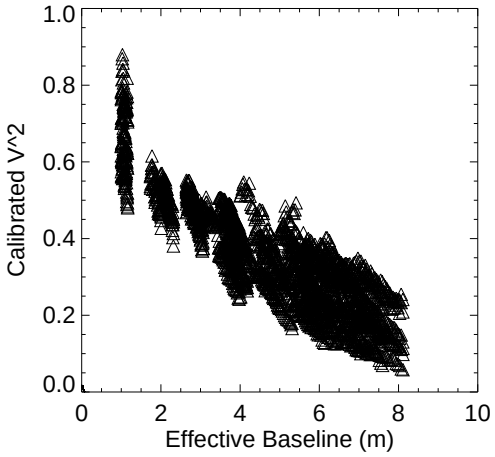

Figure 6.10: The observed calibrated V^2 as a function of baseline. The drop in V^2 at longer baselines indicates sigificant resolved structure.

of wavelengths of GPI. Large amounts of structure are seen, tracing clumps of material in the mass-loss envelope of this star.

VY CMa has been observed regularly with NRM on older instruments since 1997. The previous most recent image of VY CMa, taken with the NACO instrument, is also shown in Figure 6.11 for reference. Comparison with previous images allows us to verify the orientation and position angle information is being used correctly in processing the GPI NRM data. This also acts as a demonstration of the imaging capabilities of GPI NRM in spectral mode, showing that resolved structure can be reconstructed from observed data with the modest Fourier coverage of the GPI 10 hole aperture mask.

These observations increase the time baseline for NRM imaging of VY CMa to 17 years, allowing us to trace its mass losing history. By pinpointing visible structures and tracing their positions in subsequent images, it is possible to measure the projected velocities of individual clumps, giving an estimate of the speed of the VY CMa ejecta.

Applying this process to the GPI image and combining it with previous NRM images indicates wind velocities of ~ 10 km/sec, with variations between individual clumps of up to a factor of 2. Estimates from VLBA observations of maser emission from the circumstellar envelope suggest velocities of up to 8 km/sec (Zhang et al., 2012), in agreement with our result.

6.6.4 Conclusion

We have observed the cool red supergiant VY CMa with GPI NRM in spectral mode in H band, using model independent image reconstruction to produce an image from the observed closure phases and visibilities. The resulting image verifies that the orientation of the GPI aperture mask is being accounted for correctly in the Sydney aperture masking pipeline. Comparison with images produced in the same way using older instruments shows a confident detection of relatively

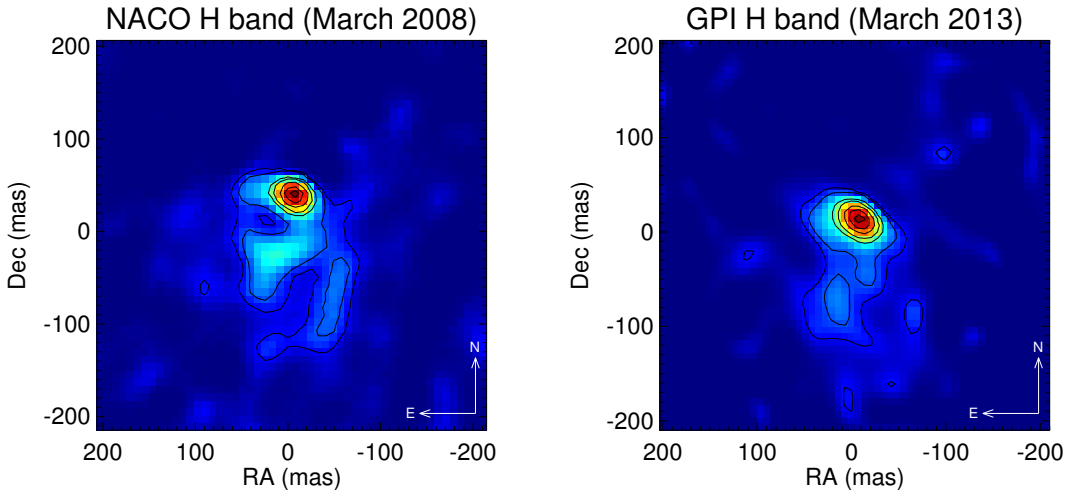

Figure 6.11: *Left:* A reconstructed H band image from NACO NRM data from March 2008, showing the complex structure of the ejected material. Contours show 0.5%,1%, 5%, 1%, 25%, 50% and 80% of the peak flux.
Right: The reconstructed image from the GPI NRM data with the same contours shown. The observed morphology of the ejected material shows the same general features, with a bright resolved structure South of the central star. Significant motion of the ejected material is also observed between epochs.

minor proper motion of source structure. From these images, the wind velocity was estimated at ~ 10 km/sec, in agreement with previous measurements from maser emission. While the GPI aperture mask was not designed to optimize its imaging capability, the high precision image generated shows that it is a useful tool for imaging resolved structure.

6.7 Future Work

A final commissioning run for the GPI NRM mode is planned for 2015, concentrating on measuring performance for the remaining combinations of filter with polarimetry and the IFU. The results of this observing run (which are not part of this dissertation) will be used in conjunction with the results presented here to fully characterise the overall performance and to guide future observations. This should allow GPI NRM to be offered to the community in time for the 2016A observing round.

As mentioned in Section 6.3, the current method for processing GPI NRM data uses the GPI data reduction pipeline. Any method for extracting datacubes from the raw data has the potential to introduce systematic noise. Incorporating this process into the aperture masking pipeline used to analyse the data would allow for easier characterisation of these effects, as well as the addition of possible NRM specific optimisations. This is particularly important for IFU mode, where the correlation between different wavelength channels is important to measure and minimize. Having a single pipeline for taking the data through from the raw data to the point of extracting measured quantities would simplify this process.

To date, the use of wavelength differential quantities has not been demonstrated with GPI. Typically, these quantities are constructed by comparing the measured visibilities and closure phases of images taken inside and outside of a spectral line, taking advantage of the large change in the expected signal as the observed target gets significantly brighter or fainter compared to the companion or circumstellar material being studied. The low spectral resolution of GPI makes this task difficult, since the width of any spectral line will be much smaller than the width of a wavelength channel, reducing the change in brightness. For GPI NRM, usage of wavelength differential quantities may be limited to companions with significantly different spectral types to their host star, targets with wide absorption bands or targets with extremely strong emission lines. A demonstration of this process may be possible on such a target in the future.

Chapter 7

The T Cha Transition Disk

7.1 Transition Disks

The star T Chameleontis was one of the first transition disks observed with Non Redundant Masking, and the presence of a large closure phase signal was initially interpreted as originating from a substellar companion located in the disk gap (Huélamo et al., 2011a). However, subsequent work combining multi-wavelength data on a range of angular scales cast some doubt on this claim, and suggested that the data could equally well be explained by forward scattered light from the inclined inner edge of the outer disk (Olofsson et al., 2013).

In the following paper, we investigate the nature of the T Cha companion candidate by analysing 3 years of NRM data in 2 wavelengths. A consistent closure phase signal is seen in each dataset, contradicting expectations for an orbiting body (for which signals are expected to vary) and confirming the most likely origin of the flux asymmetry as a circumstellar disk.

By performing model-independent image reconstruction of the NRM data and through thorough modelling of systematic effects introduced by this process, we provide further evidence that the closure phase data is more consistent with the disk model.

For this paper, I performed all data processing and analysis. I also provided the interpretation of the results, with consultation from Peter Tuthill. The observations were conducted by the co-authors, who also provided help with the models of the T Cha disk used in the paper. The paper was written by myself, and improved with comments from co-authors.

The following manuscript was published in Monthly Notices of the Royal Astronomical Society: Letters (2015) vol. 450, issue 1, L1. The version presented here has been modified slightly from the published version.

Near-IR imaging of T Cha: evidence for scattered-light disk structures at solar system scales

Anthony Cheetham,[1] Nuria Huélamo,[2] Sylvestre Lacour,[3] Itziar de Gregorio-Monsalvo[4,5] and Peter Tuthill[1]

[1]Sydney Institute for Astronomy, School of Physics, University of Sydney, NSW 2006, Australia
[2]Centro de Astrobiología (INTA-CSIC); ESAC Campus, P.O. Box 78, E-28691 Villanueva de la Cañada, Spain
[3]Observatoire de Paris, LESIA/CNRS UMR, 5 place Jules Janssen, Meudon, France
[4]Joint ALMA Observatory (JAO), Alonso de Cordova 3107, Vitacura, Santiago de Chile
[5]European Southern Observatory, Garching bei Munchen, D-85748 Germany

Abstract

T Chamaeleontis is a young star surrounded by a transitional disk, and a plausible candidate for ongoing planet formation. Recently, a substellar companion candidate was reported within the disk gap of this star. However, its existence remains controversial, with the counter-hypothesis that light from a high inclination disk may also be consistent with the observed data. The aim of this work is to investigate the origin of the observed closure phase signal to determine if it is best explained by a compact companion. We observed T Cha in the L' and K_s filters with sparse aperture masking, with 7 datasets covering a period of 3 years. A consistent closure phase signal is recovered in all L' and K_s datasets. Data were fit with a companion model and an inclined circumstellar disk model based on known disk parameters: both were shown to provide an adequate fit. However, the absence of expected relative motion for an orbiting body over the 3-year time baseline spanned by the observations rules out the companion model. Applying image reconstruction techniques to each dataset reveals a stationary structure consistent with forward scattering from the near edge of an inclined disk.

7.1.1 Introduction

Transitional disks represent an important phase in the evolution of circumstellar disks; a stepping stone between a gas rich protoplanetary disk and a rocky, gas poor debris disk.

The characteristic deficit of mid-IR emission that defines this class is explained by a lack of dust at intermediate distances from the central star, leading to the appearance of an annular gap in their disks. These holes or gaps can be created by dust clearing due to the presence of a planetary system, causing transition disks to be prime targets for young planetary systems in formation. However, alternative explanations exist, such as the presence of a close binary companion (e.g. CoKu Tau 4, Ireland and Kraus, 2008) or grain growth (Dullemond and Dominik, 2005).

In the last few years, several substellar companion candidates have been reported within the annular gaps of transition disks. Among these are T Cha, HD 142527 and LkCa 15 (Huélamo et al., 2011b; Biller et al., 2012; Kraus and Ireland, 2012), all based on the Sparse Aperture Masking (SAM) technique (Tuthill et al., 2006). In this paper, we investigate the nature of the companion candidate reported for T Cha.

T Cha is a G8 star at an estimated distance of 108 ± 9 pc (Torres et al., 2008). The star is surrounded by an inner disk (Olofsson et al., 2013) and an outer disk separated by a dust gap of $\sim$20 AU (Huélamo et al., 2015). The highly inclined nature of its outer disk has led to the

Table 7.1: Log of observations.

Date	Filter	Calibrators
2010-Mar-14	L'	HD 101251, HD 102260
2011-Mar-14	L'	HD 101251, HD 102260
2011-Mar-15	K_s	HD 101251, HD 102260
2012-Mar-08	L'	HD 101251, HD 102260
2013-Mar-25	L'	HD 101251, HD 102260
2013-Mar-26	K_s	HD 101251, HD 102260
2013-Mar-27	H	HD 101251, HD 102260

suggestion that forward scattering may produce closure phases similar to those expected from the reported companion candidate (Olofsson et al., 2013). To investigate this claim, we have obtained 4 epochs of SAM data for T Cha covering 3 years, to look for evidence of orbital motion that would reveal the nature of this object.

Several multiwavelength studies of the T Cha system have been performed, yielding precise constraints on the disk and stellar parameters (Cieza et al., 2011; Olofsson et al., 2011, 2013; Huélamo et al., 2015). Based on these constraints, we adopt a mass of $1.5\,M_{\odot}$, temperature of 5400 K and stellar radius of $1.4\,R_{\odot}$. The outer disk around T Cha has been recently imaged by ALMA (Huélamo et al., 2015), showing a gaseous disk larger than the dust disk. We adopt an inclination of 68°and a position angle (measured from North to East) of 118°, estimated from these spatially resolved observations.

7.1.2 Observations and data reduction

T Cha was observed with NAOS-CONICA (NACO), the AO system at the Very Large Telescope (VLT) using SAM in March 2011, March 2012 and March 2013. Observations were conducted with the L' and K_s filters, under good to moderate conditions. A summary of the observations is included in Table 7.1. We also include the observations from March 2010 previously reported in Huélamo et al. (2011b).

A 2013 dataset taken with the H filter was also analysed, but a combination of poor seeing and wind shake resulted in this data being dominated by noise and hence not useful for the purposes of this study.

All data were reduced and analysed using two independent aperture masking pipelines to check for consistent results. The first was developed in Sydney and uses a Fast Fourier Transform-based approach (Tuthill et al., 2000), while the second (SAMP) was developed in Paris and measures phase by fringe fitting to images (Lacour et al., 2011). Similar results were obtained regardless of the software employed, and so only the results from the Sydney reduction are presented in the following sections. Following established procedure (Lloyd et al., 2006), our analysis of circumstellar structure is reliant upon the robust closure phase observable (inclusion of the noisy visibility modulus adds little of significance). The resulting OIFITS files are available for download as supplementary material from the online journal.

Comparing the closure phase data from the two calibrators revealed no statistically significant

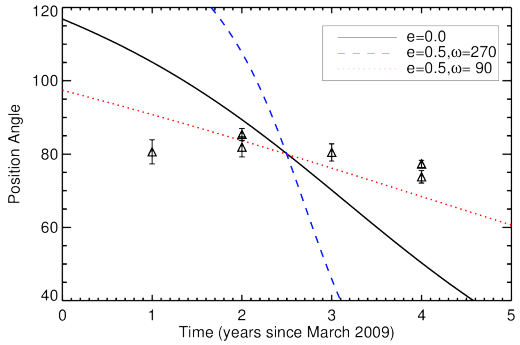

Figure 7.1: The measured position angles of the detected companion candidate plotted over several simulated orbits for an object in the plane of the disk. Shown are a circular orbit (black solid line), as well as moderately eccentric orbits (e=0.5) chosen to maximize (blue dashed line) and minimize (red dotted line) the expected change in position angle. Orbital motion expected from even a moderately eccentric orbit is clearly excluded by the observations, suggesting that the detected object is not consistent with a stellar or sub-stellar coplanar companion.

difference between them that would indicate the presence of a companion to either star in the range of angular scales explorable through SAM.

Lengthy data runs targeting individual objects, such as were taken for this project, give sufficient statistics to mitigate random noise introduced by uncorrected seeing. However the accuracy with which we are able to recover our primary closure phase observable can still reach an instrumental noise floor due to imperfections in the telescope and camera. The use of a PSF reference star dramatically reduces, but does not entirely eliminate, this noise. For our T Cha data, strong confidence that real signals arising from the target dominate over any residual systematic error is provided by the finding of identical results over a range of angular diversity. Features rotating at siderial rates as observations span large ranges of sky orientation would be overwhelmingly difficult to concoct by statistical fluke.

7.1.3 Results and Interpretation

7.1.4 Planet model

Calibrated closure phase data were fit with a two-component model representing the star and companion incorporating 3 free parameters (separation ρ, position angle θ and contrast ratio C). Model fits were obtained using the nested sampling implementation MULTINEST (Feroz et al., 2009). A uniform prior was used for position angle and separation, while a logarithmic prior was used for contrast ratio (translating to a uniform prior in units of magnitudes). This is expected to more closely match the actual distribution of companion flux ratios in the region of interest.

To check that the detections were robust, a 99.9% confidence test was applied. This consisted of a Monte Carlo simulation of 10,000 datasets drawn from a Gaussian distribution with zero mean and a standard deviation given by the measured uncertainties of each closure phase. By

Table 7.2: The resulting parameters from a single companion fit and a two companion fit to each dataset.

		Companion 1			Companion 2		
Epoch	Filter	ρ (mas)	θ (°)	C	ρ (mas)	θ (°)	C
2010	L'	64 ± 20	81 ± 3	217 ± 100			
		84 ± 12	87 ± 4	310 ± 40	128 ± 5	309.5 ± 1.5	390 ± 40
2011	L'	79 ± 13	82 ± 3	250 ± 80			
		74 ± 13	81 ± 3	340 ± 90	145 ± 9	310 ± 30	720 ± 180
2012	L'	45 ± 20	80 ± 3	81 ± 80			
		70 ± 12	90 ± 4	170 ± 60	88 ± 12	310 ± 5	300 ± 80
2013	L'	49 ± 10	77.3 ± 1.0	97 ± 50			
		72 ± 4	95.1 ± 1.9	95 ± 25	59 ± 7	291 ± 3	81 ± 30
2011	K_s	64 ± 2	85.4 ± 1.7	183 ± 16			
		66 ± 2	84.7 ± 1.5	175 ± 14	32 ± 8	349 ± 4	130 ± 70
2013	K_s	43 ± 6	73.8 ± 1.7	220 ± 40			
		54 ± 3	76 ± 2	270 ± 20	46 ± 6	321 ± 2	270 ± 50

fitting binary companions to each of these datasets, a distribution of parameters that are consistent with noise was constructed. To be considered real, a companion detected in the data must have a smaller contrast ratio than 99.9% of the simulated datasets with a similar separation.

Since the structures detected here are close to the resolution limit, there is a strong covariance between separation and contrast ratio. A bright companion at a small separation provides an equally good fit compared to a fainter companion at a wider separation. The uncertainties presented here represent the full marginal likelihood distributions and are much larger than uncertainties calculated at a fixed separation or contrast, such as those reported in Huélamo et al. (2011b).

The results of a single companion fit to each dataset are displayed in Table 7.2. The detection reported in Huélamo et al. (2011b) is reproduced in each dataset, although this re-analysis prefers a larger separation and higher contrast ratio consistent with the separation-contrast degeneracy expected at such small separations. The various datasets converge to different optimum combinations of separation and contrast, but all lie within the band consistent with this degeneracy.

Fits to all L' and K_s datasets produce a robust detection that satisfies the 99.9% criteria discussed above; the sole exception being March 2011 L' which gave a detection consistent with those from the other epochs, albeit at a lower signal-to-noise ratio.

Crucially, we find no evidence of orbital motion for the detected companion candidate. Assuming a circular, coplanar orbit, the measured angular separations correspond to deprojected separations between 12–21 AU and an orbital period in the range 35–78 years.

The location of the detected companion candidate places it close to the semi-minor axis of the inclined disk, both the location of maximum change in position angle and maximum uncertainty in physical separation. An example of typical orbits at the mean physical separation of 15 AU are shown in Figure 7.1. A position angle of 80°midway between the 2011 and 2012 epochs is assumed, which provides a good fit to the data. For a circular orbit, we expect 50°of change in

the position angle between our 4 detection epochs, which is clearly excluded by our observations. Orbits with moderate eccentricities also fail to reproduce the observed data, leaving only highly contrived solutions with high eccentricity and periapsis aligned to minimize observed orbital motion. The lack of orbital motion argues strongly against the interpretation of the detected object as a companion coplanar with the observed disk.

Quite apart from the absence of expected orbital motion, the single companion model does not fully explain the observed closure phases. In all datasets the final reduced χ^2 for the best fit binary parameters was substantially greater than 1, as shown in Table 7.3. This may indicate the presence of uncorrected systematics or additional source structure (or both). To investigate this, models incorporating additional companions were also fit to the data.

In all datasets, a better fit is provided by including the presence of a second companion with parameters given in Table 7.2. While the best fit separation and contrast suffer the degeneracy described above, the position angle is consistently around $\sim$310°for almost all datasets. The addition of further companions beyond 2 did not substantially improve the fit, and there was no consistency over the location of a third component.

While the detection of a second faint companion in any single dataset does not carry great statistical weight, the consistent finding of the same best fit parameters across all datasets indicates that the structure detected likely arises from real underlying structure in the source. However, as with the single companion fit, the absence of orbital motion with observing epoch makes it appear unlikely that the origin of the closure phases is a true stellar or substellar companion.

Disk Model

Olofsson et al. (2013) suggested that the 2010 L band data may be explained by the presence of forward scattering from the highly inclined disk of T Cha. In order to determine whether the observed closure phases could arise from the disk, we have performed radiative transfer modelling using the MCFOST code (Pinte et al., 2006).

Simulated images were produced from MCFOST models, and the expected closure phases were calculated and compared to the data. We have reproduced the best fit models from Olofsson et al. (2013) and Huélamo et al. (2015). While the inner disks are identical, Olofsson et al. (2013) used a power-law prescription for the surface density profile of the outer disk while Huélamo et al. (2015) used a tapered-edge model. The disk parameters from these models are shown in Table 7.4. The PAH component of the outer disk discussed by Olofsson et al. (2013) was not included in this analysis, due to the strongly degraded fit that it provides to the SAM data. Including PAHs at the level of 0.5% of the outer disk mass substantially increases the resolved flux from the entire outer disk, causing a strong closure phase and square-visibility signal that dwarfs those seen in the data.

As seen in Table 7.3, both of the disk models offer an improved fit to the data compared to an unresolved point source. The Huélamo et al. (2015) disk model contends with the 2-companion model (section 7.1.4) for the best overall fit of any model to the ensemble data, and importantly it does so with no free parameters (the 2-companion model has 6).

Table 7.3: Comparison of reduced χ^2 from several models.

Model	2010 L'	2011 L'	2012 L'	2013 L'	2011 K_s	2013 K_s
Null Hypothesis	4.91	1.34	1.43	2.29	1.63	2.66
1 companion	4.67	1.26	1.22	1.77	1.45	2.67
2 companions	4.52	1.23	1.12	1.61	1.37	2.40
Olofsson 2013 Disk	4.79	1.47	1.21	1.96	1.47	2.66
Huélamo 2015 Disk	4.42	1.31	1.16	1.75	1.46	2.51
Image Reconstruction	1.35	0.46	1.34	0.59	0.54	0.78

Image Reconstruction

To better visualise the physical origin of the closure phase signal present in the SAM data, image reconstruction was performed individually on each of the 6 datasets using the MACIM package (Ireland et al., 2008). The reconstructed images are shown in Fig. 7.2. The unresolved central star has been subtracted, and image reconstruction performed on the residuals. This process allows a higher dynamic range reconstruction of fainter structure, and has been used successfully for other transition disks (e.g. Kraus and Ireland, 2012).

In each of the L' datasets, the same structure is seen: two significant sources located at approximately 90°and 310°from North, consistent with the best fit parameters from the 2-companion model. A matching pair of sources at the same approximate position angles are also seen in the two K_s datasets, but at a closer separation to the host star. The similarity of the image reconstructions over a three year observational window confirms the lack of proper motion previously discussed and lends weight to the disk interpretation.

In the L' images, a third fainter structure is consistently seen South of the central star, but much closer to the noise level. Given the low signal-to-noise, it may be an artefact of the mapping, although if real its location coincides with the rear face of the inner edge of the outer disk, making it a plausible candidate for back scattering from this location.

A model disk with physical properties matching those in Huélamo et al. (2015) was input into radiative transfer modelling code, resulting in the simulated image shown in the left panel of Fig. 7.3. Interestingly, the bright arc corresponding to light forward scattered at the model disk edge occupies the same region that was seen in previous sections to host companions in model fits and bright features in reconstructed images. However, to casual inspection, there is still quite some difference between (for example) the recovered images of Fig. 7.2 and the radiative transfer model.

In order to demonstrate that such qualitatively different representations are in accord with each other and both may represent the same underlying structure, it is important to account for the fact that the image reconstruction process will introduce artefacts. Closure phase data is insensitive to symmetric structure, while square visibilities are insensitive to asymmetric structure. The measurement error for each of these quantities can tune the amount of symmetric and asymmetric structure recovered in the reconstructed images. Furthermore, the highly incomplete coverage, and the mechanisms to subtract the overwhelmingly bright central star all result in biases in the final image.

Table 7.4: Disk models tested.

Zone	Mass [$M_\odot$]	R_{in} [AU]	R_{out} (R_c) [AU]	α (γ)	β	H_0/R_0 [AU]/[AU]	Dust type	Mass Fraction [%]	a_{min} [μm]	a_{max} [μm]	a_{exp}	G/D
Model 1: Best fit model from Olofsson et al. (2013) – Power law density profile for outer disk.												
Inner Disk	2×10^{-11}	0.07	0.11	-1	1	0.02/0.1	Astrosil	70	5	1000	3.5	100
							Carbon	30	0.01	1000	3.5	100
Outer Disk	8×10^{-5}	12	25	-1	1.1	2.1/25	Astrosil	100	0.1	3000	3.5	100
Model 2: Best fit model from Huélamo et al. (2015) – Outer disk with tapered edge.												
Inner Disk	2×10^{-11}	0.07	0.11	-1	1	0.02/0.1	Astrosil	70	5	1000	3.5	100
							Carbon	30	0.01	1000	3.5	100
Outer Disk	9×10^{-5}	21.6	50	-0.5	1.0	4.0/50	Astrosil	70	0.01	30000	3.7	50
							Carbon	30	0.01	30000	3.7	50

To investigate the effects of the image reconstruction process on images of circumstellar disks, the expected closure phases generated by radiative transfer model images was calculated for the exact observing configuration used at each epoch. Noise consistent with the measured uncertainties of each dataset was also added, and the same image reconstruction code was run on the resulting simulated data. An example output simulated map generated by this process for the March 2013 L' epoch is seen in the right panel of Fig. 7.3, and is representative of the results from other L' epochs.

Comparison with Fig. 7.2 now shows that simulated images show excellent correspondence with structures seen in the images reconstructed from real data. By subtracting the central point source, the image reconstruction process typically also removes flux from structures at small separations. For the model images, this has the effect of splitting the continuous arc of forward scattered light from the front edge of the disk into two point sources, resulting in an image similar to those produced from the SAM data.

Although the models of Huélamo et al. (2015) were found to be highly effective at matching the morphology of images recovered in both L' and K_s, in one quantitative sense there was some degree of mismatch. Specifically, the ratio of the flux coming from the resolved component (outer disk) compared to the unresolved component (star plus inner disk) was significantly higher in the observed data than the models predicted. This under-prediction of the outer disk flux contribution was much more pronounced for the K_s data than for the L', further implying that the spectral slope for the disk component was not perfectly represented by the models. Fortunately, it turned out that both of these discrepancies could be amended with a relatively minor tweak to the model: changing the power law index of the grain size distribution from 3.7 to 3.5 in the model of Huélamo et al. (2015) was enough to remove any residual systematic mismatch between images produced from radiative transfer, and those recovered from data at both observing bands. This change to a 3.5 index also matches that used by Olofsson et al. (2013).

7.1.5 Conclusions

We have studied the transitional disk object T Cha over 3 years with multi-wavelength near infrared interfometric imaging data. We recover the companion candidate proposed in Huélamo et al. (2011b), but find a lack of orbital motion rules out the hypothesis that the object is a companion in a co-planar orbit with the disk. Instead, we find that the data are consistent with forward scattering from the rim of a highly inclined outer disk, as suggested by Olofsson et al. (2013).

A significantly better fit to the data is provided by the radiative transfer image produced with updated disk parameters from Huélamo et al. (2015). With a minor tweak to a single parameter (of modest significance), this new model can comprehensively explain all statistically significant signals within our imaging data with no further tailoring and no degrees of freedom.

Image reconstruction from the observed datasets compared with simulated images produced from the disk model confirmed the match between observation and theory. The predominant term contributing to image asymmetry was shown to be an extended arc arising from forward-scattering at the near edge of the model disk. Incomplete information at the image recovery step was shown to cause an appearent split of this arc into two point sources, mimicking the signal produced by two companions. The recovery of essentially the same image structure from each observational dataset shows that image reconstruction can be a useful tool to visualise SAM data. However,

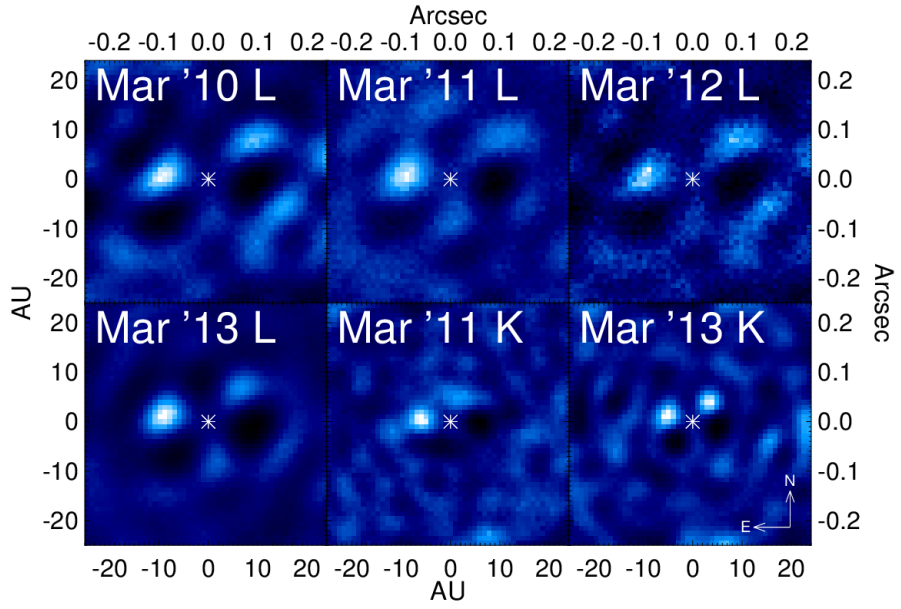

Figure 7.2: The result of applying a maximum entropy image reconstruction algorithm to the SAM data. The same structure of two point sources located to the North-West and East of the central star appear in all epochs, suggesting that it corresponds to real structure. Angular sizes are converted to AU assuming a distance of 108 pc.

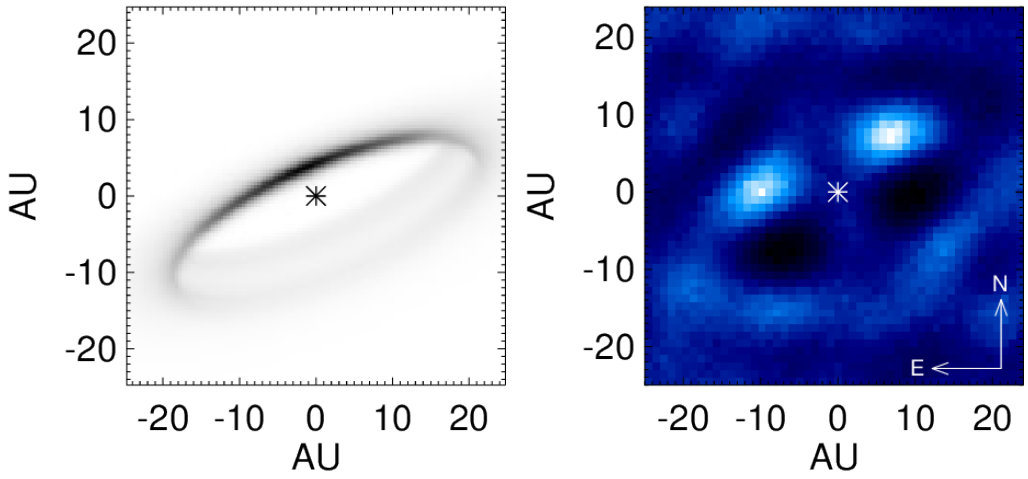

Figure 7.3: Left: A simulated image from radiative transfer modelling of T Cha using the Huélamo et al. (2015) parameters in Table 7.4. Forward scattered light from the close edge of the disk is the dominant source of resolved emission. The contribution from the central star has been removed to highlight the faint disk. The cross indicates the position of the star.
Right: The result of applying image reconstruction to simulated observations of this image, using the measured uncertainties from the March 2013 L band T Cha data. This image matches well with the reconstructed images in Fig. 7.2, suggesting that they trace the same structure.

the image reconstruction process combined with the limitations of the sparse data provided by SAM can introduce strong image artefacts that must be modelled to ensure robust interpretation of recovered structures.

Chapter 8

Conclusions and Future Work

In this thesis I have applied high resolution imaging techniques to the study of planet and star formation, yielding tighter constraints for models of these processes. In addition, I have presented improvements and new ideas for mirror cophasing and interferometric techniques that should ensure optimal performance for new and future instruments that will study these processes in much greater detail.

In Chapter 2, I exploited the ability of interferometric techniques to precisely measure phase to produce a novel technique for the problem of cophasing for segmented mirrors. Development in this area is important to ensure high resolution imaging capabilities of next-generation segmented telescopes are not restricted by segment alignment problems. Called Fizeau Interferometric Cophasing of Segmented Mirrors, the method works for any non-redundant pupil, allowing it to be used in conjunction with segment tilting to cophase an entire mirror without the requirement for dedicated aperture masks. A more robust version of the original algorithm was presented, that allows FICSM to be resistant to increased error processes. Simulations for JWST's NIRCam instrument show that it is more than capable of fulfilling the requirements for a backup cophasing algorithm, by phasing a mirror from an initial state with pistons larger than 70 wavelengths to a final state with an rms of 0.03% of a wavelength.

In Chapter 3, I performed experiments to demonstrate the basic principles of FICSM in a lab environment. A small MEMS segmented deformable mirror was used as a proxy for a larger mirror, and cophased from pistons larger than 5 wavelengths using segment tilting. The mirror was cophased successfully from the largest piston error possible to a state with residuals consistent with the limiting accuracy of the mirror actuation. The results of a further experiment on the JWST testbed telescope were also presented. While technical problems with the setup ultimately stopped the experiment, many important modifications to FICSM were made that ensure it will be more robust for future applications. Most importantly, the requirement for segments to have a regular shape was removed to allow FICSM to be applied to the clipped testbed pupil. This also allows a simple way to incorporate known pupil obstructions and aberrations into the algorithm, such as the telescope spiders that are ubiquitous in modern telesopes.

Due to the problems encountered with the JWST testbed, the next steps for FICSM involve a rigorous test on a setup capable of exploring the full capture range and accuracy expected. This may be possible following the successful repair of the testbed, or using another setup. Tests in a space-like environment are also necessary, which may require the use of a sounding rocket. Applying FICSM on ground based telescopes should also be possible, and preliminary simulations

have begun. Examples of strategies that would make FICSM more robust on a seeing limited setup were provided here, which should aid in this task. Since all of the largest planned optical telescopes will employ segmented designs, development of cophasing strategies is particularly important to ensure optimal telescope performance and improve high resolution imaging capabilities.

In Chapter 4, I used high resolution imaging techniques to study brown dwarfs. The foundation of an adaptive optics orbital monitoring survey was set out, with the first promising results presented. At the conclusion of this study, the orbits of up to 19 brown dwarf binary systems will be calculated. This will allow measurement of dynamical masses for these systems, which, when combined with photometry and distance information, are critical observations needed to test brown dwarf evolutionary models. The discovery of a further sample of brown dwarf companions to intermediate mass stars was also presented. These systems are intriguing examples of extreme mass ratio binary systems, and rare examples of companions in the brown dwarf desert. In the future, orbital monitoring of these targets will provide similar mass-luminosity information to the brown dwarf binary systems studied. In addition, the system ages can be measured from applying well-calibrated stellar models to the primary stars, which will provide a further important constraint for brown dwarf evolutionary models.

In Chapter 5, I performed a multiplicity survey of the nearby Ophiuchus star forming region. A comprehensive study of Ophiuchus members was conducted by combining results from the literature with high resolution NRM data to reveal a more complete picture of the region. The distribution of the binary stars as a function of separation and mass ratio was investigated, yielding similar results to other star forming regions and showing marked differences to results from the field. The observed distribution of mass ratios was consistent with a flat distribution, predicting that the observed lack of brown dwarf companions is not anomalously low but simply an extension of the distribution of stellar mass companions to smaller masses. This conclusion echoes the results of other work targeting both wider separations and other star forming regions. Finally, the relationship between disk hosting stars and multiplicity was explored. This showed that the disk frequency of stars with wide binary companions at greater than ~ 40 AU was similar to that of single stars ($\sim 2/3$), while close binary systems with separations less than ~ 40 AU had a much lower frequency ($\sim 1/3$) at an age of only 1 Myr. This shows that close binary companions significantly speed up the process of dispersal, or inhibit the formation of protoplanetary disks. This has profound implications for giant planet formation, which may take place on longer timescales and hence would be supressed in these systems.

Combining the results of this survey with those of other star forming regions is necessary to get a complete picture of star formation. The regions that have been studied to date span a range of ages, providing information on the time evolution of multiplicity and disk parameters. Several other close star forming regions have not been studied with the same level of rigour as Upper Scorpius, Taurus or Ophiuchus, and performing surveys for these less targeted regions will also help with this task. Ideally, further study of systems younger than the 1–2 Myr age of Ophiuchus is needed to measure the timescale of disk dissipation in close binaries.

In Chapter 6, I presented the results of commissioning NRM on the Gemini Planet Imager (GPI). By combining NRM with the more stable PSF provided by the extreme adaptive optics system, GPI outperforms previous NRM instruments. In addition, the integral field unit provides the opportunity to study the spectral features of objects while simultaneously obtaining high resolution

imaging. The study of resolved polarized structure is made possible through a polarimetric mode, which should prove useful for the study of dust in protoplanetary disks. Two examples of scientific applications were also provided. Using a combination of spectrally dispersed and polarized data, the transition disk HD 142527 was studied. The low mass stellar companion HD 142527B was detected at high significance and with the most accurate measurement of its position to date, crucial for tying down its orbit in the future. Tentative evidence of resolved polarized structure was detected, although further study of instrument systematics is needed to confirm the origin of the observed signal. The supergiant VY CMa was also observed, yielding a high angular resolution image of its extreme stellar winds. Combined with older images from previous instruments, the wind speed was estimated by tracing the position of ejecta over a 17 year time baseline. This data also provided verification of both the orientation of the GPI mask and its imaging capability.

Future observations with GPI NRM should complete the commissioning process, and allow it to be opened to the community. GPI NRM has the potential to do exciting science related to exoplanets and young stars, with the expected obtainable contrast allowing low mass giant planets to be detected around young stars. Combined with coronagraphic and other direct imaging observations, we should soon have a much better understanding of exoplanets at wide separations. In addition, new observations providing photometric and spectroscopic information of these planets will be crucial to improve planet formation and evolutionary models that are currently not well constrained.

Finally, in Chapter 7 I studied the transition disk T Cha with 3 years of NRM observations. The detected source reported to be a substellar companion in previous work was monitored, yielding no evidence of orbital motion. A simulated model of the disk showed that a similar closure phase and visibility signal is produced by forward scattering from the inclined outer disk. Model independent image reconstruction of the data showed that the features strongly resembled those expected from the disk model. Combined, this evidence shows that the detected signal is most likely to originate in the outer disk.

Despite the non-detection of an orbiting companion in our data, other lines of evidence suggest that the disk gap of the T Cha transition disk is most likely caused by a planetary companion. The highly inclined disk makes searching for such a companion difficult, but by incorporating the known disk parameters and looking for residual structure, future high contrast observations may be able to shed light on this hypothesis. The lessons learnt from the T Cha system are important for future studies of other likely planet-hosting transition disks. Taking into account the flux contribution from the disk is important when studying these objects, presenting a huge challenge for highly inclined systems in particular. But with new instruments such as GPI and SPHERE reaching higher contrasts than previously possible, there is huge potential for direct imaging observations to reveal the origin of transition disk gaps.

A number of high resolution imaging instruments are currently coming online at telescopes around the world (e.g. GPI, SPHERE). Prior to the use of these instruments, direct imaging studies were confined to high mass exoplanets at large separations. Despite several dedicated surveys with older instruments (e.g. Lafrenière et al., 2007a; Biller et al., 2013), only a handful of such systems are known, underlining the difficulty of the endeavour. However, these new instruments allow higher contrasts to be obtained at smaller separations, which should lead to many more detections and more detailed study of forming planetary systems. Dedicated surveys with these instruments

will reveal the frequency of low mass giant planets in $\gtrsim 5$ AU orbits around nearby young stars, while targeted studies of individual stars should provide low resolution exoplanet spectra and polarimetric imaging of the outer disks of forming systems in much greater detail than previously attainable.

In addition to the new optical and near-infrared instruments, the new Atacama Large Millimeter Array (ALMA) facility will provide a revolution in our understanding of star and planet formation. ALMA allows high sensitivity and high angular resolution imaging and spectroscopy of cold gas and dust at millimetre wavelengths, giving a direct view into these objects as they form. Similarly, JWST's imaging and spectroscopic capabilities in the near and mid-infrared will surpass current facilities and further extend our reach into these processes.

Looking further ahead, the "Extremely Large Telescopes" are planned to open in the next decade. All three current designs have high resolution exoplanet research as primary science goals, and should allow direct detection of a wider range of exoplanets, as well as high resolution imaging of warm dust and the inner disks of young stars.

The combination of current and future facilities should solve many of the current mysteries surrounding the process of star and planet formation, giving an unprecedented view into the environs of young stars and their circumstellar disks.

Bibliography

D Scott Acton, Timothy Towell, John Schwenker, John Swensen, Duncan Shields, Erin Sabatke, Lana Klingemann, Adam R Contos, Brian Bauer, Karl Hansen, et al. Demonstration of the james webb space telescope commissioning on the jwst testbed telescope. In *Astronomical Telescopes and Instrumentation*, pages 62650R–62650R. International Society for Optics and Photonics, 2006.

D Scott Acton, Timothy Towell, John Schwenker, Duncan Shields, Erin Sabatke, Adam R Contos, Karl Hansen, Fang Shi, Bruce Dean, and Scott Smith. End-to-end commissioning demonstration of the james webb space telescope. In *Optical Engineering+ Applications*, pages 668706–668706. International Society for Optics and Photonics, 2007.

D.S. Acton, J.S. Knight, A. Contos, S. Grimaldi, J. Terry, P. Lightsey, A. Barto, B. League, B. Dean, J. Smith, et al. Wavefront sensing and controls for the james webb space telescope. In *Proc SPIE*, volume 8442, 2012. In Press.

C. Aime, R. Soummer, and A. Ferrari. Total coronagraphic extinction of rectangular apertures using linear prolate apodizations. A&A, 389:334–344, July 2002. doi: 10.1051/0004-6361:20020419.

J. Alcolea, V. Bujarrabal, P. Planesas, D. Teyssier, J. Cernicharo, E. De Beck, L. Decin, C. Dominik, K. Justtanont, A. de Koter, A. P. Marston, G. Melnick, K. M. Menten, D. A. Neufeld, H. Olofsson, M. Schmidt, F. L. Schöier, R. Szczerba, and L. B. F. M. Waters. HIFISTARS Herschel/HIFI observations of VY Canis Majoris. Molecular-line inventory of the envelope around the largest known star. A&A, 559:A93, November 2013. doi: 10.1051/0004-6361/201321683.

R. D. Alexander and P. J. Armitage. Dust dynamics during protoplanetary disc clearing. MNRAS, 375:500–512, February 2007. doi: 10.1111/j.1365-2966.2006.11341.x.

R.J. Allen. Station-keeping requirements for constellations of free-flying collectors used for astronomical imaging in space. *Publications of the Astronomical Society of the Pacific*, 119(858): 914–922, 2007.

K. M. Aller, A. L. Kraus, M. C. Liu, W. S. Burgett, K. C. Chambers, K. W. Hodapp, N. Kaiser, E. A. Magnier, and P. A. Price. A Pan-STARRS + UKIDSS Search for Young, Wide Planetary-mass Companions in Upper Scorpius. ApJ, 773:63, August 2013. doi: 10.1088/0004-637X/773/1/63.

V Ambartsumian. On the statistics of double stars. *Astronomicheskii Zhurnal*, 14:207, 1937.

P. Andre, D. Ward-Thompson, and M. Barsony. Submillimeter continuum observations of Rho Ophiuchi A - The candidate protostar VLA 1623 and prestellar clumps. ApJ, 406:122–141, March 1993. doi: 10.1086/172425.

S. M. Andrews, D. J. Wilner, C. Espaillat, A. M. Hughes, C. P. Dullemond, M. K. McClure, C. Qi, and J. M. Brown. Resolved Images of Large Cavities in Protoplanetary Transition Disks. ApJ, 732:42, May 2011. doi: 10.1088/0004-637X/732/1/42.

S. M. Andrews, K. A. Rosenfeld, A. L. Kraus, and D. J. Wilner. The Mass Dependence between Protoplanetary Disks and their Stellar Hosts. ApJ, 771:129, July 2013. doi: 10.1088/0004-637X/771/2/129.

P. Artymowicz and S. H. Lubow. Dynamics of binary-disk interaction. 1: Resonances and disk gap sizes. ApJ, 421:651–667, February 1994. doi: 10.1086/173679.

V. Bailey, T. Meshkat, M. Reiter, K. Morzinski, J. Males, K. Y. L. Su, P. M. Hinz, M. Kenworthy, D. Stark, E. Mamajek, R. Briguglio, L. M. Close, K. B. Follette, A. Puglisi, T. Rodigas, A. J. Weinberger, and M. Xompero. HD 106906 b: A Planetary-mass Companion Outside a Massive Debris Disk. ApJ, 780:L4, January 2014. doi: 10.1088/2041-8205/780/1/L4.

J. E. Baldwin, C. A. Haniff, C. D. Mackay, and P. J. Warner. Closure phase in high-resolution optical imaging. Nature, 320:595–597, April 1986. doi: 10.1038/320595a0.

I. Baraffe, G. Chabrier, F. Allard, and P. H. Hauschildt. Evolutionary models for solar metallicity low-mass stars: mass-magnitude relationships and color-magnitude diagrams. A&A, 337:403–412, September 1998.

I. Baraffe, G. Chabrier, T. S. Barman, F. Allard, and P. H. Hauschildt. Evolutionary models for cool brown dwarfs and extrasolar giant planets. The case of HD 209458. A&A, 402:701–712, May 2003. doi: 10.1051/0004-6361:20030252.

M. Barsony, C. Koresko, and K. Matthews. A Search for Close Binaries in the ρ Ophiuchi Star-forming Region. ApJ, 591:1064–1074, July 2003. doi: 10.1086/375532.

M. R. Bate. Stellar, brown dwarf and multiple star properties from hydrodynamical simulations of star cluster formation. MNRAS, 392:590–616, January 2009. doi: 10.1111/j.1365-2966.2008.14106.x.

F. C. Bertiau. Absolute Magnitudes of Stars in the Scorpo-Centaurus Association. ApJ, 128:533, November 1958. doi: 10.1086/146569.

J.-L. Beuzit, M. Feldt, K. Dohlen, D. Mouillet, P. Puget, F. Wildi, L. Abe, J. Antichi, A. Baruffolo, P. Baudoz, A. Boccaletti, M. Carbillet, J. Charton, R. Claudi, M. Downing, C. Fabron, P. Feautrier, E. Fedrigo, T. Fusco, J.-L. Gach, R. Gratton, T. Henning, N. Hubin, F. Joos, M. Kasper, M. Langlois, R. Lenzen, C. Moutou, A. Pavlov, C. Petit, J. Pragt, P. Rabou, F. Rigal, R. Roelfsema, G. Rousset, M. Saisse, H.-M. Schmid, E. Stadler, C. Thalmann, M. Turatto,

S. Udry, F. Vakili, and R. Waters. SPHERE: a 'Planet Finder' instrument for the VLT. In Proc. SPIE, volume 7014, July 2008. doi: 10.1117/12.790120.

B. Biller, S. Lacour, A. Juhász, M. Benisty, G. Chauvin, J. Olofsson, J.-U. Pott, A. Müller, A. Sicilia-Aguilar, M. Bonnefoy, P. Tuthill, P. Thebault, T. Henning, and A. Crida. A Likely Close-in Low-mass Stellar Companion to the Transitional Disk Star HD 142527. ApJ, 753:L38, July 2012. doi: 10.1088/2041-8205/753/2/L38.

B. A. Biller, M. C. Liu, Z. Wahhaj, E. L. Nielsen, T. L. Hayward, J. R. Males, A. Skemer, L. M. Close, M. Chun, C. Ftaclas, F. Clarke, N. Thatte, E. L. Shkolnik, I. N. Reid, M. Hartung, A. Boss, D. Lin, S. H. P. Alencar, E. de Gouveia Dal Pino, J. Gregorio-Hetem, and D. Toomey. The Gemini/NICI Planet-Finding Campaign: The Frequency of Planets around Young Moving Group Stars. ApJ, 777:160, November 2013. doi: 10.1088/0004-637X/777/2/160.

W. J. Borucki, D. Koch, G. Basri, N. Batalha, T. Brown, D. Caldwell, J. Caldwell, J. Christensen-Dalsgaard, W. D. Cochran, E. DeVore, E. W. Dunham, A. K. Dupree, T. N. Gautier, J. C. Geary, R. Gilliland, A. Gould, S. B. Howell, J. M. Jenkins, Y. Kondo, D. W. Latham, G. W. Marcy, S. Meibom, H. Kjeldsen, J. J. Lissauer, D. G. Monet, D. Morrison, D. Sasselov, J. Tarter, A. Boss, D. Brownlee, T. Owen, D. Buzasi, D. Charbonneau, L. Doyle, J. Fortney, E. B. Ford, M. J. Holman, S. Seager, J. H. Steffen, W. F. Welsh, J. Rowe, H. Anderson, L. Buchhave, D. Ciardi, L. Walkowicz, W. Sherry, E. Horch, H. Isaacson, M. E. Everett, D. Fischer, G. Torres, J. A. Johnson, M. Endl, P. MacQueen, S. T. Bryson, J. Dotson, M. Haas, J. Kolodziejczak, J. Van Cleve, H. Chandrasekaran, J. D. Twicken, E. V. Quintana, B. D. Clarke, C. Allen, J. Li, H. Wu, P. Tenenbaum, E. Verner, F. Bruhweiler, J. Barnes, and A. Prsa. Kepler Planet-Detection Mission: Introduction and First Results. *Science*, 327:977–, February 2010. doi: 10.1126/science.1185402.

A. P. Boss. Gas Giant Protoplanet Formation: Disk Instability Models with Thermodynamics and Radiative Transfer. ApJ, 563:367–373, December 2001. doi: 10.1086/323694.

J. Bouvier and I. Appenzeller. A magnitude-limited spectroscopic and photometric survey of Rho Ophiuchus X-ray sources. A&AS, 92:481–516, February 1992.

Ron Bracewell. The fourier transform and iis applications. *New York*, 1965.

A. Brandeker, R. Jayawardhana, P. Khavari, K. E. Haisch, Jr., and D. Mardones. Deficit of Wide Binaries in the η Chamaeleontis Young Cluster. ApJ, 652:1572–1584, December 2006. doi: 10.1086/508483.

A. Bressan, P. Marigo, L. Girardi, B. Salasnich, C. Dal Cero, S. Rubele, and A. Nanni. PARSEC: stellar tracks and isochrones with the PAdova and TRieste Stellar Evolution Code. MNRAS, 427:127–145, November 2012. doi: 10.1111/j.1365-2966.2012.21948.x.

N. Calvet, P. D'Alessio, L. Hartmann, D. Wilner, A. Walsh, and M. Sitko. Evidence for a Developing Gap in a 10 Myr Old Protoplanetary Disk. ApJ, 568:1008–1016, April 2002. doi: 10.1086/339061.

J. C. Carson, S. S. Eikenberry, J. J. Smith, and J. M. Cordes. The Cornell High-Order Adaptive Optics Survey for Brown Dwarfs in Stellar Systems. II. Results from Monte Carlo Population Analyses. AJ, 132:1146–1152, September 2006. doi: 10.1086/505705.

G. Chabrier, I. Baraffe, F. Allard, and P. Hauschildt. Evolutionary Models for Very Low-Mass Stars and Brown Dwarfs with Dusty Atmospheres. ApJ, 542:464–472, October 2000. doi: 10.1086/309513.

J. E. Chambers. Making More Terrestrial Planets. Icarus, 152:205–224, August 2001. doi: 10.1006/icar.2001.6639.

G. Chanan, M. Troy, F. Dekens, S. Michaels, J. Nelson, T. Mast, and D. Kirkman. Phasing the mirror segments of the keck telescopes: the broadband phasing algorithm. *Applied Optics*, 37 (1):140–155, 1998.

G. Chanan, M. Troy, and E. Sirko. Phase discontinuity sensing: a method for phasing segmented mirrors in the infrared. *Applied optics*, 38(4):704–713, 1999.

G. Chanan, C. Ohara, and M. Troy. Phasing the mirror segments of the keck telescopes ii: the narrow-band phasing algorithm. *Applied Optics*, 39(25):4706–4714, 2000.

S. Chatterjee, E. B. Ford, S. Matsumura, and F. A. Rasio. Dynamical Outcomes of Planet-Planet Scattering. ApJ, 686:580–602, October 2008. doi: 10.1086/590227.

A.C. Cheetham. Cophasing jwst's segmented mirror using sparse aperture interferometry. Honours thesis, University of Sydney, 2011.

Anthony C Cheetham, Peter G Tuthill, Anand Sivaramakrishnan, and James P Lloyd. Fizeau interferometric cophasing of segmented mirrors. *Optics express*, 20(28):29457–29471, 2012.

Anthony C Cheetham, Nick Cvetojevic, Barnaby Norris, Anand Sivaramakrishnan, and Peter G Tuthill. Fizeau interferometric cophasing of segmented mirrors: experimental validation. *Optics express*, 22(11):12924–12934, 2014.

L. A. Cieza, D. L. Padgett, L. E. Allen, C. E. McCabe, T. Y. Brooke, S. J. Carey, N. L. Chapman, M. Fukagawa, T. L. Huard, A. Noriga-Crespo, D. E. Peterson, and L. M. Rebull. Primordial Circumstellar Disks in Binary Systems: Evidence for Reduced Lifetimes. ApJ, 696:L84–L88, May 2009. doi: 10.1088/0004-637X/696/1/L84.

L. A. Cieza, M. R. Schreiber, G. A. Romero, M. D. Mora, B. Merin, J. J. Swift, M. Orellana, J. P. Williams, P. M. Harvey, and N. J. Evans, II. The Nature of Transition Circumstellar Disks. I. The Ophiuchus Molecular Cloud. ApJ, 712:925, April 2010. doi: 10.1088/0004-637X/712/2/925.

L. A. Cieza, J. Olofsson, P. M. Harvey, C. Pinte, B. Merín, J.-C. Augereau, N. J. Evans, II, J. Najita, T. Henning, and F. Ménard. Herschel Observations of the T Cha Transition Disk: Constraining the Outer Disk Properties. ApJ, 741:L25, November 2011. doi: 10.1088/2041-8205/741/2/L25.

L. A. Cieza, S. Lacour, M. R. Schreiber, S. Casassus, A. Jordán, G. S. Mathews, H. Cánovas, F. Ménard, A. L. Kraus, S. Pérez, P. Tuthill, and M. J. Ireland. Sparse Aperture Masking Observations of the FL Cha Pre-transitional Disk. ApJ, 762:L12, January 2013. doi: 10.1088/2041-8205/762/1/L12.

L. M. Close, N. Siegler, M. Freed, and B. Biller. Detection of Nine M8.0-L0.5 Binaries: The Very Low Mass Binary Population and Its Implications for Brown Dwarf and Very Low Mass Star Formation. ApJ, 587:407–422, April 2003. doi: 10.1086/368177.

L. M. Close, K. B. Follette, J. R. Males, A. Puglisi, M. Xompero, D. Apai, J. Najita, A. J. Weinberger, K. Morzinski, T. J. Rodigas, P. Hinz, V. Bailey, and R. Briguglio. Discovery of Hα Emission from the Close Companion inside the Gap of Transitional Disk HD 142527. ApJ, 781:L30, February 2014. doi: 10.1088/2041-8205/781/2/L30.

Robert W Cox and Raoqiong Tong. Two-and three-dimensional image rotation using the fft. *IEEE Transactions on Image Processing*, 8(9):1297–1299, 1999.

J. R. Crepp and J. A. Johnson. Estimates of the Planet Yield from Ground-based High-contrast Imaging Observations as a Function of Stellar Mass. ApJ, 733:126, June 2011. doi: 10.1088/0004-637X/733/2/126.

T. Currie, S. Daemgen, J. Debes, D. Lafreniere, Y. Itoh, R. Jayawardhana, T. Ratzka, and S. Correia. Direct Imaging and Spectroscopy of a Candidate Companion Below/Near the Deuterium-burning Limit in the Young Binary Star System, ROXs 42B. ApJ, 780:L30, January 2014. doi: 10.1088/2041-8205/780/2/L30.

W. C. Danchi, M. Bester, C. G. Degiacomi, L. J. Greenhill, and C. H. Townes. Characteristics of dust shells around 13 late-type stars. AJ, 107:1469–1513, April 1994. doi: 10.1086/116960.

Jay Daniel, Tony Hull, and John B Barentine. Jwst: Tinsley achievements on the largest beryllium polishing project. In *SPIE Astronomical Telescopes+ Instrumentation*, pages 845021–845021. International Society for Optics and Photonics, 2012.

E. J. de Geus, P. T. de Zeeuw, and J. Lub. Physical parameters of stars in the Scorpio-Centaurus OB association. A&A, 216:44–61, June 1989.

P. T. de Zeeuw, R. Hoogerwerf, J. H. J. de Bruijne, A. G. A. Brown, and A. Blaauw. A HIPPARCOS Census of the Nearby OB Associations. AJ, 117:354–399, January 1999. doi: 10.1086/300682.

E. J. Delgado-Donate, C. J. Clarke, M. R. Bate, and S. T. Hodgkin. On the properties of young multiple stars. MNRAS, 351:617–629, June 2004. doi: 10.1111/j.1365-2966.2004.07803.x.

S. Desidera and M. Barbieri. Properties of planets in binary systems. The role of binary separation. A&A, 462:345–353, January 2007. doi: 10.1051/0004-6361:20066319.

A. P. Digby, S. Hinkley, B. R. Oppenheimer, A. Sivaramakrishnan, J. P. Lloyd, M. D. Perrin, L. C. Roberts, Jr., R. Soummer, D. Brenner, R. B. Makidon, M. Shara, J. Kuhn, J. Graham, P. Kalas, and L. Newburgh. The Challenges of Coronagraphic Astrometry. ApJ, 650:484–496, October 2006. doi: 10.1086/506339.

S. E. Dodson-Robinson, D. Veras, E. B. Ford, and C. A. Beichman. The Formation Mechanism of Gas Giants on Wide Orbits. ApJ, 707:79–88, December 2009. doi: 10.1088/0004-637X/707/1/79.

C. Dominik and A. G. G. M. Tielens. The Physics of Dust Coagulation and the Structure of Dust Aggregates in Space. ApJ, 480:647–673, May 1997.

G. W. Doppmann, D. T. Jaffe, and R. J. White. Stellar Properties of Pre-Main-Sequence Stars from High-Resolution Near-Infrared Spectra. AJ, 126:3043–3057, December 2003. doi: 10.1086/378958.

R. Doyon, J.B. Hutchings, N. Rowlands, D. Touahri, M. Beaulieu, L. Albert, D. Lafrenire, R. Abraham, P. Chayer, L. Ferrarese, et al. The jwst fine guidance sensor (fgs) and near-infrared imager and slitless spectrograph (niriss). In *Proc SPIE*, volume 8442, 2012. In Press.

G. Duchêne. Planet Formation in Binary Systems: A Separation-Dependent Mechanism? ApJ, 709:L114–L118, February 2010. doi: 10.1088/2041-8205/709/2/L114.

G. Duchêne and A. Kraus. Stellar Multiplicity. ARA&A, 51:269–310, August 2013. doi: 10.1146/annurev-astro-081710-102602.

G. Duchêne, J. Bouvier, and T. Simon. Low-mass binaries in the young cluster IC 348: implications for binary formation and evolution. A&A, 343:831–840, March 1999.

C. P. Dullemond and C. Dominik. Dust coagulation in protoplanetary disks: A rapid depletion of small grains. A&A, 434:971–986, May 2005. doi: 10.1051/0004-6361:20042080.

A. Duquennoy and M. Mayor. Multiplicity among solar-type stars in the solar neighbourhood. II - Distribution of the orbital elements in an unbiased sample. A&A, 248:485–524, August 1991.

Bradley Efron. Bootstrap methods: another look at the jackknife. *The annals of Statistics*, pages 1–26, 1979.

J. H. Elias. An infrared study of the Ophiuchus dark cloud. ApJ, 224:453, September 1978. doi: 10.1086/156393.

K. L. Erickson, B. A. Wilking, M. R. Meyer, J. G. Robinson, and L. N. Stephenson. The Initial Mass Function and Disk Frequency of the ρ Ophiuchi Cloud: An Extinction-limited Sample. AJ, 142:140, October 2011. doi: 10.1088/0004-6256/142/4/140.

N. J. Evans, II, L. E. Allen, G. A. Blake, A. C. A. Boogert, T. Bourke, P. M. Harvey, J. E. Kessler, D. W. Koerner, C. W. Lee, L. G. Mundy, P. C. Myers, D. L. Padgett, K. Pontoppidan, A. I. Sargent, K. R. Stapelfeldt, E. F. van Dishoeck, C. H. Young, and K. E. Young. From Molecular

Cores to Planet-forming Disks: An SIRTF Legacy Program. PASP, 115:965–980, August 2003. doi: 10.1086/376697.

NJ Evans, MM Harvey, TL Huard, et al. *Final Delivery of Data from the c2d Legacy Project: IRAC and MIPS*, 2007. `http://irsa.ipac.caltech.edu/data/SPITZER/C2D/doc/c2d_del_document.pdf`.

T. M. Evans, M. J. Ireland, A. L. Kraus, F. Martinache, P. Stewart, P. G. Tuthill, S. Lacour, J. M. Carpenter, and L. A. Hillenbrand. Mapping the Shores of the Brown Dwarf Desert. III. Young Moving Groups. ApJ, 744:120, January 2012. doi: 10.1088/0004-637X/744/2/120.

F. Feroz, M. P. Hobson, and M. Bridges. MULTINEST: an efficient and robust Bayesian inference tool for cosmology and particle physics. MNRAS, 398:1601–1614, October 2009. doi: 10.1111/j.1365-2966.2009.14548.x.

F. Feroz, M. P. Hobson, E. Cameron, and A. N. Pettitt. Importance Nested Sampling and the MultiNest Algorithm. *ArXiv e-prints*, June 2013.

Farhan Feroz and MP Hobson. Multimodal nested sampling: an efficient and robust alternative to markov chain monte carlo methods for astronomical data analyses. MNRAS, 384(2):449–463, 2008.

James R Fienup, Joseph C Marron, Timothy J Schulz, and John H Seldin. Hubble space telescope characterized by using phase-retrieval algorithms. *Applied optics*, 32(10):1747–1767, 1993.

D. A. Fischer and G. W. Marcy. Multiplicity among M dwarfs. ApJ, 396:178–194, September 1992. doi: 10.1086/171708.

H. Fizeau. Prix Bordin: rapport sur le concours de lannée 1867. *C. R. Acad. Sci.*, 66:932–934, 1868.

G. Foo, D. M. Palacios, and G. A. Swartzlander, Jr. Optical vortex coronagraph. *Optics Letters*, 30:3308–3310, December 2005. doi: 10.1364/OL.30.003308.

D. Foreman-Mackey, D. W. Hogg, D. Lang, and J. Goodman. emcee: The MCMC Hammer. PASP, 125:306–312, March 2013. doi: 10.1086/670067.

J. J. Fortney, M. S. Marley, D. Saumon, and K. Lodders. Synthetic Spectra and Colors of Young Giant Planet Atmospheres: Effects of Initial Conditions and Atmospheric Metallicity. ApJ, 683:1104–1116, August 2008. doi: 10.1086/589942.

V. C. Geers, K. M. Pontoppidan, E. F. van Dishoeck, C. P. Dullemond, J.-C. Augereau, B. Merín, I. Oliveira, and J. W. Pel. Spatial separation of small and large grains in the transitional disk around the young star ¡ASTROBJ¿IRS 48¡/ASTROBJ¿. A&A, 469:L35–L38, July 2007. doi: 10.1051/0004-6361:20077524.

A. M. Ghez, G. Neugebauer, and K. Matthews. The multiplicity of T Tauri stars in the star forming regions Taurus-Auriga and Ophiuchus-Scorpius: A 2.2 micron speckle imaging survey. AJ, 106:2005–2023, November 1993. doi: 10.1086/116782.

A. M. Ghez, R. J. White, and M. Simon. High Spatial Resolution Imaging of Pre-Main-Sequence Binary Stars: Resolving the Relationship between Disks and Close Companions. ApJ, 490: 353–367, November 1997.

R. Gilmozzi and J. Spyromilio. The European Extremely Large Telescope (E-ELT). *The Messenger*, 127:11, March 2007.

Roberto Gilmozzi. Science and technology drivers for future giant telescopes. In *Astronomical Telescopes and Instrumentation*, pages 1–10. International Society for Optics and Photonics, 2004.

T. P. Greene and M. R. Meyer. An Infrared Spectroscopic Survey of the rho Ophiuchi Young Stellar Cluster: Masses and Ages from the H-R Diagram. ApJ, 450:233, September 1995. doi: 10.1086/176134.

D. Grether and C. H. Lineweaver. How Dry is the Brown Dwarf Desert? Quantifying the Relative Number of Planets, Brown Dwarfs, and Stellar Companions around Nearby Sun-like Stars. ApJ, 640:1051–1062, April 2006. doi: 10.1086/500161.

E. Han, S. X. Wang, J. T. Wright, Y. K. Feng, M. Zhao, O. Fakhouri, J. I. Brown, and C. Hancock. Exoplanet Orbit Database. II. Updates to Exoplanets.org. PASP, 126:827–837, October 2014. doi: 10.1086/678447.

W. I. Hartkopf, A. Tokovinin, and B. D. Mason. Speckle Interferometry at SOAR in 2010 and 2011: Measures, Orbits, and Rectilinear Fits. AJ, 143:42, February 2012. doi: 10.1088/0004-6256/143/2/42.

J Hartmann. *Bemerkungen über den Bau und die Justirung von Spektrographen*. Springer, 1900.

Michael A Helmbrecht, Min He, Thor Juneau, Matthew Hart, and Nathan Doble. Segmented mems deformable-mirror for wavefront correction. In *Optics East 2006*, pages 63760D–63760D. International Society for Optics and Photonics, 2006.

Michael A Helmbrecht, Min He, Carl J Kempf, and Marc Besse. Mems dm development at iris ao, inc. In *SPIE MOEMS-MEMS*, pages 793108–793108. International Society for Optics and Photonics, 2011.

G. H. Herbig and K. R. Bell. *Third Catalog of Emission-Line Stars of the Orion Population*. 1988.

S. Hinkley, J. M. Carpenter, M. J. Ireland, and A. L. Kraus. Observational Constraints on Companions Inside of 10 AU in the HR 8799 Planetary System. ApJ, 730:L21, April 2011. doi: 10.1088/2041-8205/730/2/L21.

S. Hinkley, B. P. Bowler, A. Vigan, K. M. Aller, M. C. Liu, D. Mawet, E. Matthews, Z. Wahhaj, S. Kraus, I. Baraffe, and G. Chabrier. Early Results from VLT SPHERE: Long-slit Spectroscopy of 2MASS 0122-2439 B, a Young Companion Near the Deuterium Burning Limit. ApJ, 805: L10, May 2015. doi: 10.1088/2041-8205/805/1/L10.

Nancy Houk and M Smith-Moore. Michigan Catalogue of Two-dimensional Spectral Types for the HD Stars. Volume 4, Declinations-26. 0 to-12. 0. *Michigan Spectral Survey (Ann Arbor: Dept. Astron. Univ. Mich.)*, 1, 1988.

O. Hubickyj, P. Bodenheimer, and J. J. Lissauer. Accretion of the gaseous envelope of Jupiter around a 5 10 Earth-mass core. Icarus, 179:415–431, December 2005. doi: 10.1016/j.icarus.2005.06.021.

N. Huélamo, S. Lacour, P. Tuthill, M. Ireland, A. Kraus, and G. Chauvin. A companion candidate in the gap of the t chamaeleontis transitional disk. *Astronomy & Astrophysics*, 528, 2011a.

N Huélamo, S Lacour, P Tuthill, M Ireland, A Kraus, and G Chauvin. A companion candidate in the gap of the t chamaeleontis transitional disk. *Astronomy and Astrophysics*, 528:L7, 2011b.

N. Huélamo, I. de Gregorio-Monsalvo, E. Macias, C. Pinte, M. Ireland, P. Tuthill, and S. Lacour. High resolution observations of the outer disk around T Cha: the view from ALMA. A&A, *accepted*, January 2015.

M. J. Ireland. Phase errors in diffraction-limited imaging: contrast limits for sparse aperture masking. MNRAS, 433:1718–1728, August 2013. doi: 10.1093/mnras/stt859.

M. J. Ireland and A. L. Kraus. The Disk Around CoKu Tauri/4: Circumbinary, Not Transitional. ApJ, 678:L59–L62, May 2008. doi: 10.1086/588216.

M. J. Ireland, A. Kraus, F. Martinache, J. P. Lloyd, and P. G. Tuthill. Dynamical Mass of GJ 802B: A Brown Dwarf in a Triple System. ApJ, 678:463–471, May 2008. doi: 10.1086/529578.

Michael J Ireland, John D Monnier, and Nathalie Thureau. Monte-carlo imaging for optical interferometry. In *Proc. SPIE*, volume 6268, page 62681T, 2008.

M. Janson, D. Lafrenière, R. Jayawardhana, M. Bonavita, J. H. Girard, A. Brandeker, and J. E. Gizis. A Multiplicity Census of Intermediate-mass Stars in Scorpius-Centaurus. ApJ, 773:170, August 2013. doi: 10.1088/0004-637X/773/2/170.

J. H. Jeans. The Stability of a Spherical Nebula. *Royal Society of London Philosophical Transactions Series A*, 199:1–53, 1902. doi: 10.1098/rsta.1902.0012.

P. Kalas, J. R. Graham, E. Chiang, M. P. Fitzgerald, M. Clampin, E. S. Kite, K. Stapelfeldt, C. Marois, and J. Krist. Optical Images of an Exosolar Planet 25 Light-Years from Earth. *Science*, 322:1345–, November 2008. doi: 10.1126/science.1166609.

L. K. Kingsbury and P. D. Atcheson. JWST testbed telescope: a functionally accurate scaled version of the flight optical telescope element used to develop the flight wavefront sensing and control algorithm. In J. C. Mather, editor, *Optical, Infrared, and Millimeter Space Telescopes*, volume 5487 of *Proceedings of SPIE*, pages 875–886, October 2004. doi: 10.1117/12.552859.

R. Köhler, M. Kunkel, C. Leinert, and H. Zinnecker. Multiplicity of X-ray selected T Tauri stars in the Scorpius-Centaurus OB association. A&A, 356:541–558, April 2000.

R. Köhler, M. G. Petr-Gotzens, M. J. McCaughrean, J. Bouvier, G. Duchêne, A. Quirrenbach, and H. Zinnecker. Binary stars in the Orion Nebula Cluster. A&A, 458:461–476, November 2006. doi: 10.1051/0004-6361:20054561.

Q. M. Konopacky, S. J. Thomas, B. A. Macintosh, D. Dillon, N. Sadakuni, J. Maire, M. Fitzgerald, S. Hinkley, P. Kalas, T. Esposito, C. Marois, P. J. Ingraham, F. Marchis, M. D. Perrin, J. R. Graham, J. J. Wang, R. J. De Rosa, K. Morzinski, L. Pueyo, J. K. Chilcote, J. E. Larkin, D. Fabrycky, S. J. Goodsell, B. R. Oppenheimer, J. Patience, L. Saddlemyer, and A. Sivaramakrishnan. Gemini Planet Imager Observational Calibrations V: Astrometry and Distortion. *ArXiv e-prints*, July 2014.

C. D. Koresko. Imaging the Circumstellar Environments of Young Binaries in Southern Star-Forming Regions. AJ, 124:1082–1088, August 2002. doi: 10.1086/341386.

M. B. N. Kouwenhoven, A. G. A. Brown, H. Zinnecker, L. Kaper, and S. F. Portegies Zwart. The primordial binary population. I. A near-infrared adaptive optics search for close visual companions to A star members of Scorpius OB2. A&A, 430:137–154, January 2005. doi: 10.1051/0004-6361:20048124.

M. B. N. Kouwenhoven, A. G. A. Brown, and L. Kaper. A brown dwarf desert for intermediate mass stars in Scorpius OB2? A&A, 464:581–599, March 2007a. doi: 10.1051/0004-6361:20054396.

M. B. N. Kouwenhoven, A. G. A. Brown, S. F. Portegies Zwart, and L. Kaper. The primordial binary population. II.. Recovering the binary population for intermediate mass stars in Scorpius OB2. A&A, 474:77–104, October 2007b. doi: 10.1051/0004-6361:20077719.

K. M. Kratter, R. A. Murray-Clay, and A. N. Youdin. The Runts of the Litter: Why Planets Formed Through Gravitational Instability Can Only Be Failed Binary Stars. ApJ, 710:1375–1386, February 2010. doi: 10.1088/0004-637X/710/2/1375.

A. L. Kraus and L. A. Hillenbrand. The Role of Mass and Environment in Multiple-Star Formation: A 2MASS Survey of Wide Multiplicity in Three Young Associations. ApJ, 662:413–430, June 2007. doi: 10.1086/516835.

A. L. Kraus, M. J. Ireland, F. Martinache, and J. P. Lloyd. Mapping the Shores of the Brown Dwarf Desert. I. Upper Scorpius. ApJ, 679:762–782, May 2008. doi: 10.1086/587435.

A. L. Kraus, M. J. Ireland, F. Martinache, and L. A. Hillenbrand. Mapping the Shores of the Brown Dwarf Desert. II. Multiple Star Formation in Taurus-Auriga. ApJ, 731:8, April 2011. doi: 10.1088/0004-637X/731/1/8.

A. L. Kraus, M. J. Ireland, L. A. Hillenbrand, and F. Martinache. The Role of Multiplicity in Disk Evolution and Planet Formation. ApJ, 745:19, January 2012. doi: 10.1088/0004-637X/745/1/19.

A. L. Kraus, M. J. Ireland, L. A. Cieza, S. Hinkley, T. J. Dupuy, B. P. Bowler, and M. C. Liu. Three Wide Planetary-mass Companions to FW Tau, ROXs 12, and ROXs 42B. ApJ, 781:20, January 2014. doi: 10.1088/0004-637X/781/1/20.

A. L. Kraus, A. M. Cody, K. R. Covey, A. C. Rizzuto, A. W. Mann, and M. J. Ireland. The Mass-Radius Relation of Young Stars, I: UScoCTIO 5, An M4.5 Eclipsing Binary in Upper Scorpius Observed By K2. *ArXiv e-prints*, May 2015.

Adam L Kraus and Michael J Ireland. Lkca 15: A young exoplanet caught at formation? ApJ, 745(1):5, 2012.

John E Krist and Christopher J Burrows. Phase-retrieval analysis of pre-and post-repair hubble space telescope images. *Applied optics*, 34(22):4951–4964, 1995.

S. Lacour, P. Tuthill, P. Amico, M. Ireland, D. Ehrenreich, N. Huélamo, and A.-M. Lagrange. Sparse aperture masking at the VLT. I. Faint companion detection limits for the two debris disk stars HD 92945 and HD 141569. A&A, 532:A72, August 2011. doi: 10.1051/0004-6361/201116712.

S. Lacour, B. Biller, A. Cheetham, A. Greenbaum, P. Tuthill, and The GPI Team (to add). Mass, Temperature and Orbital Parameters of HD 142527B. *in prep.*, June 2015.

D. Lafrenière, R. Doyon, C. Marois, D. Nadeau, B. R. Oppenheimer, P. F. Roche, F. Rigaut, J. R. Graham, R. Jayawardhana, D. Johnstone, P. G. Kalas, B. Macintosh, and R. Racine. The Gemini Deep Planet Survey. ApJ, 670:1367–1390, December 2007a. doi: 10.1086/522826.

D. Lafrenière, C. Marois, R. Doyon, D. Nadeau, and É. Artigau. A New Algorithm for Point-Spread Function Subtraction in High-Contrast Imaging: A Demonstration with Angular Differential Imaging. ApJ, 660:770–780, May 2007b. doi: 10.1086/513180.

D. Lafrenière, R. Jayawardhana, M. H. van Kerkwijk, A. Brandeker, and M. Janson. An Adaptive Optics Multiplicity Census of Young Stars in Upper Scorpius. ApJ, 785:47, April 2014. doi: 10.1088/0004-637X/785/1/47.

A.-M. Lagrange, M. Bonnefoy, G. Chauvin, D. Apai, D. Ehrenreich, A. Boccaletti, D. Gratadour, D. Rouan, D. Mouillet, S. Lacour, and M. Kasper. A Giant Planet Imaged in the Disk of the Young Star β Pictoris. *Science*, 329:57–, July 2010. doi: 10.1126/science.1187187.

J.-B. Le Bouquin. A close-in companion to HD142384. *ArXiv e-prints*, August 2014.

J. J. Lissauer. Planet formation. ARA&A, 31:129–174, 1993. doi: 10.1146/annurev.aa.31.090193.001021.

J. P. Lloyd, F. Martinache, M. J. Ireland, J. D. Monnier, S. H. Pravdo, S. B. Shaklan, and P. G. Tuthill. Direct Detection of the Brown Dwarf GJ 802B with Adaptive Optics Masking Interferometry. ApJ, 650:L131–L134, October 2006. doi: 10.1086/508771.

J.P. Lloyd, F. Martinache, M.J. Ireland, J.D. Monnier, S.H. Pravdo, S.B. Shaklan, and P.G. Tuthill. Direct detection of the brown dwarf gj 802b with adaptive optics masking interferometry. *The Astrophysical Journal Letters*, 650:L131, 2006.

L. Loinard, R. M. Torres, A. J. Mioduszewski, and L. F. Rodríguez. A Preliminary VLBA Distance to the Core of Ophiuchus, with an Accuracy of 4%. ApJ, 675:L29–L32, March 2008. doi: 10.1086/529548.

M. Lombardi, C. J. Lada, and J. Alves. Hipparcos distance estimates of the Ophiuchus and the Lupus cloud complexes. A&A, 480:785–792, March 2008. doi: 10.1051/0004-6361:20079110.

KS Long. Jwst mission operations concept document (jwst-ops-002018). *STScI, Baltimore*, 2006.

R. B. Loren and A. Wootten. A massive prestellar molecular core and adjacent compression front in the Rho Ophiuchi cloud. ApJ, 306:142–159, July 1986. doi: 10.1086/164327.

K. L. Luhman and E. E. Mamajek. The Disk Population of the Upper Scorpius Association. ApJ, 758:31, October 2012. doi: 10.1088/0004-637X/758/1/31.

K. L. Luhman and G. H. Rieke. Low-Mass Star Formation and the Initial Mass Function in the ρ Ophiuchi Cloud Core. ApJ, 525:440–465, November 1999. doi: 10.1086/307891.

K. L. Luhman, J. R. Stauffer, A. A. Muench, G. H. Rieke, E. A. Lada, J. Bouvier, and C. J. Lada. A Census of the Young Cluster IC 348. ApJ, 593:1093–1115, August 2003. doi: 10.1086/376594.

B. A. Macintosh, J. R. Graham, D. W. Palmer, R. Doyon, J. Dunn, D. T. Gavel, J. Larkin, B. Oppenheimer, L. Saddlemyer, A. Sivaramakrishnan, J. K. Wallace, B. Bauman, D. A. Erickson, C. Marois, L. A. Poyneer, and R. Soummer. The Gemini Planet Imager: from science to design to construction. In *Society of Photo-Optical Instrumentation Engineers (SPIE) Conference Series*, volume 7015 of *Society of Photo-Optical Instrumentation Engineers (SPIE) Conference Series*, page 18, July 2008b. doi: 10.1117/12.788083.

B. A. Macintosh, J. R. Graham, D. W. Palmer, R. Doyon, J. Dunn, D. T. Gavel, J. Larkin, B. Oppenheimer, L. Saddlemyer, A. Sivaramakrishnan, J. K. Wallace, B. Bauman, D. A. Erickson, C. Marois, L. A. Poyneer, and R. Soummer. The Gemini Planet Imager: from science to design to construction. In Proc. SPIE, volume 7015, July 2008a. doi: 10.1117/12.788083.

E. E. Mamajek. On the distance to the Ophiuchus star-forming region. *Astronomische Nachrichten*, 329:10, January 2008. doi: 10.1002/asna.200710827.

G. W. Marcy and R. P. Butler. Planets Orbiting Other Suns. PASP, 112:137–140, February 2000. doi: 10.1086/316516.

G.-D. Marleau and A. Cumming. Constraining the initial entropy of directly detected exoplanets. MNRAS, 437:1378–1399, January 2014. doi: 10.1093/mnras/stt1967.

C. Marois, R. Doyon, R. Racine, and D. Nadeau. Efficient Speckle Noise Attenuation in Faint Companion Imaging. PASP, 112:91–96, January 2000. doi: 10.1086/316492.

C. Marois, D. Lafrenière, R. Doyon, B. Macintosh, and D. Nadeau. Angular Differential Imaging: A Powerful High-Contrast Imaging Technique. ApJ, 641:556–564, April 2006. doi: 10.1086/500401.

C. Marois, B. Macintosh, T. Barman, B. Zuckerman, I. Song, J. Patience, D. Lafrenière, and R. Doyon. Direct Imaging of Multiple Planets Orbiting the Star HR 8799. *Science*, 322:1348–, November 2008. doi: 10.1126/science.1166585.

C. Marois, B. Zuckerman, Q. M. Konopacky, B. Macintosh, and T. Barman. Images of a fourth planet orbiting HR 8799. Nature, 468:1080–1083, December 2010. doi: 10.1038/nature09684.

C. Marois, C. Correia, J.-P. Véran, and T. Currie. TLOCI: A Fully Loaded Speckle Killing Machine. In M. Booth, B. C. Matthews, and J. R. Graham, editors, *IAU Symposium*, volume 299 of *IAU Symposium*, pages 48–49, January 2014. doi: 10.1017/S1743921313007813.

E. L. Martin, T. Montmerle, J. Gregorio-Hetem, and S. Casanova. Spectroscopic classification of X-ray selected stars in the rho Ophiuchi star-forming region and vicinity. MNRAS, 300: 733–746, November 1998. doi: 10.1046/j.1365-8711.1998.01932.x.

F. Martinache. Kernel Phase in Fizeau Interferometry. ApJ, 724:464–469, November 2010. doi: 10.1088/0004-637X/724/1/464.

F. Martinache and O. Guyon. The Subaru Coronagraphic Extreme-AO Project. In *Society of Photo-Optical Instrumentation Engineers (SPIE) Conference Series*, volume 7440 of *Society of Photo-Optical Instrumentation Engineers (SPIE) Conference Series*, page 0, August 2009. doi: 10.1117/12.826365.

B. D. Mason, T. ten Brummelaar, D. R. Gies, W. I. Hartkopf, and M. L. Thaller. ICCD Speckle Observations of Binary Stars.XVIII.An Investigation of Be =. AJ, 114:2112, November 1997. doi: 10.1086/118630.

D. Mawet, P. Riaud, O. Absil, and J. Surdej. Annular Groove Phase Mask Coronagraph. ApJ, 633:1191–1200, November 2005. doi: 10.1086/462409.

M. Mayor and D. Queloz. A Jupiter-mass companion to a solar-type star. Nature, 378:355–359, November 1995. doi: 10.1038/378355a0.

S. A. Metchev and L. A. Hillenbrand. The Palomar/Keck Adaptive Optics Survey of Young Solar Analogs: Evidence for a Universal Companion Mass Function. ApJS, 181:62–109, March 2009. doi: 10.1088/0067-0049/181/1/62.

M. R. Meyer, B. A. Wilking, and H. Zinnecker. Young low mass stars in the vicinity of Sigma Scorpii. AJ, 105:619–629, February 1993. doi: 10.1086/116459.

Albert Abraham Michelson. On the application of interference methods to astronomical measurements. *The Astrophysical Journal*, 51:257, 1920.

J. D. Monnier, P. G. Tuthill, B. Lopez, P. Cruzalebes, W. C. Danchi, and C. A. Haniff. The Last Gasps of VY Canis Majoris: Aperture Synthesis and Adaptive Optics Imagery. ApJ, 512: 351–361, February 1999. doi: 10.1086/306761.

JD Monnier, PG Tuthill, M. Ireland, R. Cohen, A. Tannirkulam, and MD Perrin. Mid-infrared size survey of young stellar objects: Description of keck segment-tilting experiment and basic results. *The Astrophysical Journal*, 700:491, 2009.

J. Nelson and G. H. Sanders. The status of the Thirty Meter Telescope project. In *Society of Photo-Optical Instrumentation Engineers (SPIE) Conference Series*, volume 7012 of *Society of Photo-Optical Instrumentation Engineers (SPIE) Conference Series*, page 1, July 2008. doi: 10.1117/12.788238.

JE Nelson. The university of california 10-m telescope project. *J. Opt. Soc. America, Vol. 69, p. 1436*, 69:1436, 1979.

Jerry E Nelson. Design concepts for the california extremely large telescope (celt). In *Astronomical Telescopes and Instrumentation*, pages 282–289. International Society for Optics and Photonics, 2000.

Christopher Neyman, Ralf Flicker, and Sergey Panteleev. Effect of keck segment figure errors on keck ao performance. *Keck Adaptive Optics Note469*, 2007.

B. Norris, G. Schworer, P. Tuthill, N. Jovanovic, O. Guyon, P. Stewart, and F. Martinache. The VAMPIRES instrument: imaging the innermost regions of protoplanetary discs with polarimetric interferometry. MNRAS, 447:2894–2906, March 2015. doi: 10.1093/mnras/stu2529.

B. R. M. Norris, P. G. Tuthill, M. J. Ireland, S. Lacour, A. A. Zijlstra, F. Lykou, T. M. Evans, P. Stewart, and T. R. Bedding. A close halo of large transparent grains around extreme red giant stars. Nature, 484:220–222, April 2012. doi: 10.1038/nature10935.

E. O'Gorman, W. Vlemmings, A. M. S. Richards, A. Baudry, E. De Beck, L. Decin, G. M. Harper, E. M. Humphreys, P. Kervella, T. Khouri, and S. Muller. ALMA observations of anisotropic dust mass loss in the inner circumstellar environment of the red supergiant VY Canis Majoris. A&A, 573:L1, January 2015. doi: 10.1051/0004-6361/201425101.

J. Olofsson, M. Benisty, J.-C. Augereau, C. Pinte, F. Ménard, E. Tatulli, J.-P. Berger, F. Malbet, B. Merín, E. F. van Dishoeck, S. Lacour, K. M. Pontoppidan, J.-L. Monin, J. M. Brown, and G. A. Blake. Warm dust resolved in the cold disk around T Chamaeleontis with VLTI/AMBER. A&A, 528:L6, April 2011. doi: 10.1051/0004-6361/201016074.

J. Olofsson, M. Benisty, J.-B. Le Bouquin, J.-P. Berger, S. Lacour, F. Ménard, T. Henning, A. Crida, L. Burtscher, G. Meeus, T. Ratzka, C. Pinte, J.-C. Augereau, F. Malbet, B. Lazareff, and W. Traub. Sculpting the disk around T Chamaeleontis: an interferometric view. A&A, 552: A4, April 2013. doi: 10.1051/0004-6361/201220675.

R. D. Oudmaijer and A. M. Parr. The binary fraction and mass ratio of Be and B stars: a comparative Very Large Telescope/NACO study. MNRAS, 405:2439–2446, July 2010. doi: 10.1111/j.1365-2966.2010.16609.x.

M. J. Pecaut and E. E. Mamajek. Intrinsic Colors, Temperatures, and Bolometric Corrections of Pre-main-sequence Stars. ApJS, 208:9, September 2013. doi: 10.1088/0067-0049/208/1/9.

M. J. Pecaut, E. E. Mamajek, and E. J. Bubar. A Revised Age for Upper Scorpius and the Star Formation History among the F-type Members of the Scorpius-Centaurus OB Association. ApJ, 746:154, February 2012. doi: 10.1088/0004-637X/746/2/154.

S. Perez, S. Casassus, F. Ménard, P. Roman, G. van der Plas, L. Cieza, C. Pinte, V. Christiaens, and A. S. Hales. CO Gas Inside the Protoplanetary Disk Cavity in HD 142527: Disk Structure from ALMA. ApJ, 798:85, January 2015. doi: 10.1088/0004-637X/798/2/85.

M. D. Perrin, R. Soummer, E. M. Elliott, M. D. Lallo, and A. Sivaramakrishnan. Simulating point spread functions for the James Webb Space Telescope with WebbPSF. In *Society of Photo-Optical Instrumentation Engineers (SPIE) Conference Series*, volume 8442 of *Society of Photo-Optical Instrumentation Engineers (SPIE) Conference Series*, page 3, September 2012. doi: 10.1117/12.925230.

M. D. Perrin, J. Maire, P. Ingraham, D. Savransky, M. Millar-Blanchaer, S. G. Wolff, J.-B. Ruffio, J. J. Wang, Z. H. Draper, N. Sadakuni, C. Marois, A. Rajan, M. P. Fitzgerald, B. Macintosh, J. R. Graham, R. Doyon, J. E. Larkin, J. K. Chilcote, S. J. Goodsell, D. W. Palmer, K. Labrie, M. Beaulieu, R. J. De Rosa, A. Z. Greenbaum, M. Hartung, P. Hibon, Q. Konopacky, D. Lafreniere, J.-F. Lavigne, F. Marchis, J. Patience, L. Pueyo, F. T. Rantakyrö, R. Soummer, A. Sivaramakrishnan, S. Thomas, K. Ward-Duong, and S. Wiktorowicz. Gemini Planet Imager Observational Calibrations I: Overview of the GPI Data Reduction Pipeline. *ArXiv e-prints*, July 2014.

M. D. Perrin, G. Duchene, M. Millar-Blanchaer, M. P. Fitzgerald, J. R. Graham, S. J. Wiktorowicz, P. G. Kalas, B. Macintosh, B. Bauman, A. Cardwell, J. Chilcote, R. J. De Rosa, D. Dillon, R. Doyon, J. Dunn, D. Erikson, D. Gavel, S. Goodsell, M. Hartung, P. Hibon, P. Ingraham, D. Kerley, Q. Konapacky, J. E. Larkin, J. Maire, F. Marchis, C. Marois, T. Mittal, K. M. Morzinski, B. R. Oppenheimer, D. W. Palmer, J. Patience, L. Poyneer, L. Pueyo, F. T. Rantakyrö, N. Sadakuni, L. Saddlemyer, D. Savransky, R. Soummer, A. Sivaramakrishnan, I. Song, S. Thomas, J. K. Wallace, J. J. Wang, and S. G. Wolff. Polarimetry with the Gemini Planet Imager: Methods, Performance at First Light, and the Circumstellar Ring around HR 4796A. ApJ, 799:182, February 2015. doi: 10.1088/0004-637X/799/2/182.

C. Pinte, F. Ménard, G. Duchêne, and P. Bastien. Monte Carlo radiative transfer in protoplanetary disks. A&A, 459:797–804, December 2006. doi: 10.1051/0004-6361:20053275.

J. B. Pollack, O. Hubickyj, P. Bodenheimer, J. J. Lissauer, M. Podolak, and Y. Greenzweig. Formation of the Giant Planets by Concurrent Accretion of Solids and Gas. Icarus, 124:62–85, November 1996. doi: 10.1006/icar.1996.0190.

B. Pope, F. Martinache, and P. Tuthill. Dancing in the Dark: New Brown Dwarf Binaries from Kernel Phase Interferometry. ApJ, 767:110, April 2013. doi: 10.1088/0004-637X/767/2/110.

L. Prato. A Survey for Young Spectroscopic Binary K7-M4 Stars in Ophiuchus. ApJ, 657:338–346, March 2007. doi: 10.1086/510882.

T. Preibisch and E. Mamajek. *The Nearest OB Association: Scorpius-Centaurus (Sco OB2)*, page 235. December 2008.

T. Preibisch and H. Zinnecker. The History of Low-Mass Star Formation in the Upper Scorpius OB Association. AJ, 117:2381–2397, May 1999. doi: 10.1086/300842.

T. Preibisch, E. Guenther, H. Zinnecker, M. Sterzik, S. Frink, and S. Roeser. A lithium-survey for pre-main sequence stars in the Upper Scorpius OB association. A&A, 333:619–628, May 1998.

T. Preibisch, A. G. A. Brown, T. Bridges, E. Guenther, and H. Zinnecker. Exploring the Full Stellar Population of the Upper Scorpius OB Association. AJ, 124:404–416, July 2002. doi: 10.1086/341174.

W.H. Press, B.P. Flannery, S.A. Teukolsky, and W.T. Vetterling. *Numerical Recipes*. Cambridge Univ Press, 1986.

S. P. Quanz, H. Avenhaus, E. Buenzli, A. Garufi, H. M. Schmid, and S. Wolf. Gaps in the HD 169142 Protoplanetary Disk Revealed by Polarimetric Imaging: Signs of Ongoing Planet Formation? ApJ, 766:L2, March 2013. doi: 10.1088/2041-8205/766/1/L2.

Roberto Ragazzoni. Pupil plane wavefront sensing with an oscillating prism. *Journal of modern optics*, 43(2):289–293, 1996.

D. Raghavan, H. A. McAlister, T. J. Henry, D. W. Latham, G. W. Marcy, B. D. Mason, D. R. Gies, R. J. White, and T. A. ten Brummelaar. A Survey of Stellar Families: Multiplicity of Solar-type Stars. ApJS, 190:1–42, September 2010. doi: 10.1088/0067-0049/190/1/1.

J. Rameau, G. Chauvin, A.-M. Lagrange, A. Boccaletti, S. P. Quanz, M. Bonnefoy, J. H. Girard, P. Delorme, S. Desidera, H. Klahr, C. Mordasini, C. Dumas, and M. Bonavita. Discovery of a Probable 4-5 Jupiter-mass Exoplanet to HD 95086 by Direct Imaging. ApJ, 772:L15, August 2013. doi: 10.1088/2041-8205/772/2/L15.

F. A. Rasio and E. B. Ford. Dynamical instabilities and the formation of extrasolar planetary systems. *Science*, 274:954–956, November 1996. doi: 10.1126/science.274.5289.954.

T. Ratzka, R. Köhler, and C. Leinert. A multiplicity survey of the ρ Ophiuchi molecular clouds. A&A, 437:611–626, July 2005. doi: 10.1051/0004-6361:20042107.

S. Reffert, C. Bergmann, A. Quirrenbach, T. Trifonov, and A. Künstler. Precise radial velocities of giant stars. VII. Occurrence rate of giant extrasolar planets as a function of mass and metallicity. A&A, 574:A116, February 2015. doi: 10.1051/0004-6361/201322360.

I. N. Reid and J. E. Gizis. Low-Mass Binaries and the Stellar Luminosity Function. AJ, 113:2246, June 1997. doi: 10.1086/118436.

I. N. Reid, J. E. Gizis, and S. L. Hawley. The Palomar/MSU Nearby Star Spectroscopic Survey. IV. The Luminosity Function in the Solar Neighborhood and M Dwarf Kinematics. AJ, 124: 2721–2738, November 2002. doi: 10.1086/343777.

I. N. Reid, E. Lewitus, P. R. Allen, K. L. Cruz, and A. J. Burgasser. A Search for Binary Systems among the Nearest L Dwarfs. AJ, 132:891–901, August 2006. doi: 10.1086/505626.

I. N. Reid, K. L. Cruz, A. J. Burgasser, and M. C. Liu. L-Dwarf Binaries in the 20-Parsec Sample. AJ, 135:580–587, February 2008. doi: 10.1088/0004-6256/135/2/580.

B. Reipurth and H. Zinnecker. Visual binaries among pre-main sequence stars. A&A, 278:81–108, October 1993.

L. Richter, A. Kemball, and J. Jonas. Simultaneous VLBA polarimetric observations of the v = {1,2} J = 1-0 and v =1, J = 2-1 SiO maser emission towards VY CMa: maser morphology and pumping. MNRAS, 436:1708–1720, December 2013. doi: 10.1093/mnras/stt1686.

A. C. Rizzuto, M. J. Ireland, and J. G. Robertson. Multidimensional Bayesian membership analysis of the Sco OB2 moving group. MNRAS, 416:3108–3117, October 2011. doi: 10.1111/j.1365-2966.2011.19256.x.

A. C. Rizzuto, M. J. Ireland, J. G. Robertson, Y. Kok, P. G. Tuthill, B. A. Warrington, X. Haubois, W. J. Tango, B. Norris, T. ten Brummelaar, A. L. Kraus, A. Jacob, and C. Laliberte-Houdeville. Long-baseline interferometric multiplicity survey of the Sco-Cen OB association. MNRAS, 436:1694–1707, December 2013. doi: 10.1093/mnras/stt1690.

T. J. Rodigas, K. B. Follette, A. Weinberger, L. Close, and D. C. Hines. Polarized Light Imaging of the HD 142527 Transition Disk with the Gemini Planet Imager: Dust around the Close-in Companion. ApJ, 791:L37, August 2014. doi: 10.1088/2041-8205/791/2/L37.

JM Rodríguez-Ramos and JJ Fuensalida. Phasing of segmented mirrors: a new algorithm for piston detection. *Monthly Notices of the Royal Astronomical Society*, 328(1):167–173, 2001.

T. Roell, R. Neuhäuser, A. Seifahrt, and M. Mugrauer. Extrasolar planets in stellar multiple systems. A&A, 542:A92, June 2012. doi: 10.1051/0004-6361/201118051.

D. Rouan, P. Riaud, A. Boccaletti, Y. Clénet, and A. Labeyrie. The Four-Quadrant Phase-Mask Coronagraph. I. Principle. PASP, 112:1479–1486, November 2000. doi: 10.1086/317707.

E. Sabatke, J. Burge, and D. Sabatke. Analytic diffraction analysis of a 32-m telescope with hexagonal segments for high-contrast imaging. *Applied optics*, 44(8):1360–1365, 2005.

C. Scharf and K. Menou. Long-Period Exoplanets From Dynamical Relaxation. ApJ, 693:L113–L117, March 2009. doi: 10.1088/0004-637X/693/2/L113.

D. J. Schlegel, D. P. Finkbeiner, and M. Davis. Maps of Dust Infrared Emission for Use in Estimation of Reddening and Cosmic Microwave Background Radiation Foregrounds. ApJ, 500:525–553, June 1998. doi: 10.1086/305772.

Th Schmidt-Kaler. Physical parameters of the stars. *Landolt-Bornstein New Series*, 2:19, 1982.

G. Schneider and M. D. Silverstone. Coronagraphy with HST: detectability is a sensitive issue. In A. B. Schultz, editor, *High-Contrast Imaging for Exo-Planet Detection.*, volume 4860 of *Society of Photo-Optical Instrumentation Engineers (SPIE) Conference Series*, pages 1–9, February 2003.

Roland V Shack and BC Platt. Production and use of a lenticular hartmann screen. In *Journal of the Optical Society of America*, volume 61, page 656. AMER INST PHYSICS CIRCULATION FULFILLMENT DIV, 500 SUNNYSIDE BLVD, WOODBURY, NY 11797-2999, 1971.

Fang Shi, Gary Chanan, Catherine Ohara, Mitchell Troy, and David C Redding. Experimental verification of dispersed fringe sensing as a segment phasing technique using the keck telescope. *Applied optics*, 43(23):4474–4481, 2004.

L. Siess, E. Dufour, and M. Forestini. An internet server for pre-main sequence tracks of low- and intermediate-mass stars. A&A, 358:593–599, June 2000.

M. Simon, A. M. Ghez, C. Leinert, L. Cassar, W. P. Chen, R. R. Howell, R. F. Jameson, K. Matthews, G. Neugebauer, and A. Richichi. A lunar occultation and direct imaging survey of multiplicity in the Ophiuchus and Taurus star-forming regions. ApJ, 443:625–637, April 1995. doi: 10.1086/175554.

A. Sivaramakrishnan, R. Soummer, L. Pueyo, J.K. Wallace, and M. Shao. Sensing phase aberrations behind lyot coronagraphs. *The Astrophysical Journal*, 688:701, 2008.

A. Sivaramakrishnan, P.G. Tuthill, M.J. Ireland, J.P. Lloyd, F. Martinache, R. Soummer, R.B. Makidon, R. Doyon, M. Beaulieu, and C.A. Beichman. Planetary system and star formation science with non-redundant masking on jwst. In *Proceedings of SPIE*, volume 7440, page 74400Y, 2009.

A. Sivaramakrishnan, R. Soummer, B.R. Oppenheimer, G.L. Carr, J.L. Mey, D. Brenner, C.W. Mandeville, N. Zimmerman, B.A. Macintosh, J.R. Graham, et al. Gemini planet imager coronagraph testbed results. In *Proceedings of SPIE*, volume 7735, page 773586, 2010.

A. Sivaramakrishnan, D. Lafrenière, K. E. S. Ford, B. McKernan, A. Cheetham, A. Z. Greenbaum, P. G. Tuthill, J. P. Lloyd, M. J. Ireland, R. Doyon, M. Beaulieu, A. Martel, A. Koekemoer, F. Martinache, and P. Teuben. Non-redundant Aperture Masking Interferometry (AMI) and segment phasing with JWST-NIRISS. In *Society of Photo-Optical Instrumentation Engineers (SPIE) Conference Series*, volume 8442 of *Society of Photo-Optical Instrumentation Engineers (SPIE) Conference Series*, page 2, September 2012. doi: 10.1117/12.925565.

MF Skrutskie, RM Cutri, R Stiening, MD Weinberg, S Schneider, JM Carpenter, C Beichman, R Capps, T Chester, J Elias, et al. The two micron all sky survey (2mass). AJ, 131(2):1163, 2006.

A. Slettebak. Spectral types and rotational velocities of the brighter Be stars and A-F type shell stars. ApJS, 50:55–83, September 1982. doi: 10.1086/190820.

I. Song, B. Zuckerman, and M. S. Bessell. New Members of the Scorpius-Centaurus Complex and Ages of Its Sub-regions. AJ, 144:8, July 2012. doi: 10.1088/0004-6256/144/1/8.

R. Soummer, C. Aime, and P. E. Falloon. Stellar coronagraphy with prolate apodized circular apertures. A&A, 397:1161–1172, January 2003. doi: 10.1051/0004-6361:20021573.

R. Soummer, A. Ferrari, C. Aime, and L. Jolissaint. Speckle Noise and Dynamic Range in Coronagraphic Images. ApJ, 669:642–656, November 2007. doi: 10.1086/520913.

R. Soummer, L. Pueyo, and J. Larkin. Detection and Characterization of Exoplanets and Disks Using Projections on Karhunen-Loève Eigenimages. ApJ, 755:L28, August 2012. doi: 10.1088/2041-8205/755/2/L28.

D. Stamatellos and A. P. Whitworth. The properties of brown dwarfs and low-mass hydrogen-burning stars formed by disc fragmentation. MNRAS, 392:413–427, January 2009. doi: 10.1111/j.1365-2966.2008.14069.x.

R. Teixeira, C. Ducourant, M. J. Sartori, J. I. B. Camargo, J. P. Périé, J. R. D. Lépine, and P. Benevides-Soares. Proper motions of pre-main sequence stars { } in southern star-forming regions. A&A, 361:1143–1151, September 2000.

C. Thalmann, C. A. Grady, M. Goto, J. P. Wisniewski, M. Janson, T. Henning, M. Fukagawa, M. Honda, G. D. Mulders, M. Min, A. Moro-Martín, M. W. McElwain, K. W. Hodapp, J. Carson, L. Abe, W. Brandner, S. Egner, M. Feldt, T. Fukue, T. Golota, O. Guyon, J. Hashimoto, Y. Hayano, M. Hayashi, S. Hayashi, M. Ishii, R. Kandori, G. R. Knapp, T. Kudo, N. Kusakabe, M. Kuzuhara, T. Matsuo, S. Miyama, J.-I. Morino, T. Nishimura, T.-S. Pyo, E. Serabyn, H. Shibai, H. Suto, R. Suzuki, M. Takami, N. Takato, H. Terada, D. Tomono, E. L. Turner, M. Watanabe, T. Yamada, H. Takami, T. Usuda, and M. Tamura. Imaging of a Transitional Disk Gap in Reflected Light: Indications of Planet Formation Around the Young Solar Analog LkCa 15. ApJ, 718:L87–L91, August 2010. doi: 10.1088/2041-8205/718/2/L87.

A. Tokovinin, B. D. Mason, and W. I. Hartkopf. Speckle Interferometry at SOAR in 2012 and 2013. AJ, 147:123, May 2014. doi: 10.1088/0004-6256/147/5/123.

C. A. O. Torres, G. R. Quast, L. da Silva, R. de La Reza, C. H. F. Melo, and M. Sterzik. Search for associations containing young stars (SACY). I. Sample and searching method. A&A, 460:695–708, December 2006. doi: 10.1051/0004-6361:20065602.

C. A. O. Torres, G. R. Quast, C. H. F. Melo, and M. F. Sterzik. *Young Nearby Loose Associations*, page 757. December 2008.

P. Tuthill, J. Lloyd, M. Ireland, F. Martinache, J. Monnier, H. Woodruff, T. ten Brummelaar, N. Turner, and C. Townes. Sparse-aperture adaptive optics. volume 6272 of *Proc. SPIE*, page 103, June 2006. doi: 10.1117/12.672342.

P. G. Tuthill, J. D. Monnier, and W. C. Danchi. Aperture masking interferometry on the Keck I Telescope: new results from the diffraction limit. volume 4006 of *Proc. SPIE*, pages 491–498, July 2000.

Peter Tuthill, Sylvestre Lacour, Paola Amico, Michael Ireland, Barnaby Norris, Paul Stewart, Tom Evans, Adam Kraus, Chris Lidman, Emanuela Pompei, et al. Sparse aperture masking (sam) at naos/conica on the vlt. In *Proc. SPIE*, volume 7735, pages 77351O–77351O, 2010.

PG Tuthill, JD Monnier, WC Danchi, EH Wishnow, and CA Haniff. Michelson interferometry with the keck i telescope. *Publications of the Astronomical Society of the Pacific*, 112(770): 555–565, 2000.

A. Vigan, J. Patience, C. Marois, M. Bonavita, R. J. De Rosa, B. Macintosh, I. Song, R. Doyon, B. Zuckerman, D. Lafrenière, and T. Barman. The International Deep Planet Survey. I. The frequency of wide-orbit massive planets around A-stars. A&A, 544:A9, August 2012. doi: 10.1051/0004-6361/201218991.

F. J. Vrba. Role of magnetic fields in the evolution of five dark cloud complexes. AJ, 82:198–208, March 1977. doi: 10.1086/112031.

J. Wang, D. A. Fischer, J.-W. Xie, and D. R. Ciardi. Influence of Stellar Multiplicity on Planet Formation. II. Planets are Less Common in Multiple-star Systems with Separations Smaller than 1500 AU. ApJ, 791:111, August 2014. doi: 10.1088/0004-637X/791/2/111.

S. J. Weidenschilling. Aerodynamics of solid bodies in the solar nebula. MNRAS, 180:57–70, July 1977.

D. C. B. Whittet. The ratio of total to selective absorption in the Rho Ophiuchi cloud. MNRAS, 168:371–378, August 1974.

B. A. Wilking, M. R. Meyer, J. G. Robinson, and T. P. Greene. Optical Spectroscopy of the Surface Population of the ρ Ophiuchi Molecular Cloud: The First Wave of Star Formation. AJ, 130: 1733–1751, October 2005. doi: 10.1086/432758.

Allan Wirth. Dispersed hartmann sensor and method for mirror segment alignment and phasing, November 18 2003. US Patent 6,649,895.

E. L. Wright, P. R. M. Eisenhardt, A. K. Mainzer, M. E. Ressler, R. M. Cutri, T. Jarrett, J. D. Kirkpatrick, D. Padgett, R. S. McMillan, M. Skrutskie, S. A. Stanford, M. Cohen, R. G. Walker, J. C. Mather, D. Leisawitz, T. N. Gautier, III, I. McLean, D. Benford, C. J. Lonsdale, A. Blain, B. Mendez, W. R. Irace, V. Duval, F. Liu, D. Royer, I. Heinrichsen, J. Howard, M. Shannon, M. Kendall, A. L. Walsh, M. Larsen, J. G. Cardon, S. Schick, M. Schwalm, M. Abid, B. Fabinsky, L. Naes, and C.-W. Tsai. The Wide-field Infrared Survey Explorer (WISE):

Mission Description and Initial On-orbit Performance. AJ, 140:1868, December 2010. doi: 10.1088/0004-6256/140/6/1868.

A. N. Youdin and F. H. Shu. Planetesimal Formation by Gravitational Instability. ApJ, 580: 494–505, November 2002. doi: 10.1086/343109.

N. Zacharias, D. G. Monet, S. E. Levine, S. E. Urban, R. Gaume, and G. L. Wycoff. The Naval Observatory Merged Astrometric Dataset (NOMAD). In *American Astronomical Society Meeting Abstracts*, volume 36 of BAAS, page 1418, December 2004.

B. Zhang, M. J. Reid, K. M. Menten, and X. W. Zheng. Distance and Kinematics of the Red Hypergiant VY CMa: Very Long Baseline Array and Very Large Array Astrometry. ApJ, 744: 23, January 2012. doi: 10.1088/0004-637X/744/1/23.